NUCLEAR REACTIONS IN THE CRUST OF ACCRETING NEUTRON STARS

By

Kit Yu Lau

A DISSERTATION

Submitted to
Michigan State University
in partial fulfillment of the requirements
for the degree of

DOCTOR OF PHILOSOPHY

Physics

2012

ABSTRACT

NUCLEAR REACTIONS IN THE CRUST OF ACCRETING NEUTRON
STARS

By

Kit Yu Lau

There have been many discoveries from observations of accreting neutron stars in X-ray binaries. Many of the observed phenomena such as superbursts or the cooling of quasi-persistent transients during their quiescent state are affected by the thermal properties and the composition of the crust. To model the nuclear energy release and crust composition, we build up a first complete network with pycnonuclear fusion. We run a consistent nuclear reaction network that follows the evolution of an accreted fluid element from the atmosphere down to the inner crust. We take into account a majority of the most important nuclear processes including electron capture, neutron capture, neutron emissions, β^- decay, and pycnonuclear fusion reactions. The result of the model shows that there is nuclear reaction path splitting in the crust of accreting neutron stars due to the usage of finite electron capture rates. The pycnonuclear fusion reactions can occur at a shallower depth than previously thought. The composition deep inside the inner crust is mainly ^{40}Mg, independent of the initial composition of the ashes of the outer crust. The inner crust is found to be very pure no matter what the initial abundance of the ashes is in the outer crust. The neutron drip which is the density that neutrons start dropping out from the nuclei, locates at a higher density in our model. In general, the nuclear reaction path and the heat energy generation in the inner crust are significantly different from the previous work.

ACKNOWLEDGMENTS

TABLE OF CONTENTS

LIST OF FIGURES

Chapter 1

Introduction

Neutron stars consist of the densest matter in the Universe [1, 2]. They are the remnants of the gravitational collapse of massive stars during supernovae events. Neutron stars are mostly composed of neutrons. There are ions and electrons in the outer crust and electrons, neutrons and nuclei in the inner curst. The core consists of superdense matter composed of neutrons, protons, muons, and possibly hyperons, quarks, pions, and kaons [3]. Neutron stars are supported by quantum degeneracy pressure due to the Pauli exclusion Principle, which does not allow two neutrons to occupy the same quantum state simultaneously. X-ray observations can help us understand these objects. Neutron stars are either observed in isolation [4] or in binary systems where the neutron star orbits a companion star - a regular star, a white dwarf, a black hole, or another neutron star. Some highly magnetized neutron stars emit strong radio radiation and are radio pulsars. Radio pulsars in binary systems can be used to determine accurately the mass of the neutron star through relativistic orbital effects that affect the observed radio pulsations [5]. Neutron star masses between 1.35 [6] to 1.97 solar masses[7] have been observed. If the companion star is a white dwarf or a main

sequence star then mass transfer onto the neutron star can occur, leading to X-ray emissions that can be highly variable. Examples for extreme variations in X-ray flux are recurrent X-ray bursts, soft X-ray transients and Superbursts [8]. X-ray bursts are periodic and rapid increases in luminosity peaked in the X-ray regime of the electromagnetic spectrum. Soft X-ray transients emit X-rays for some time before they turn off for extended periods of time, possibly due to instabilities in the accretion process. Superbursts are particularly long energetic X-ray bursts. These surface phenomena probe the neutron star surface and can also provide information on compactness [9]. Many of these observations are influenced by nuclear processes. Nuclear reactions heat up the surface as well as the crust. When the accretion stops and the crust starts cooling down, it continues to emit X-rays due to the residual nuclear heat. The goal of our work is to understand the nuclear reactions that heat the neutron star crust during accretion. These nuclear reactions also set the composition as a function of depth. The crust composition in turn determines crust properties such as thermal and electrical conductivities [10], elastic properties [10], viscosity [10], superfluidity and superconductivity [10], neutrino emissions [10], g-mode oscillations [11] and evolution of magnetic fields [12]. The reactions in the crust might also deform the crust leading to the possibility of gravitational wave emission if the neutron star is spinning rapidly [13].

Detailed studies of the composition of accreting neutron star crusts were carried out first by [14] and by [15]. The energy released by nuclear reactions in the accreting neutron star crust was first calculated by Vartanyan and Ovakimova [16]. Haensel & Zdunik [17] further developed the work by using different S factors for the pycnonuclear fusion rates and different mass models. They calculated the compositional changes with depth by minimizing the Gibbs Free energy of a Wigner-Seitz cell of accreted matter assuming only electron

captures, neutron emissions and absorption and pycnonculear fusion occur. They assume the nuclear reactions happen at zero temperature, a single nuclide composition and infinitely fast reaction rates [18]. Gupta et al [19, 20] went the next step by using a reaction network which included realistic electron capture rates and neutron emissions. In our work, we use a complete reaction network calculation with a self-consistent thermal structure and finite electron and neutron capture rates. A new formalism for pycnonuclear reaction rates in a multicomponent plasma is also used [21]. The results differ significantly from previous work due to the more comprehensive and detailed modeling of the nuclear processes. Examples for such differences include the splitting of the nuclear reaction path due to the usage of finite electron capture rates. The pycnonuclear fusion reactions occur at a shallower depth. The composition in the inner crust is substantially different and consists of mainly ^{40}Mg, independent of the initial composition of the ashes of the outer crust. The inner crust is found to be very pure no matter what the initial abundance of the ashes is in the outer crust. In general, the nuclear reaction path and the heat energy generation in the inner crust are significantly different from the previous work.

The thesis will be organized as follows: In chapter 2 some background information on neutron stars and related phenomena is given. In chapter 3, the detail of our thermal and nuclear model for accreting neutron star crusts is discussed. In chapter 4 follows a detailed discussion of the nuclear reactions and heat generation. In chapter 5 a brief discussion of the potential impact on various crust properties and observables follows.

Chapter 2

Background

Since the purpose of the thesis is to investigate the nuclear reactions in the crust of accreting neutron stars, an introduction to formation and principal properties of neutron stars is given in the following subsections. The idea of neutron stars was first proposed by Baade and Zwicky in 1934 [22]. They suggested that a neutron star can be formed in a supernova explosion. The first calculation of the neutron star structure was performed by Oppenhemier & Volkoff in 1939 [23]. They assumed neutron star matter is composed of an ideal gas of free neutrons at high density. However, this simple model failed to predict observed neutron star masses. Later, Cameron calculated the structure of neutron stars using a Skyrme force model in the 1950's [24]. Neutron stars in the form of pulsars were first discovered in 1967 [25]. About a year later the discovery of a similar source in the Crab Nebula [26] further supported the idea that neutron stars are the remnants of supernova explosions.

2.1　Birth of a neutron star

When a massive star($\geq 8M_\odot$) reaches the end of its life and undergoes gravitational collapse, the core collapses into a neutron star or a black hole and a supernova explosion occurs. The explosion mechanism is not well understood, but the most promising mechanism is the so called delayed neutrino driven mechanism: the core collapse stops when the star's interior density reaches nuclear saturation density and a shock wave is produced at the boundary between the collapsing inner core and the infalling outer core. The outgoing shock wave loses energy due to neutrino emissions and nuclear dissociation of the infalling material and therefore stalls at radii of about 100 to 200 km. The neutrinos from the core resuscitate the shock, which then accelerates the stellar envelope outwards leading to mass ejection. The proto-neutron star left behind shrinks rapidly because of pressure losses from neutrino emissions. At the resulting high densities the high electron Fermi energy leads to neutralization by fusing electrons and protons into neutrons. As a result the core heats to temperatures around 6.0×10^{11} K. After 10 to 20 s, neutrino emission starts to cool the neutron star [1].Figure 2.1 is a diagram showing the main stages of the evolution of a neutron star. The radius R and central temperatures T for the neutron star are indicated as it evolves in time t [1].

2.2　Structure of a neutron star

Neutron star masses in the range of 1.35 [6] to 1.97 [7] solar masses have been measured, with radii to be less than 20 km. There are five major regions in a neutron star: atmosphere, ocean, crust, outer core and inner core. The atmosphere and ocean are made of normal atoms.
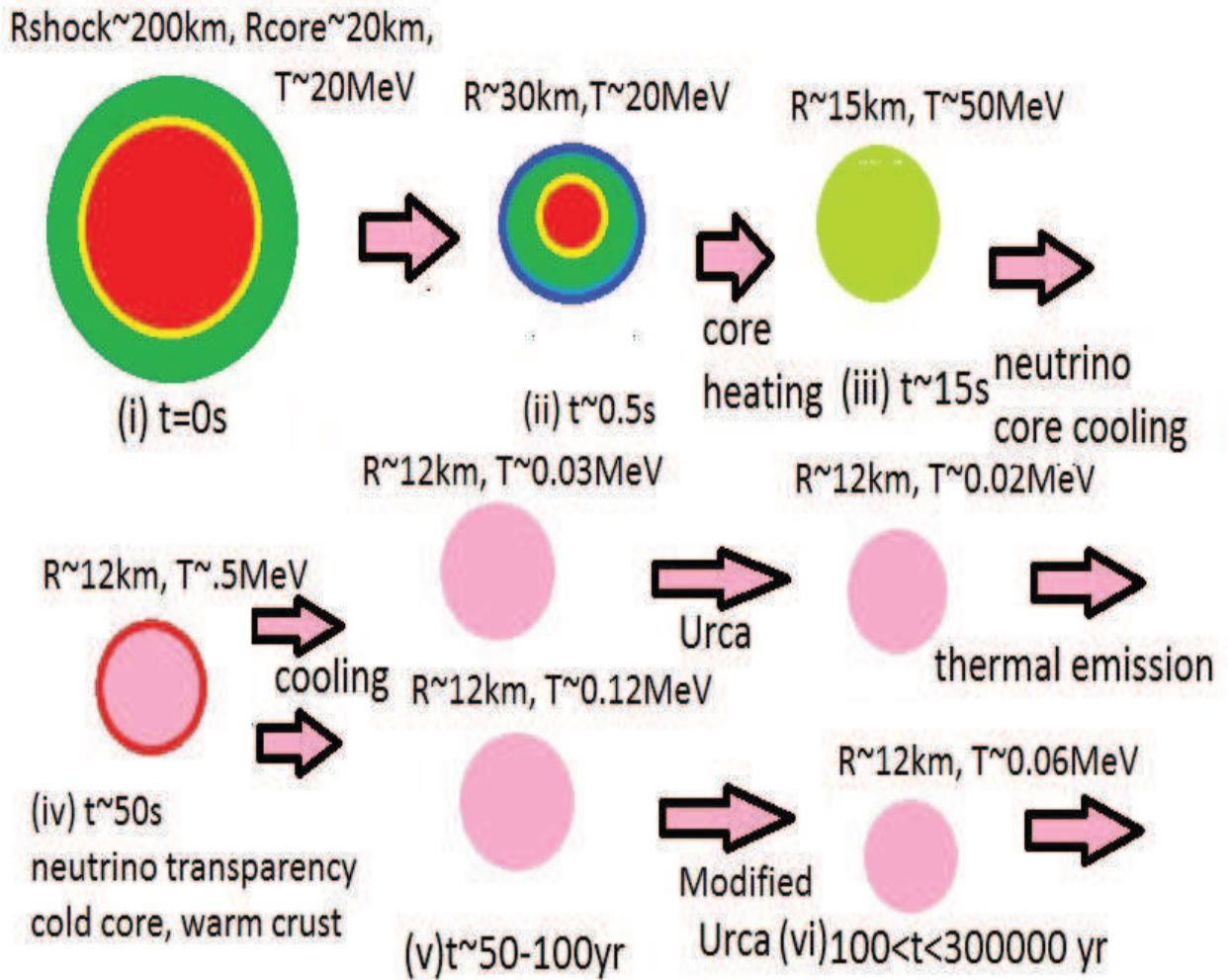
Figure 2.1: The main stages of evolution of a neutron star [1]. For interpretation of the references to color in this and all other figures, the reader is referred to the electronic version of this dissertation.

They are thin shells with negligible mass compared to the total stellar mass. Although the atmosphere is not hot and dense enough for nuclear reactions to happen, it plays an important role in shaping the emergent photon spectrum. Beneath the atmosphere is the ocean, which influences the transport and release of thermal energy from the star's surface. The crust which is about 1 to 2 km thick contains mainly of ionized nuclei and neutrons. The dominant nuclei in the crust vary with density, and it is the main focus of this thesis to investigate the composition of the crust of an accreting neutron star.

The crust is further divided into outer crust and inner crust. The outer crust consists of ordinary nuclei and electrons and starts at a density around 1.0×10^6 g cm^{-3}. It reaches down to neutron drip density, which is the density where neutrons drip out from nuclei, around $4.0 - 6.0 \times 10^{11}$ g cm^{-3}. The inner crust begins at neutron drip and consists mostly of a mix of neutrons, nuclei and electrons, and extends to the bottom of the crust at a density around 10^{14} g cm^{-3}. Just above the core-crust interface, theory [1] predicts a transition from three-dimensional (3D) nuclei, to 2D cylindrical nuclei, to 1D slabs of nuclei interlaid with planar voids, to 2D cylindrical voids, and to 3D voids before a transition to uniform nucleonic matter in the core. This series of transitions is known as nuclear pasta. At the core-crust interface, nuclei are so close together that they are nearly touching each other.

Beneath the crust is the core which constitutes most of the mass of the star. The composition of the core is less well known due to uncertainties in the equation of state for matter exceeding nuclear matter saturation density ($\sim 0.17 fm^3$). The outer core is made of nucleons, electrons, and muons. The inner core region possibly consists of more exotic particles such as hyperons, pions or kaons. A Quark condensate may be found in the center of the neutron star [1].
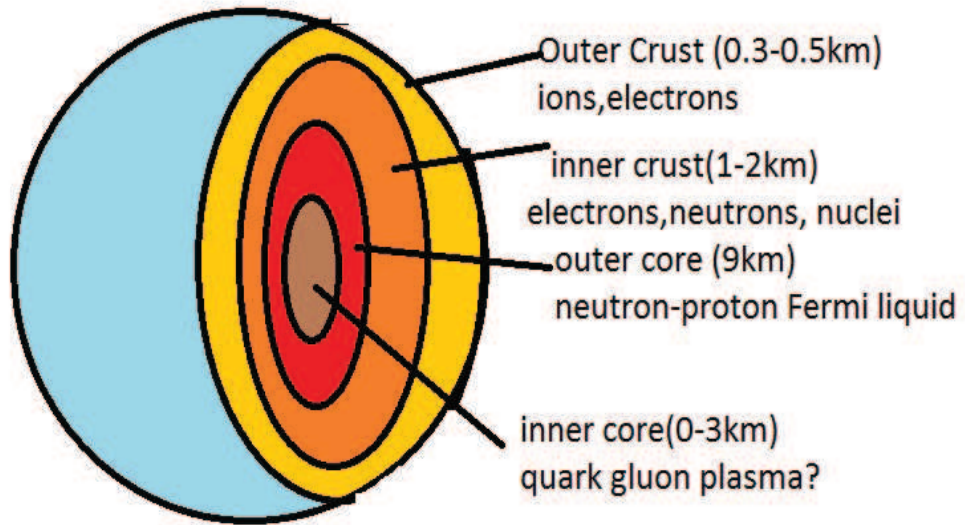
Figure 2.2: Schematic cross section of a neutron star

2.3 Accreting neutron stars

Accreting neutron stars accrete matter from a companion star and are bright X-ray sources, so called X-ray binaries. They can be further divided into low mass X-ray binaries, intermediate X-ray binaries and high mass X-ray binaries depending on the mass of the companion stars. Low mass X-ray binaries have donor stars' masses $\leq 1M_\odot$. High mass X-ray binaries have companion stars with masses larger than about $10M_\odot$ while intermediate X-ray binaries have companion stars with masses in between [27]. In this thesis, our interest is in low mass X-ray binaries (LMXB). These systems are usually found in the galactic bulge and in globular clusters because the companion star tends to be old. Matter is typically transferred from the companion star (primary star) to the compact star (secondary star) by Roche lobe overflow. The Roche lobes is the equipotential suface that includes the inner Lagrange point

(see Fig. 2.3). Interior evolutionary changes of a star cause it to expand and fill up its Roche lobe at which point matter can flow slowly over the gravitational potential saddle point (Lagrange point) between the two stars. Because of angular momentum conservation, the overflowing matter forms an accretion disk around the neutron star. Total accretion rates are typically $10^{15} - 10^{18}$ g s^{-1}. When matter approaches the neutron star surface, it is decelerated heating up the gas and leading to the emission of X-rays [2]. The Eddington accretion rate represents an upper limit on the accretion rate as long as matter is distributed evenly across the neutron star surface. The Eddington mass accretion rate is defined as the rate at which the gravitational energy released by the in-falling matter generates the Eddington luminosity, which is the maximum luminosity a star can emit while remaining in hydrostatic equilibrium. Assuming Thomson scattering is the only opacity source, the Eddington limit $\dot{m}_{Edd}$ can be calculated as [28].

$$\dot{m}_{\mathrm{Edd}} = \frac{2m_p c}{(1 + X_{\mathrm{H}})R\sigma_{\mathrm{T}}} = 8.8 \times 10^4 (1.71/(1 + X_{\mathrm{H}}))(\frac{10\mathrm{km}}{R})\mathrm{gcm}^{-2}\mathrm{s}^{-1} \qquad (2.1)$$

where X_{H} is the hydrogen mass fraction of the accreted material, m_{p} is the proton mass, σ_{T} is the Thomson cross section, R is the radius of the star and c is the speed of light.

2.4 X-ray Bursts

A new class of bursts, known as type I X-ray bursts, was discovered in 1975 [29]. Type I X-ray bursts are thought to be powered by thermonuclear explosions on the surface of weakly magnetized neutron stars [30]. These X-ray bursts last for seconds to minutes and have a recurrence time of the order of hours or days. Their luminosity ranges from 10^{36} to 10^{38}
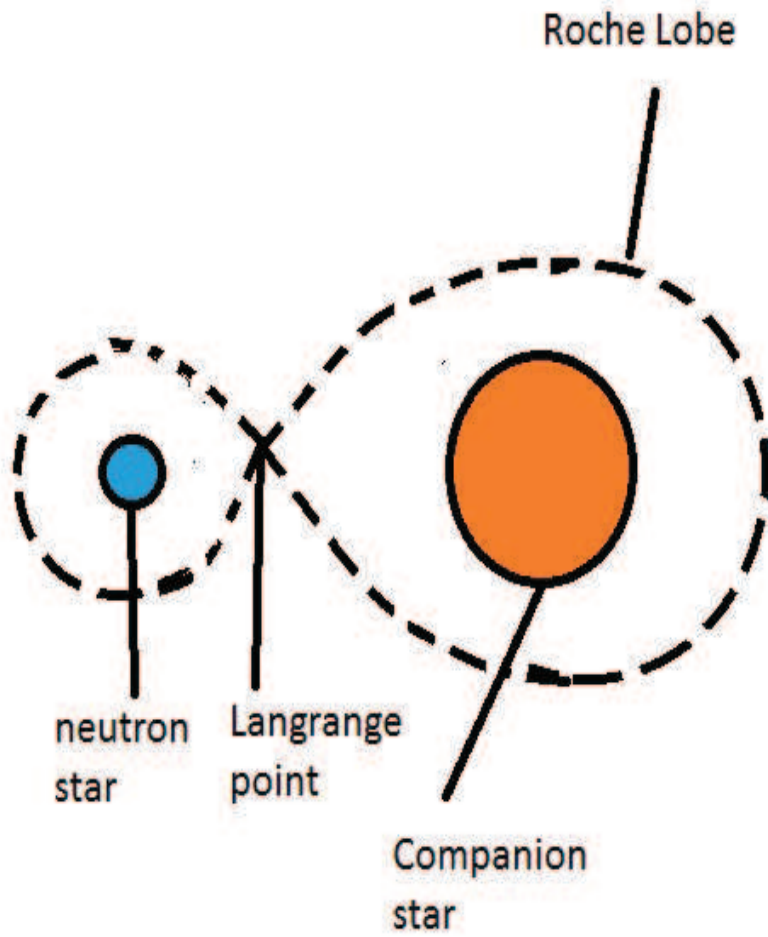
Figure 2.3: Roche Lobe of a binary system

erg s^{-1}. Typical rise times of X-ray bursts are 2 s but can be up to 10 s, while the roughly exponential decay time ranges from 10 s to several minutes. X-ray bursts are produced when ionized hydrogen and helium are accreted from the envelope of the companion star, accumulated on the neutron star, and ignited. During accretion the gravitational energy release is about 200 MeV/u and powers the continuous X-ray emission of the X-ray binary. Some of the X-ray bursts are powered by the rp-process (rapid proton capture process) which releases less than 6 MeV/u, which is small compared to the gravitational energy. However, X-ray bursts are observable as the nuclear energy is released in very short period of time [31]. Many bursts are powered by mixed hydrogen and helium burning. In this case the burst is triggered by helium burning via the 3-α reaction. Cooling through expansion is prevented because the matter is degenerate. When matter is degenerate, pressure is independent of temperature, and therefore a temperature rise does not induce an expansion. The result is a thermonuclear runaway as the rise in temperatures accelerates the thermonuclear reaction rates. The acceleration in reaction rates further increases the temperature, which increases the thermonuclear reactions and so on. Thus the temperature becomes quickly high enough to allow ^{15}O and ^{18}Ne to undergo a (α, p) reactions leading to breakout from the hot CNO cycle marking the onset of the (α, p) process. After the (α, p) process (a sequence of (α, p) and (p, γ) reactions) burning of hydrogen via the rapid proton capture process (rp-process) follows. At the drip line, the (γ, p) process slows (p, γ) down. In those cases, β^+ decays can compete with proton capture. Peak temperatures as high as 1-2 GK have been predicted to be reached in X-ray bursts [32]. The furthest point that the rp-process can reach are the isotopes where a SnSbTe cycle is formed by (γ, α) reactions on α unbound proton-rich Te isotopes [32]. Figure 2.4 shows the predicted composition of the X-ray burst ashes. As the
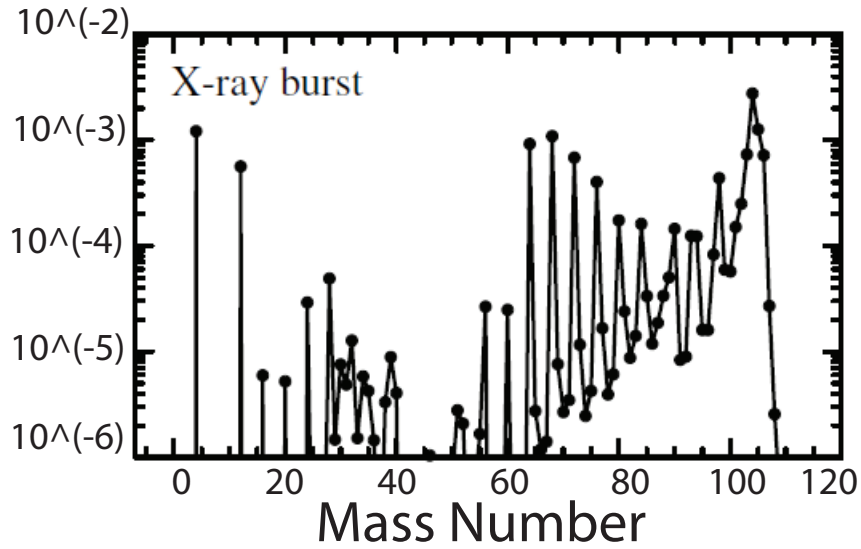
Figure 2.4: Abundances as a function of mass number of X-ray burst ashes. Abundances are defined as the mass fraction over the mass number [32]

burst cools, the burning layer shrinks and forms a layer on the neutron star surface. The fuel for the next burst is then accreted on top of this layer of ashes.

2.5 Superbursts

Superbursts are rare, extremely powerful X-ray bursts (see Fig. 2.5). They are 1000 times more energetic than X-ray bursts, last for hours and have recurrence times of years. Super-bursts are expected to occur at a density around 10^9 g cm^{-3}, which is 3 orders of magnitude occurs deeper in density than regular X-ray bursts. The much higher ignition depth explains the longer recurrence time and the higher total energy as more matter needs to be accumu-lated to trigger the burst. They have a rapid rise time and a long decay time of typically a few hours, with similar spectra as X-ray bursts, indicating their thermonuclear origin. Superbursts are typically observed in a system with mass accretion rates of $0.1 - 0.3\dot{M}_{\mathrm{Edd}}$

but have also been found in more rapidly accreting sources [33]. Superbursts are believed to be produced by the ignition of carbon in the ashes ocean on the neutron star surface. However, the origin of significant amounts of carbon is still an open question. Superbursts are an important probe for the properties of neutron stars since they are more sensitive to the thermal properties of the crust and core cooling models as they occur in a deeper region compared to ordinary X-ray bursts. Superbursts can help to constrain the thermal conductivity of the neutron star crust and the rate of neutrino cooling in the core [34]. Gupta et al [19] found that there is roughly 4 times more heat deposited in the outer crust than predicted before due to the electron captures to excited states. The higher heat release in the outer crust leads to a higher temperature reducing the ignition depth of carbon burning and shortening the recurrence time of superbursts. This helps to reduce the discrepancy between the observation and theory, though it cannot completely account for the discrepancy.

2.6 Soft X-ray transients

Transient X-ray sources are quiescent for most of the time but are bright X-ray sources during their active state, which lasts typically for 10-100 days [36]. They were initially classified based on their spectral hardness because their nature was unclear [37]. Hard X-ray transients are characterized by an equivalent temperature of > 15keV. Equivalent temperature is the temperature of an air parcel from which all the water vapor has been extracted by adiabatic process. They are believed to contain a young, pulsating neutron star orbiting a Be star companion [38]. Soft X-ray transients (SXRTs) are characterized by an equivalent temperatures of < 15keV and usually show type I X-ray bursts during their active state. They are believed to belong to the class of low mass X-ray binaries (LMXRBs)
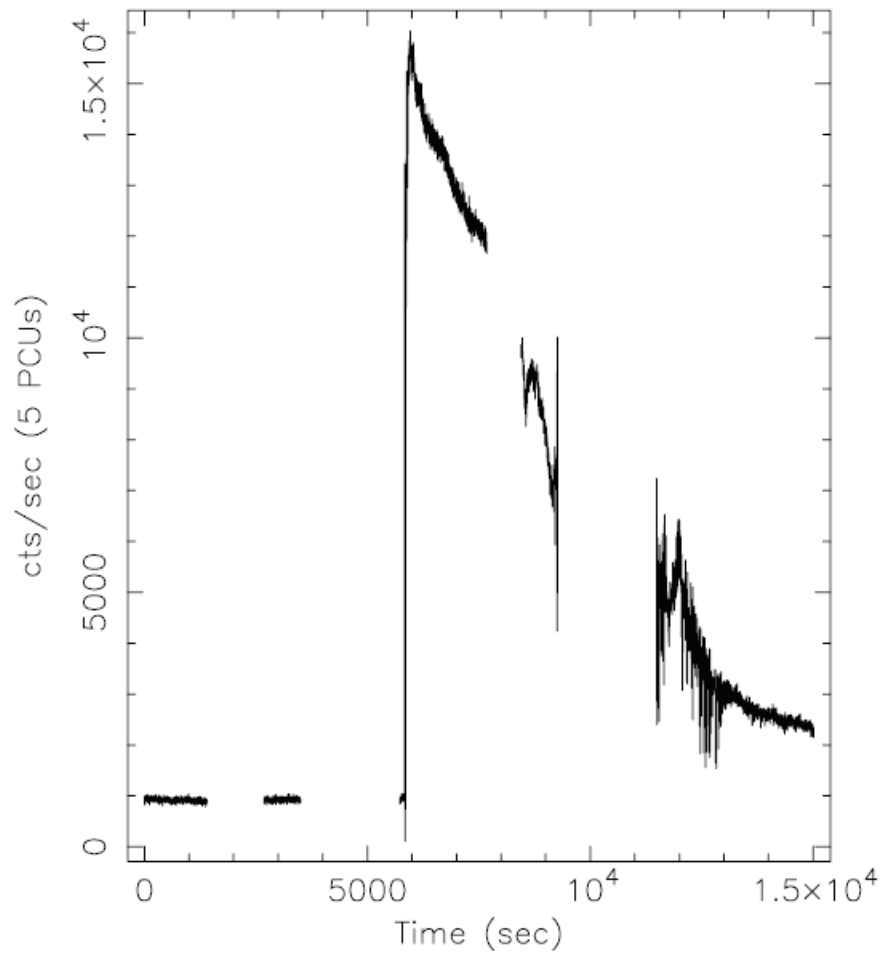
Figure 2.5: Light curve of Superburst from 4U1820-30 [35]

14

containing an old neutron star. There are also ultrasoft X-ray transients, which do not contain any bursts or pulsations, and are believed to contain a black hole [39].

Soft X-ray transients are binary systems where the accretion onto the neutron star turns on and off for periods ranging from months to decades, possibly due to the thermal accretion disc instabilites [36]. During the accretion outburst, the neutron star emits X-rays similar to persistent X-ray binaries. At the beginning of an outburst the flux increases over a few days and reaches X-ray luminosities of $\sim 10^{37} - 10^{38}$ erg s^{-1}. It then decays by a slow, nearly exponential decay with a timescale of weeks to months. When the accretion turns off, there is a residual quiescent luminosity. For example, Aq1 X-1 emits $\sim 10^{32} - 10^{33}$ erg s^{-1} in the quiescent state.

The spectral evolution can be described as follows: First there is the beginning of the outburst, which shows relatively soft spectra when they are close to the outburst peak, (kT ~ 5 keV). The outburst phase has intermediate luminosities ($\sim 10^{35} - 10^{37}$ erg s^{-1}) during the rise and decay of the outburst. It declines with a high energy tail extending to at least ~ 100 keV.

Most models of SXRT involve accretion disk instabilities. A compact star is continuously accreting from a disk fed by a companion star filling its Roche lobe and transferring matter. In disk instability models, the accretion disk can become thermally and viscously unstable due to strong opacity variations caused by partial ionization of hydrogen [40]. [41] modified the model by pointing out the importance of X-ray heating of the accretion disk which leads to recurrence times.

The nature of the quiescent luminosity is not known with certainty. Four types of models have been discussed: residual accretion onto the neutron star surface [36], residual accretion

to the magnetosphere radius which defines as the radiation pressure dominated region of an accretion disc surrounding a neutron star [36], non-thermal processes powered by the rotational energy loss of a rapidly spinning neutron star [42] and thermal emission from the hot neutron star [36]. The latter is an important motivation for this thesis. When matter accretes on the neutron star, it may burn steadily or have X-ray bursts in the atmosphere of the neutron star. The ashes from the atmosphere are continuously pushed down to the crust and undergo further nuclear reactions such as electron capture, neutron emission and absorption and pycnonculear fusions [17]. These nuclear reactions release heat energy which further heats the crust of the neutron star. While the core is isothermal, the crust is not and can be at a higher temperature than the core due to the crust heating processes. When accretion halts, we can see the luminosity from the crust.

There are observational evidences for the thermal emission model. The quiescent spectra measured with Chandra ACIS-S of the transient neutron star Aq1 X-1 after the accretion outburst is consistent with that predicted by Brown, Bildsten and Rutledge [43] from deep crustal heating [44]. However, the observation of hard tails and flucutations in Aq1 X-1 and Cen X-4 [45] can hardly be reconciled with quiescent emission being powered by this mechanism alone.

Observations of soft X-ray transients are important for constraining properties of the neutron star, as probing the thermal state of the crust helps to determine the cooling mechanism of the neutron star. In that context quasi-persistent X-ray transients (long period transients) provide the unique opportunity to measure the crust cooling behaviour of an accreting neutron star as a function of time.

KS1731-260 and MXB1659-29 [46] are two such sources, where the quiescent emission is

16

believed to be powered by the thermal emissions from the cooling crust [47]. KS 1731-260 was first observed in August 1989. It was in its active state [48, 49] until early 2001 [50]. It then went into the quiescent phase within two months. It had a luminosity $\sim 1 \times 10^{33}$ erg s^{-1} at that time. In 2001 September the source was found to have a luminosity of approximately (2-5) $\times 10^{32}$ erg s^{-1} [51]. According to neutron star cooling models, this decrease in luminosity can be interpreted as the rapid cooling of the neutron star crust. MXB 1659-29 was first detected [52] in October 1979. In July 1979, it was in its quiescence state [53]. It continued to exist in the state for 21 years until in April 1999 (Zand et al. 1999) [54] it switched to the active state. After 2.5 years in the active state, MXB 1659-29 went back to quiescence in September 2001 [55] with a residual luminosity of (3.2-4.3) $\times 10^{33}$ erg s^{-1} assuming a distance of 10kpc [56]. When MXB 1659-29 was in quiescence, it was observed that the luminosity was decaying exponentially, decreasing by a factor of 7-9 over 1.5 years [57].

The cooling light curves of these quiescent transients can be used to probe the thermal structure of the neutron star crust. An example for this is given by Brown et al who fitted the light curve with a broken power law (see Fig. 2.6) [58]. The break in the power law is explained by a change in heat capacity at the corresponding depth in the neutron star crust. Such a change in heat capacity is predicted by the model because of the onset of a significant fraction of free neutrons. The quantitative interpretation of the cooling light curves depends on the understanding of the thermal structure of the neutron star crust, in particular the distribution and strength of various nuclear heat sources. This is the topic of the thesis.

kT$_{\mathrm{eff}}$(eV)
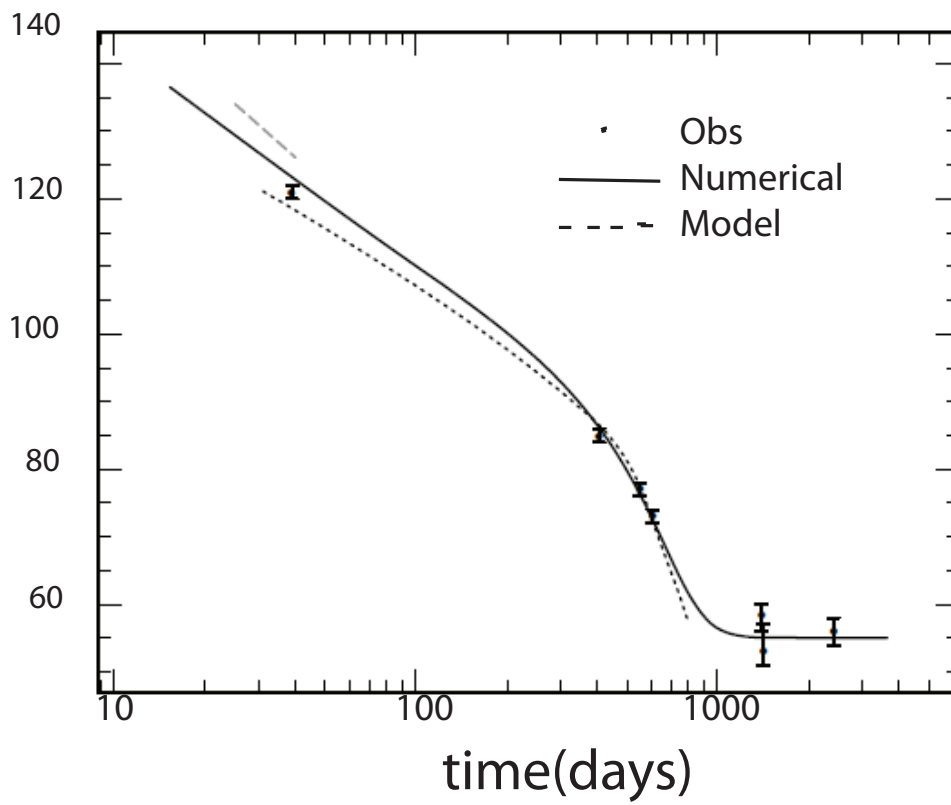
Figure 2.6: Comparison of the light curve of the X-ray transient MXB1659-29 during quiescence with model calculations [58]

18

Chapter 3

Model

In order to understand the nuclear reactions and heat generation in the accreting neutron star crust, we developed a dynamic model that includes electron capture rates, neutron capture rates, and pycnonuclear fusion rates coupled to a thermal neutron star crust model. We use a large nuclear reaction network of ~ 3000 isotopes covering the mass range A=1-181 and extending from stable nuclei to beyond the neutron-drip line in order to follow the nuclear reaction sequences in detail. This approach has been used before by [19] up to neutron drip. [20] then extendend their model to just beyond neutron drip line. We extend the [19] model to include neutron emission and absorption processes, and for the first time, pycnonuclear fusion rates. Our model follows the dominant nuclear processes in detail. It is very different from most earlier approaches (except Gupta et al [19, 20]) where the Gibbs free energy of a Wigner-Seitz cell at constant pressure is minimized, assuming zero temperature and where the composition was limited to a single species at a given depth as in ref [17]. I will discuss the equation of state, thermal structure, mass model and nuclear reactions used in the model.

3.1   Equation of State

The neutron star structure is taken from Brown et al [59, 34]. We assume a neutron star radius of $R = 10.8$ km and a mass M of $1.6 M_{\odot}$. The resulting surface gravity $GM/R^2(1+z)$ is 2.43×10^{14} cm s^{-2} where G is the gravitational constant. The gravitational red shift z is $[1 - 2(GM)Rc^2]^{-1/2} - 1 = 0.33]$. The crust mass is $0.01 M_{\odot}$ and the crust thickness is about 0.3 km. A mass accretion rate in the rest frame on the surface of $\dot{M} = 3.0 \times 10^{17}$g s^{-1} is chosen based on typically observed rates. Assuming spherical, isotropic accretion this corresponds to a local accretion rate per unit area of 2.1×10^4 g s^{-1} cm^{-2}. For solar composition the resulting luminosity generated by the gravitational energy release is 30% of the Eddinton luminosity. The sensitivity of the calculations on neutron stars parameters and accretion rates should be explored in future work.

Electrons, ions and neutrons contribute to the equation of state of the crust. Electrons are relativistic and degenerate and the table of the Helmholtz free energy (a thermodynamic potential that measures the "useful" work obtainable from a closed thermodynamic system at a constant temperature and volume) from [60] Timmes & Swesty is used. The pressure from ions is calculated from the derivatives of the Helmholtz free energy with respect to the ionic free energy. The equation of state for the ions lattice comes from fits by [61] Farouki& Hamaguchi (1993), who modeled the molecular dynamics of a one component, strongly-coupled plasma. The neutron pressure is calculated from the zero temperature compressible liquid drop model of Ref [62].

3.2 Thermal Structure

The thermal structure of the neutron star is calculated as in Brown (2000) [59]. The model assumes hydrostatic equilibrium. The pressure is approximated to be nearly independent of temperature. The gravitational potential $\Phi \approx 1/2c^2 \ln(1 - 2GM/rc^2)$ is nearly constant in the crust. Under these approximations, the equations for temperature, luminosity, and nuclear heating are solved as follows [59],

$$\frac{dT}{dr} = \frac{-L(1+z)}{4\pi r^2 K} \tag{3.1}$$

$$\frac{dL}{dr} = \frac{dL_{nuc}}{dr} - 4\pi r^2 (1+z)\epsilon_\nu \tag{3.2}$$

$$\frac{dL_{\text{nuc}}}{dr} = \dot{M}Q(r)m_{\text{amu}}^{-1} \tag{3.3}$$

where $z = (1 - 2GM/rc^2)^{-1/2} - 1$ is the gravitational redshift, Q(r) is the heat deposited per accreted nucleon, and $m_{\text{amu}} = 1.66 \times 10^{-24}$ g = 1 amu, K is the thermal conductivity, ϵ_ν is the neutrino energy loss rate. Since the potential of the crust Φ is nearly constant, equations (1) and (2) are simplified by holding e^{Φ/c^2} constant. The physics of interest is contained in the neutrino cooling ϵ_ν, the conductivity K and the nuclear heating L_{nuc}. We will discuss the first two in this section. Nuclear heating is one of the main themes of this thesis and will be discussed in detail in section 4. The equations are solved by a relaxation method [63].

We use the thermal profile obtained by Gupta et al [19] using an iterative process, where an initial profile is used to calculate the heat sources in the crust, which is then used to recalculate the profile. The nuclear processes are not very sensitive to the thermal profile.

This approach is therefore sufficient for the goal of this thesis, which is to identify the critical nuclear reaction sequences. Further iteration processes to obtain a self consistent thermal profile should be done in future work.

3.2.1 Neutrino cooling

We include two neutrino cooling processes in addition to the energy lost by neutrinos emitted in nuclear electron capture and beta decay processes discussed in section 4. Neutrino pair bremsstrahlung is generated when electrons scatter off the Coulomb field of nuclei in the crust [18] (Haensel et al. 1996):

$$e^- + (A, Z) \rightarrow e^- + (A, Z) + \nu\bar{\nu} \tag{3.4}$$

The rate calculation of Haensel et al is used. We also consider Cooper pairing of neutrons in the $^1S_0$ state using an analytical equation from [64].

$$n + n \longrightarrow n + n + \nu + \bar{\nu} \tag{3.5}$$

We neglect neutrino emission in the outer crust such as Plasmon neutrino emissivity since these processes are not significant for the temperatures of interest here.

3.2.2 Heat Transport

Heat is transported by relativistic and degenerate electrons. The conductivity is given by the Wiedemann-Franz law:

$$K = (\pi^2/3)k_{\mathrm{B}}^2 T n_{\mathrm{e}}/m_{\mathrm{e}}^* \tau \tag{3.6}$$

where $m_e^* = E_F/c^2$ (E_F is the electron Fermi energy) is the effective electron mass and τ is the relaxation time, k_B is the Boltzmann constant and n_e is the electron number density.

$$1/\tau = 1/\tau_{ee} + 1/\tau_{eQ} + 1/\tau_{ep} \qquad (3.7)$$

where $\tau_{ee}, \tau_{eQ}, \tau_{ep}$ represents relaxation times for electron-electron, electron-impurity, and electron-phonon scattering. Impurity scattering occurs when there is more than one species of nuclei. Nuclei other than the dominat species can then be considered as an impurity in the lattice structure of the crust, hampering the heat transport. Electron-impurity scattering [65] often dominates the heat transport and is calculated according to Itoh & Kohyama 1993

$$K = 2.363 \times 10^{17} T_8 \rho_6 \sum_i \frac{X_i}{A_i} \times \frac{1}{(1 + 1.018[\sum_i (Z_i/A_i) X_i]^{2/3} \rho_6^{2/3})} < S > \times \frac{< Z >}{Q} \quad (3.8)$$

where T_8 is temperature $T/10^8$, ρ_6 is density $\rho/10^6$, X is the mass fraction, A is the mass number, $< Z >$ is the average proton number, $< S >$ is the structure factor which determines how a material scatters electrons, Q is the impurity parameter.

Electron-electron scattering can be neglected as the strongly degenerate electrons restrict the available phase space. For the electron-phonon relaxation time we use Potekhin et al.[66].

3.3 Nuclear Reactions

The main focus of the thesis is to study the composition and heat generation by nuclear reactions as a function of depth in the neutron star crust. Rates for electron captures with emissions up to 20 neutrons, beta decay, neutron capture, photodisintegration, and pycnonu-

clear fusions are used in our model. Because of the extreme environment with high density ($\rho \sim 10^9$ g cm^{-3} to 10^{13} g cm^{-3}) and temperature (~ 0.5GK) it is impossible to obtain the rates of these processes in the laboratory. Instead, rates are calculated theoretically.

3.3.1 Electron capture rates

Electron capture rates (EC) are calculated theoretically as in Gupta et al [19]. The electron capture rate R_{ij} between a parent nucleus in state i and a daughter nucleus in state j is given by:

$$R_{ij} = ln(2)f_{ij}(T, \rho, E_f)/(ft_{1/2})_{ij} \tag{3.9}$$

where $f_{ij}(T, \rho, E_f)$ is the phase space factor and $(ft_{1/2})_{ij}$ is the comparative half-life. f_{ij} is defined:

$$f_{ij} = \int_{wl} w^2(q+w)^2 G(Z, w) S_-(w, \mu_e)(1 - S_\tau)dw \tag{3.10}$$

where the electron total energy, w, is in electron rest mass units ($m_e c^2$) and q is the nuclear mass difference between parent and daughter ground states in ($m_e c^2$) units corrected by the excitation energies of the initial and final states to yield the channel Q-value: $q = q_{gs} + (E_i - E_f)/m_e c^2$. The capture threshold, wl, is unity if $q \geq -1$ and $|q|$ otherwise. $S_-(w, \mu_e)$ is the Fermi-Dirac distribution for relativistic degenerate electrons. It is very sharply peaked for low temperatures. Tabulation of the phase space integral is therefore difficult. Numerical integration, while challenging, is possible but computationally too expensive as it has to be carried for each step of the model because of the changes in electron density. A fast analytic phase space approximation [67] for f_{ij} that is valid for low temperature is used to solve the problem. The integral is separated into two separate terms at

24

the chemical potential, thus eliminating the need to find the peak of the integrand. The Coulomb correction G(Z,w), is assumed to be constant for the energy range considered here, and is taken outside the integral. Using this approximation, the electron capture phase space can be calculated for each timestep in a reaction network simulation.

The comparative half life $(ft_{1/2})_{ij}$ is related to the nuclear transition matrix elements for transition probability B_{ij} by

$$(ft_{1/2})_{ij} = D/B_{ij}, D = 2\pi\hbar^7/g^2 m_e^5 c^4 \tag{3.11}$$

where m_e is the mass of the electron, c is the speed of light, and g is the β decay strength constant. Calculated electron capture strenghth functions were taken from the results of [68]. These strength functions were calculated using a QRPA model. In the code, a table of electron capture transition strength functions as a function of excitation energy in the daughter nucleus is used. Temperatures are low and the parent nuclei are assumed to be in their ground states. The neutrino losses for each transition are calculated. This is different from earlier work where fixed fraction of $(\mu_e - E_{thr})$ lost to neutrinos was assumed [17].

Electron capture rates and up to 20 induced neutron emissions are included in the network. When the excitation of a daughter nucleus is greater than the neutron separation energy, electron capture induced neutron emission is allowed. Here it is assumed that the largest number of neutrons allowed to be emitted is emitted with a 100 % branching.

The above formalism is not developed for nuclei with $Z < 8$ and for some nuclei that are beyond the neutron drip line. These nuclei are however encountered in some cases in our network. For those nuclei, we assume a ground state to ground state transition, with a $\log((ft_{1/2})_{ij})$ value of 6 and maintain the same fast phase space approximation. This log

$(ft_{1/2})_{ij}$ value is a typical value for the dominant transitions in this mass region.

3.3.2 Beta decay rates

For beta decay rates, the same formulism as for electron capture rates is used. However, instead of using the fast analytic phase space approximation, we use a table of rates as a function of temperature and density. In addition, we set the rate to zero if the Fermi energy is higher than the beta decay threshold.

3.3.3 Neutron capture rates

For two nuclear components i and j in an astrophysical plasma with number densities n_i and n_j and a Maxwell-Boltzmann distribution of relative velocities the number of reactions, r, per $(cm^3 s)$ is given by the following equation:

$$r = n_i n_j \langle \sigma \nu \rangle \tag{3.12}$$

This form assumes neutrons and ions have a Maxwell-Boltzmann velocity distribution. This might not be the case in the deeper crust. Below a correction for the calculation of reverse rates under neutron degenerate conditions is discussed, which has been used in this work. However, we neglect the effect of neutron degeneracy on the forward neutron capture rates. This is justified as these rates have very high theoretical uncertainties.

$$\langle \sigma \nu \rangle = (\frac{8}{\pi \mu^{1/2}}) \frac{1}{(kT)^2} \int \sigma(E) E \exp(\frac{-E}{kT}) dE \tag{3.13}$$

where E is the energy and μ is the reduced mass. The neutron capture rates are calculated

assuming a Maxwell-Boltzmann velocity distribution. Target states μ in an astrophysical plasma of temperature T are thermally populated and the astrophysical cross section σ is given by

$$\sigma(E_{ij}) = \frac{\sum_{\mu}(2J_i^{\mu} + 1)exp(-E_i^{\mu}/kT)\sum_{\nu}\sigma^{\mu\nu}(E_{ij})}{\sum_{\mu}(2J_i^{\mu} + 1)exp(-E_i^{\mu}/kT)} \tag{3.14}$$

Photodisintegration reactions are the reverse reactions of neutron capture. They are derived using detailed balance [70]. The commonly used equation is valid only if the neutrons are non-degenerate:

$$\lambda_{\gamma} = (\frac{A_i A_j}{A_m})^{3/2}\frac{(2J_i + 1)(2J_j + 1)}{(2J_m + 1)}\frac{G_i(T)}{G_m(T)} \times (T)^{3/2}Fe^{-Q/kT} < \sigma_i\nu >^* \tag{3.15}$$

where λ_{γ} in s^{-1} is the photodisintegration rate, temperature $T_9 = T/10^9K$, A is the mass number and $N_A < \sigma\nu >^*$ is the neutron capture rate in cm^{3}s^{-1}mol^{-1}. F is a constant.

$$(T)^{3/2}F = T_9^{3/2}9.8685 \times 10^9 \text{molcm}^{-3}. \tag{3.16}$$

$G(T)$ is the temperature-dependent partition function given by

$$(2J_i^0 + 1)G(T) = \sum_{\mu}(2J_i^{\mu} + 1)e^{-E_i^{\mu}/kT} + \int\sum(2J^{\mu} + 1)e^{-\epsilon/kT}\rho(\epsilon, J^{\mu}, \pi^{\mu})d\epsilon \tag{3.17}$$

with ρ being the level density and μ_m the last included experimentally known state and E_i are the energy of excited states.

The reaction rates are represented in our code as seven parameter 'reaclib' fits using the

expression [71]

$$N_A \langle \sigma \nu \rangle^* = exp(a_0 + a_1 T_9^{-1} + a_2 T_9^{-1/3} + a_3 T_9^{1/3} + a_4 T_9 + a_5 T_9^{5/3} + a_6 \ln T_9) \qquad (3.18)$$

This parameterization is flexible enough to accommodate the different temperature dependencies of the various reaction types across the fitted temperature range $0.01 \leq T_9 \leq 10$.

We use radiative direct capture for the neutron capture rates since the nuclei we are interested in our calculation have low neutron separation energy. The level density may be so low that there are no or only very few compound nuclear states availabe for the neutron to be captured to. Thus the Hauser-Feshbach formalism is not a good approach here. Neutron capture occurs predominantly via a direct electromagnetic transition, direct radiactive capture (DRC) [69], to a bound final state. Following Mathews [69], the DRC cross section $\sigma_{n,\gamma}$ can be approximated as:

$$\sigma_{n,\gamma} = \frac{8\pi}{3} \frac{Z^2}{A} \frac{Re^2}{(2\mu^3 E)^{1/2} c^3} \xi \frac{(2J+1)}{(2l+1)(2s+1)(2I+1)} \times (\frac{Y+3}{Y+1})^2 S_j(Q_j + E) \qquad (3.19)$$

where E is the incident neutron energy on a nucleus with mass A, and I is the spin of the target nucleus, J is the spin of the final state, $R = 1.35 A^{1/3}$ is the effective sharp nuclear radius, and μ is the reduced mass in the entrance channel. The factor ξ is the sum of incident channel spins which lead to the same final spin J . S_J is the spectroscopic factor for the final state which we set to 1 to obtain a crude approximation, Q_J is the binding energy of the final state, and the dimensionless parameter Y is

$$Y = \frac{[2\mu(Q_J + E)]^{1/2}}{\hbar} R = 0.295[\mu(Q_J + E)]^{1/2} A^{1/3} \qquad (3.20)$$

28

Typically, for (n, γ) and (γ, n) reactions, the energies $\hbar\omega$ of electromagnetic transitions can be lower than $\hbar\omega_p$ where ω_p is the plasma frequency. It has been suggested that (γ, n) rates may be suppressed because the γ rays will be screened by the electron plasma [19, 20]. For example, the plasma energy is $\hbar\omega \sim 1.3$ MeV at $\rho Y_e \sim 10^{11}$ g/cm^3 and 4.1 MeV at 10^{12} g/cm^3. This is larger than the typical neutron separation energy S_n which is ~ 1.4 MeV. However, recent theoretical work demonstrated that this is not the case. [72]. Even though the emission of real transverse and longitudinal plasmons will be prohibited when $\omega < \omega_p$, the processes with virtual plasmons (especially the longitudinal virtual plasmon) strongly increase the radioactive decay [72]. Thus the de-excitation due to electron capture will not be prohibited even when the plasma frequency is high. Consequently plasma effects cannot suppress neutron capture reactions (n, γ) at $\omega_p > \omega$. At the temperature range that our model concerns, there will be a high level of fluctuating plasma micro fields (associated with virtual plasmon) to power the inverse reaction (γ, n) and the associated rates will be modified. However, the rates are very uncertain due to lack of nuclear structure information on the exotic nuclei in question. Thus we decided to ignore the problem for now and factor it into the (n,γ) rate uncertainties. Further work should be done in the future to improve the model to include the plasma enhancements properly.

However, the velocity distribution of the neutrons or ions are not a Maxwell-Boltzmann distribution anymore when the neutron density is too high or the temperature is too low. The neutron gas becomes degenerate when the thermal energy is less than the Fermi energy

$$\frac{3}{2}k_{\mathrm{B}}T < \frac{\hbar^2}{2m}(3\pi^2 n)^{2/3} \tag{3.21}$$

where m refers to the mass, and n to be the number density of neutrons. Assume a temper-

ature of around 0.5 GK, the neutron number density should be larger then $\sim 10^{34}$ cm^{-3}. This regime is reached quickly at a column depth (pressure over gravity) 8.0×10^{15} g cm^{-2}.

In order to address this problem, we derive the detailed balance equation for degenerate neutrons. For a Boltzmann gas, the relationship between number density n and the chemical potential is [73]

$$n = \frac{(2J+1)e^{\mu/k_{\mathrm{B}}T}(2\pi m k_{\mathrm{B}}T)^{3/2}}{h^3} \tag{3.22}$$

where n is the number density and μ is the chemical potential, J is the angular momentum, k_B is the Boltzmann constant, T is the temperature, m is the mass, h is the Planck constant. Consider a nuclear reaction involving a photon with photon energy E_γ,

$$X^A + n \longrightarrow \gamma + X^{A+1} \tag{3.23}$$

The relationship between number density n and chemical potential in the approximation of an ideal Boltzmann gas is:

$$n_A = (2J_A+1)\frac{(2\pi m_A k_{\mathrm{B}}T)^{3/2}}{h^3}e^{\mu_A/k_{\mathrm{B}}T} \tag{3.24}$$

$$n_{A+1} = (2J_{A+1}+1)\frac{(2\pi m_{A+1} k_{\mathrm{B}}T)^{3/2}}{h^3}e^{\mu_{A+1}/k_{\mathrm{B}}T} \tag{3.25}$$

Furthermore, the chemical potentials is in equilibrium and have the relationship:

$$\mu_A + m_A c^2 + \mu_{\mathrm{n}} + m_{\mathrm{n}}c^2 = \mu_{A+1} + m_{A+1}c^2 \tag{3.26}$$

where for totally degenerate neutrons μ_{n} is equal to the Fermi energy E_{Fn}. The rest masses

are related to the reaction Q-value E_γ as $m_A c^2 + m_{\rm n} c^2 - m_{A+1} c^2 = E_\gamma$. Thus combining

the 3 equations above one obtains

$$\frac{n_A n_{\rm n}}{n_{A+1}} = \frac{2(2J_A + 1)}{(2J_{A+1} + 1)} \left(\frac{A}{A+1}\right)^{3/2} e^{-E_\gamma} e^{-\mu_{\rm n}} n_{\rm n} \tag{3.27}$$

Comparing with the standard Saha equation, which assumes a Maxwell-Boltzmann distri-

bution for the velocities of all particles:

$$\frac{n_A n_{\rm n}}{n_{A+1}} = \frac{2(2J_A + 1)}{(2J_{A+1} + 1)} \left(\frac{A}{A+1}\right)^{3/2} e^{-E_\gamma} \left(\frac{2\pi\hbar^2}{m_n k_{\rm B} T}\right)^{-3/2} \tag{3.28}$$

one obtains a correction factor:

$$f = \frac{n_{\rm n}}{2(m_{\rm n} kT)(2\pi\hbar^2)^{-3/2}} exp(-\mu_{\rm n}/kT) \tag{3.29}$$

where $n_{\rm n}$ is the neutron density, and m_n is the neutron mass. In equilibrium the ratio of

the (n,γ) rate $N_A < \sigma\nu >$ to the (γ,n) rate λ_γ ratio is then for fully degenerate neutrons:

$$\frac{N_A < \sigma\nu >}{\lambda_\gamma} = \frac{n_A n_{\rm n}}{n_{A+1}} f \tag{3.30}$$

Thus, in our model, we correct (γ, n) rates by the factor f given by Eq.3.29. For the neutron

chemical potential, we use the classical chemical potential for low neutron density and the

neutron Fermi energy for high neutron density. For the neutron chemical potential in the

intermediate region between low neutron density and high neutron density, we use a fitting

curve. Figure 3.1 shows the neutron chemical potential versus the neutron density (m^{-3}) in

log scale for a temperature of 0.5 GK. After the fitting, the code is rerun and calculates the

31

new thermal structure.

Here we just take into account neutron degeneracy to calculate the ratio of the neutron capture rates to (γ,n) rates. Further work on the calculation of neutron capture rates under neutron degenerate conditions is still required for more accurate results. However, the neutron capture rates are quite uncertain. The nuclei involved are far from stability and nothing is known about them. In addition, the neutrons can form Cooper pairs resulting in superfluidity. Below a critical temperature, these Cooper pairs condense into the lowest energy single particle state which form a superfluid. The difference between Cooper pairs and bosons is that Cooper pairs only form below the critical temperature. Microscopic calculations in uniform nuclear matter predict a critical temperature of the order of $T \sim 10^9 - 10^{10}$ K which is above the temperature in our model. This might also alter neutron capture rates and could be taken into account in future work.

3.3.4 Pycnonuclear fusion

Pycnonuclear fusion is fusion of two nuclei due to high density. Due to the uncertainty principle, nuclei still have a zero point energy even at zero temperature. Thus, they have oscillations even at zero temperature. At high density, the nuclei are so closely packed that they vibrate and overlap with each other and fuse. Pycnonuclear fusion occurs in the crusts of accreting neutron stars. In this work we employ the pycnonuclear fusion rates for a multicomponent plasma derived by Yakovlev et al [74]. In this approach, one of the difficulties in the calculation of these rates is the need for reliable astrophysical S factors at astrophysical energies .These energies are low compared to the presently accessible range of laboratory fusion experiments. The S factor is therefore calculated theoretically. At low
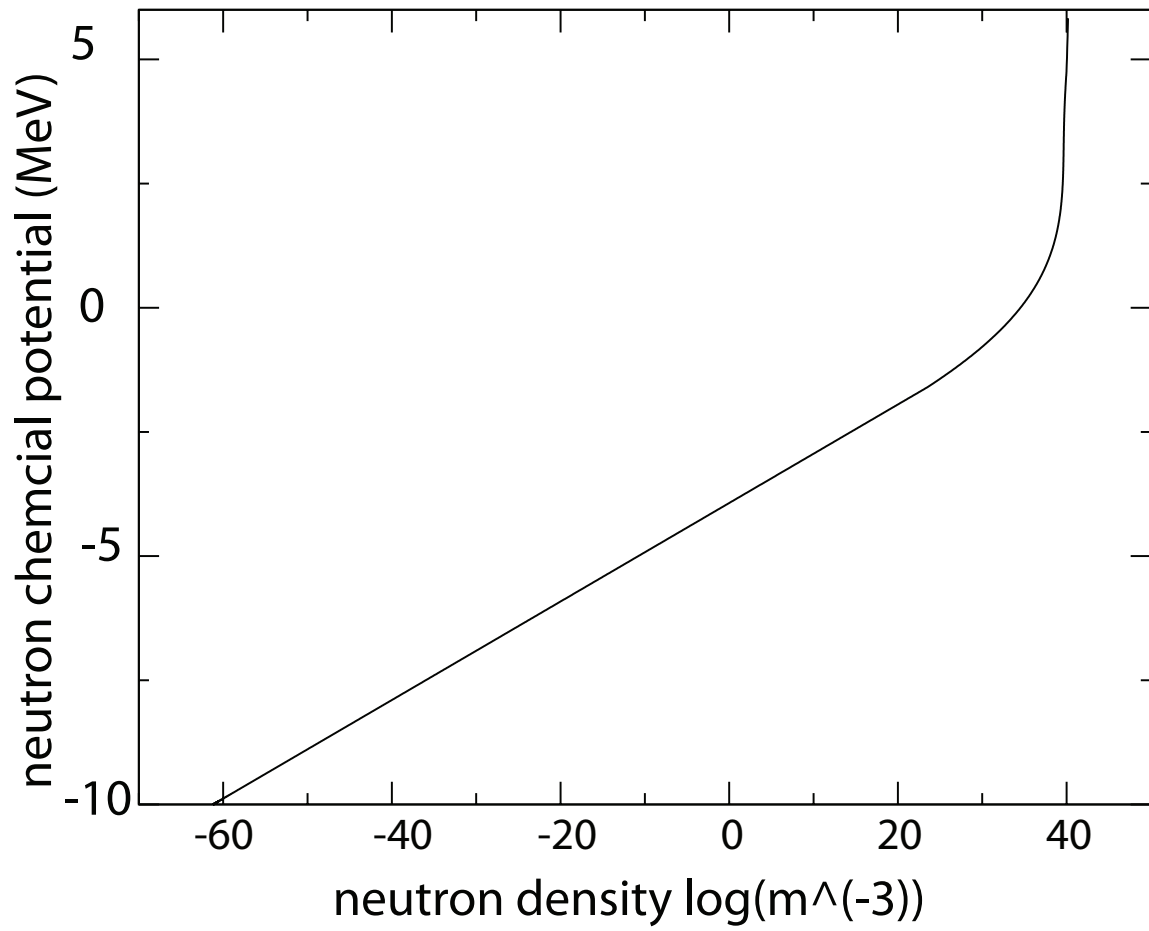
Figure 3.1: The neutron chemical potential versus the neutron density (m^{-3}) in log scale

energies, $\sigma(E)$ is dominated by the l=0 (s-wave) channel. The relationship between the fusion cross section $\sigma(E)$ at low energie, and the astrophysical S factor is then

$$S(E) = \sigma(E)Ee^{(2\pi\eta)} \tag{3.31}$$

where $\eta = (Z_1 Z_2 e^2/\hbar)\sqrt{\mu/(2E)}$ is the Gamow parameter, Z_1 and Z_2 are charge numbers of the nuclei. This parameterization removes from the fusion cross section the strong nonnuclear energy dependence associated with Coulomb barrier penetration.

Another difficulty is related to the plasma physics. One needs to consider the Coulomb fields of the surrounding plasma particles to calculate the Coulomb barrier penetration. These Coulomb fields modify the reaction rates and lead to a screening effect that tends to enhance the reaction rate. One distinguishes five nuclear burning regimes (two thermonuclear regimes, with weak and strong plasma screening respectively; two pycnonuclear regimes for zero-temperature and thermally enhanced burning; and an intermediate regime). Previous model work of the inner crust was limited to a single component plasma where pycnonuclear fusion only occurs among the same nuclides [14, 18]. In the most recent study [18] pycnonuclear fusion rates were estimated using the formulae of [75]. In order to incorporate the reaction rates into the crust model, the phenomenological expression of [21]. is used to describe the pycnonuclear fusion processes in these five regimes. In this approach the fusion cross section is calculated using a one-dimensional barrier penetration formalism and the Sã̃o Paulo potential to describe the real part of the nuclear interaction $V_N(r, E)$:

$$V_N(r, E) = V_{SP}(r, E) = V_F(r)exp(-4v^2/c^2). \tag{3.32}$$

34

$V_F(r)$ is the density-dependent double-folding potential, c is the speed of light, E is the particle collision energy (in the center of mass reference frame), v is the local relative velocity of two nuclei 1 and 2,

$$v^2(r, E) = (2/\mu)[E - V_C(r) - V_N(r, E)] \tag{3.33}$$

$V_C(r)$ is the Coulomb potential, and μ is the reduced mass. The barrier penetration model calculates the reaction cross section $\sigma(E)$ using the standard partial wave (l=0,1,...) decomposition of the effective potential $V_{eff}(r, E)$. Coulomb(V_C), nuclear(V_{SP}) and centrifugal potentials contribute to the potential:

$$V_{eff}(r, E) = V_C(r) + V_{SP}(r, E) + \frac{\hbar^2 l(l+1)}{2\mu r^2}. \tag{3.34}$$

$S(E)$ can be extrapolated to lower energies relevant to stellar burning. Following [21], the energy dependence of $S(E)$ is parameterized by an universal 9-parameter analytic expression:

$$S(E) = exp(B_1 + B_2 E + B_3 E^2 + \frac{C_1 + C_2 E + C_3 E^2 + C_4 E^3}{1 + exp[(E_c - E)/D]}) \tag{3.35}$$

where E is the center-of mass energy of reacting nuclei in MeV, and $E_C, D; B_1, B_2, B_3,$ C_1, C_2, C_3 and C_4 are nine fit parameters. The parameter E_C is approximately equal to the height of the Coulomb barrier. It divides the energy range into that below the barrier $(E \leq E_C)$ and that above the barrier $(E \geq E_C)$, where S(E) behaves distinctly different. The parameter D characterizes a narrow energy width of the transition region between the energy ranges below and above the Coulomb barrier. The parameter B_1 determines

35

$S(0)$. The parameters B_2 and B_3 specify the energy dependence of $S(E)$ at $E \leq E_C$. The parameters C_1, C_2, C_3, C_4, with B_1, B_2 and B_3 contribute to the $S(E)$ dependence at $E \geq E_C$.

A unified phenomenological expression for the temperature and density-dependent reaction rate, which combines all five burning regimes and assumes a uniformly mixed multi-component plasma at low temperatures is expressed as [74]:

$$R_{ij}(\rho, T) = R_{ij}^{pycn}(\rho) + \Delta R_{ij}(\rho, T) \tag{3.36}$$

where $R_{ij}^{pyc}(\rho)$ is the density-dependent pycnonuclear reaction rate at zero temperature and $\Delta R_{ij}(\rho, T)$ is a correction taking into account the thermonuclear burning regime. The S factor enters both of the above two terms. The reaction rates in the thermonuclear regimes (with weak and strong plasma screening) can be calculated reasonably well. The reaction rates in other regimes (zero-temperature and thermally enhanced pycnonuclear regimes; intermediate thermo-pycnonuclear regime) are much less certain. They are very sensitive to currently unknown microphysical correlation properties in a multi-component plasma (a uniform mix, a regular crystalline lattice, a phase-separated matter, a matter with impurities and defects) [74]. The expression above assumes a uniform mix. Other microstructures can strongly change the reaction rates. For example, reactions in a regular multi-component plasma can be strongly suppressed due to the absence of suitable nearby nuclei [74]. For future work it is important to know the actual microstructure of the multi-component plasma at low temperatures. For example, the availability of closest neighbors, local separations, and oscillation frequencies of neighboring nuclei, especially in the presence of impurities and lattice defects.

We neglect all these effects and just use Eq 3.35 and Eq 3.36 in our code. We use the 946 fusion reactions involving stable and neutron-rich isotopes of C, O, Ne and Mg which have been parameterized according to Eq3.35 [21]. For the other pycnonuclear reactions, we extrapolate these fusion rates.

3.4 Mass Models

Nuclear masses are important input parameters for the network calculation. They are used to calculate the phase space for the electron capture and beta decay rates, and for the calculation of (γ,n) rates from (n,γ) rates. They are also used to calculate the (n,γ) rates. They affect energy generation and determine the position of neutron drip. Masses also determine the Q-value of the electron capture and beta decay process which in turn strongly affects the phase space (Eq 3.13) and the depth at which an electron capture reaction occurs [76]. In our nuclear reaction network of ~ 3000 isotopes, we use theoretical mass model when experimental masses [77] are not available. For the mass model and strength functions as well as deformations we use the Finite Range Droplet Mass Model (FRDM) [78], which also provides the input for the calculation of electron capture and beta strength functions providing some self-consistency. For $Z \leq 7$ and very neutron rich nuclei that the FRDM does not cover, we use the analytical Hilf [79] mass formula.

3.4.1 FRDM model

The Finite Range Droplet Mass Model (FRDM) [78] is based on a macroscopic nuclear droplet model with added microscopic corrections for shell and pairing effects. The pairing and shell correction with a folded-Yukawa single-particle microscopic model. The total

nuclear potential energy can be written as

$$E_{\mathrm{pot}}(Z, N, shape) = E_{\mathrm{mac}}(Z, N, shape) + E_{s+p}(Z, N, shape) \qquad (3.37)$$

The values of nine constants are determined from a least squares adjustment to the ground state masses of 1654 nuclei ranging from ^{16}O to ^{263}106 and to 28 fission-barrier heights.

The macroscopic part of the model is mainly a droplet model. The Yukawa-plus-exponential model for the surface tension was incorporated into the droplet model to account for the finite range of the nuclear force and an empirical exponential term was added to account for compressibility effects for light nuclei and for other higher order effects.

The microscopic term is the shell-plus-pairing correction $E_{s+p}(Z, N, shape)$ which is the sum of the proton shell-plus-pairing correction and the neutron shell-plus-pairing correction. The shell correction is calculated by use of Strutinsky's method. For the pairing correction the Lipkin-Nogami version of the BCS method is used.

The rms error of the mass model is 0.669 MeV for the known masses, and it extrapolates very well towards neutron rich nuclei, with an average error of 0.448 MeV for the region $N > 65$. However, there are not huge differences to other mass models such as HFB21 [80]. As an example Fig 3.2 shows the predicted Q values for the electron capture for the mass chain $A = 56$.

3.4.2   Hilf mass model

The Hilf mass formula is a semi-empirical atomic mass formula [79]. The mass M is separated into an average part $\bar{M}$ descried by the droplet model (DM) of Myers and Swiatecki [81] and
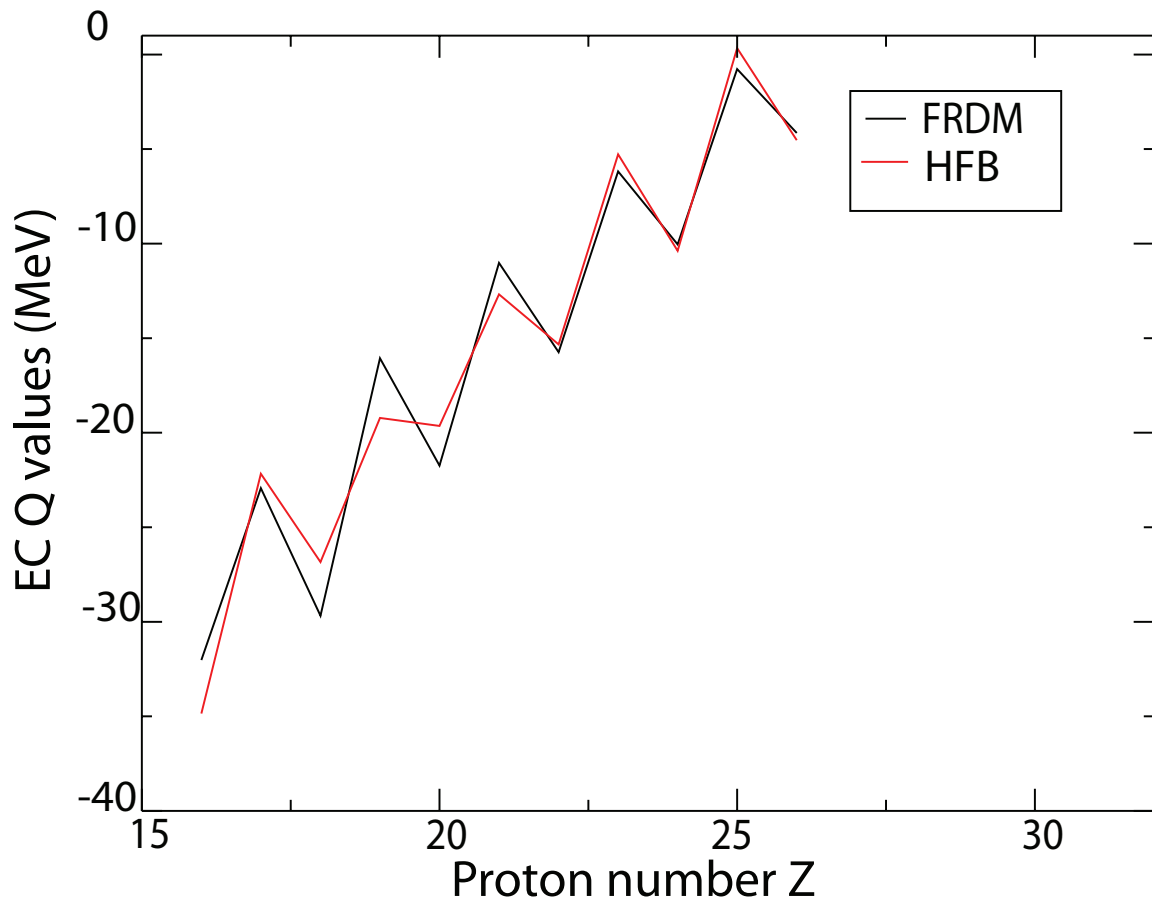
Figure 3.2: The electron capture Q-value for FRDM and HFB21 mass models for mass $A = 56$ as a function of proton number.

a microscopic term $\tilde{M}$ such that:

$$M = \bar{M} + \tilde{M} \tag{3.38}$$

$$M(N, Z) = \bar{M}(N, Z, \theta) + M_{\text{pair}}(N, Z) + M_{\text{W}}(N, Z) + \tilde{M}(N, Z, \theta) \tag{3.39}$$

where M_{pair} is the pairing term, M_{W} is the Wigner term, and $\tilde{M}$ is the shell correction. The shell correction term $\tilde{M}$ is derived by bunching the average single-particle spectrum from a Fermi gas model. Inner shells' effects, changing magicities along neutron magic isotone chains, damping of the off-Fermi-energy shell contributions, and nuclear deformation are all included. The mass formula is an analytic expression with 50 parameters fit, and a rms error of 670 keV.

In this thesis the mass formula is mainly needed for extremely neutron rich light nuclei. Figure 3 shows the Masses for the Hilf mass model and the experiment mass with $Z = 6$.

3.5   Numerical Methods

The crust model code calculates composition and energy generation as a function of depth in a steady state approximation. Following the fate of an accreted fluid element increasing time means increasing depth and pressure. For each time step pressure is evolved according to the accretion rate:

$$\delta P(t) = g\dot{m}\delta t \tag{3.40}$$

where P is the pressure, g is the surface gravity, and $\dot{m}$ is the mass accretion rate per unit area. For a temperature profile provided as input, the EOS routine (as mentioned in chapter3.1) calculates the density taking into account electron, neutron and ion abundances.
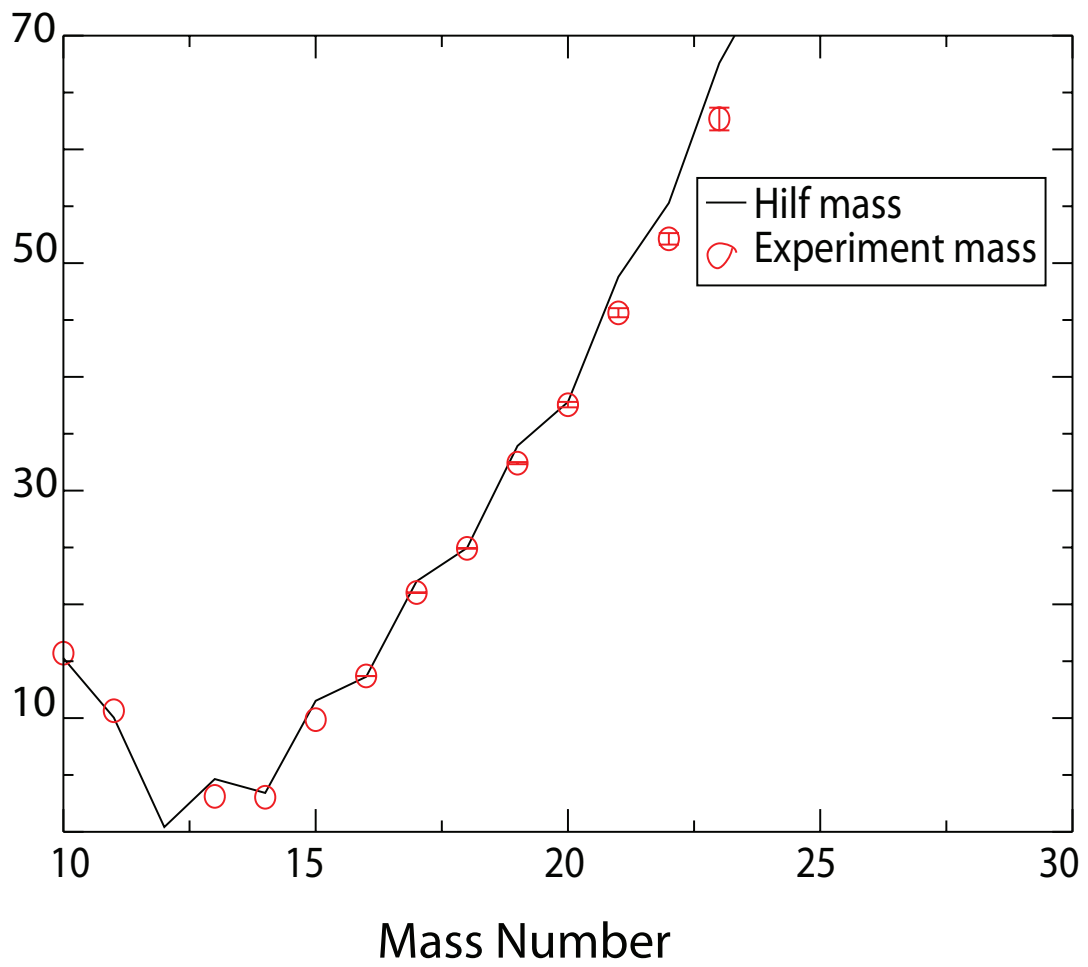
Figure 3.3: TMass excess calculated with the Hilf mass model and from experiment for carbon isotopes.

For the resulting temperature and density conditions the nuclear abundance changes are calculated using a reaction network solver for the abundances $Y_i(t)$ provided by Hix and Thielemann [82]. The energy released is calculated using:

$$dQ = dE_\mathrm{nuc} + dE_e - dE_\nu \qquad (3.41)$$

where $dE_\mathrm{nuc} = \sum_i dY_i BE_i$ is the nuclear energy generation calculated from the abundance change dY_i and binding energy BE_i of each isotope i. $dE_\mathrm{e} = \mu_\mathrm{e} dY_\mathrm{e}$ where μ_e is the Fermi energy of the electrons is the energy change due to changes in electron abundance. dE_ν is the energy released as neutrinos from electron capture. Once the calculation is completed and all heat sources are calculated, a new thermal profile is calculated using the thermal model from Ed Brown described in section 3.1.

The nuclear reaction network solver by Hix and Thielemann [82] solves the coupled first order differential equations for the abundance of each isotope as a function of time. The rate equations can be divided into 3 main categories. One category is reactions involving a single nucleus, such as electron captures, beta decay and photodisintegrations. For reaction involving two nuclei, such as neutron capture and pycnonuclear fusion, the reaction rate depends on the number densities of both target and projectile nuclei. There are also a few three particle processes but they are not important in our network. The reaction network is described by the following set of differential equations [49]:

$$\frac{dY_i}{dt} = \sum N_j^i \lambda_j Y_j + \sum N_{j,k}^i \rho N_A < \sigma\nu >_{j,k} Y_j Y_k \qquad (3.42)$$

where the three sums are over reactions which produce or destroy a nucleus of species i with

1, 2 reactant nuclei, respectively. λ represents the rate for a one body reaction and $<\sigma\nu>$ represents the energy averaged astrophysical reaction rate of the two body or three body reactions. The N^i's can be positive or negative numbers that specify how many particles of species i are created or destroyed in a reaction. The nuclear abundance depends on the number density n_i as $Y_i = n_i/\rho N_A$, where N_A is Avogadro's number. For a nucleus with atomic weight A_i, A_iY_i is the mass fraction of this nucleus, and $\sum A_iY_i = 1$.

Because our network includes strong, weak and electromagnetic reactions, we have a wide range of timescales. Systems whose solutions depend on a wide range of timescales are termed stiff. Thus an implicit approach for solving the reaction network is essential. There are explicit differencing schemes and implicit differencing schemes. An explicit differencing scheme is

$$\frac{1}{\Delta t}[Y_i(t+\Delta t) - Y_i(t)] = r_i(Y(t)) \tag{3.43}$$

where r_i defines the rate of change of species i. Explicit schemes require too small timesteps for a practical calculation. An implicit differencing scheme is

$$\frac{1}{\Delta t}[Y_i(t+\Delta t) - Y_i(t)] = r_i(Y(t+\Delta t)) \tag{3.44}$$

where the abundance change is calculated using rates evaluated with the new abundances. The code employed here use an implicit differencing scheme which allows larger timesteps. The equation above can be solved by the Backward Euler Method. r_i can be expanded as:

$$r_i(Y(t+\Delta t)) = r_i(Y(t)) + \sum_j \frac{\delta f_i}{\delta Y_j}\Delta Y_j + ... \tag{3.45}$$

where $f_i = dY_i/dt$

43

Replacing $r_i(Y(t+\delta t))$ by equation 3.44, we get

$$\frac{1}{\Delta t}[Y_i(t+\Delta t) - Y_i(t)] = r_i(Y(t)) + \sum_j \frac{\delta f_i}{\delta Y_j}\Delta Y_j + ... \tag{3.46}$$

Writing the Jacobian matrix $J_{ij} = \frac{\delta f_i}{\delta Y_j}$ and $[Y_i(t+\Delta t) - Y_i(t)] = \Delta Y_i$:

$$\frac{1}{\Delta t}\Delta Y = r_i(Y(t)) + \sum_j J_{ij}\Delta Y_j + ... \tag{3.47}$$

Rearranging and writing in vector/matri form we get

$$\vec{r_i}(Y(t)) = \frac{\Delta \vec{Y}}{\Delta t} - \tilde{J}\Delta \vec{Y} \tag{3.48}$$

Solving for ΔY, we get:

$$\Delta Y = \vec{r_i}(Y(t))(\frac{1}{\Delta t} - J)^{-1} \tag{3.49}$$

Here we use the subroutine DEGSV in Lapack to invert the Jacobian matrix. In our code, we first determine a trial timestep Δt using the following equation:

$$\Delta t = \frac{f \times \Delta_{\max} \times Y}{\dot{Y}} \tag{3.50}$$

where f is 1.00×10^{-2} and $\Delta_{\max}$ is set by the user to be 1.00×10^{-1}. In order to minimize noise effects in the network, abundances lower than 1.0×10^{-30} are set to zero. In order to avoid unnecessary tracking of very small abundances, only nuclei with abundances greater than 1.0×10^{-6} are used for timestep determination. The smallest timestep allowed by the program is time $t \times 1.0e \times 10^{-15}$ s because of numerical precision. The timestep is also

44

further restricted to be at most 2 times the previous timestep.

The network is evolved to time t+tdel and mass convergence is tested. The mass fraction $\sum A_i \times dY_i$ is compared with the previous timestep to check if the change is larger than 1.0×10^{-6}. If yes, the timestep is cut by half and the evolution is redone. If the mass convergence test is passed, the next step is a test to ensure the code has not stepped over the onset of an electron capture reaction. The electron capture rates have sharp thresholds with the rates prior to threshold being very small (resulting in the code to choose very long time steps) and with the rates beyond the threshold dramatically increasing. In order to make sure the code did not step over the onset of an electron capture rate, we compute dy/dt at the new time and ensure:

$$\frac{y(t + \Delta t)}{\dot{y}} < \Delta t \times 10 \tag{3.51}$$

If the code fails in the above test, tdel will be cut in half, and the abundance evolution will be redone again. The process above will be continued until all the tests are passed.

Chapter 4

Results

The initial composition for crust model calculations varies from system to system depending on the composition of the accreted matter and the characteristics of surface burning processes such as X-ray bursts and superbursts. As a starting point a calculation using an initial abundance of ^{56}Fe is presented. This is not necessarily a realistic case as typically the initial composition will be a mix of different isotopes. But it is a good study example to simplify the situation and to understand the general picture of the fate of the ashes. In addition, the results can be directly compared to several previous studies such as [17], which also used an initial ^{56}Fe composition. Once ^{56}Fe is discussed, we investigate the crust processes for other initial single species compositions. Finally, realistic superburst ashes are used to understand the crust processes for more realistic multi species compositions.

4.1 ^{56}Fe

The neutron star crust simulation was performed assuming an initial ^{56}Fe abundance with a mass fraction equal to 1 (see Fig.4.1.). The evolution starts at time 1.00×10^6 s, a
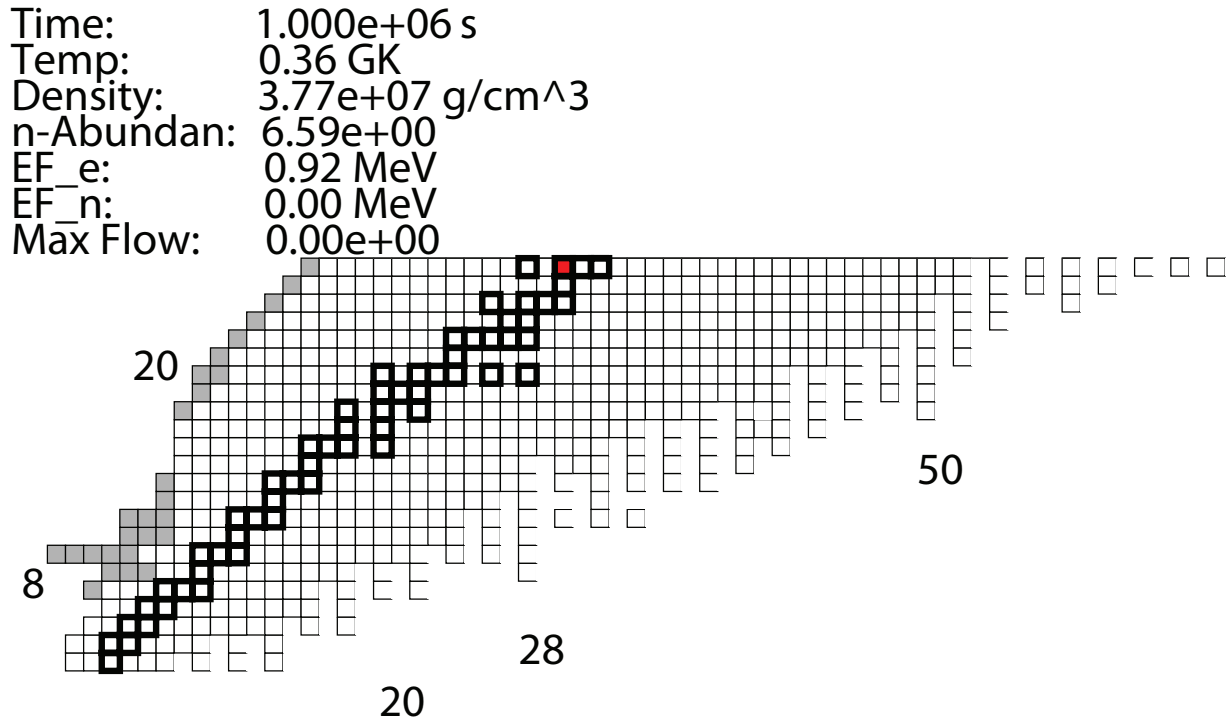
Figure 4.1: The initial composition in the chart of nuclides. Abundances are shown on a logarithmic color scale from blue (lowest) to green to yellow to orange to red (highest) with a lower cutoff at 1.0×10^{-15}. Thick black squares indicate stable nuclei and thin black squares unstable but particle bound nuclie. Particle unbound nuclei don't have an outline but can still be part of the network. Nuclides that are not part of the network are shaded gray.

mass density of 3.77×10^7 g cm^{-3}, and an electron Fermi energy of 0.919 MeV. The initial temperature is 0.36 GK. The initial mass density, electron Fermi energy and temperature are determined by the choice of initial time. The initial time is directly related to the initial depth at which the calculation begins. This initial depth was chosen such that it is well above the point where ^{56}Fe begins to capture electrons. The simulation ends at time 1.00×10^{13} s with a final temperature of 0.46 GK and a final mass density of 2.63×10^{13} g cm^{-3} near the bottom of the crust (see Fig.4.2.). The electron Fermi energy is 35.42 MeV at this density.

For readers' convenience, Figure 4.3 shows the relationship of different physical quantities (time, pressure, column depth, density, electron Fermi energy).

At time 5.4×10^8 s, density 3.94×10^9 g cm^{-3} and $E_F \sim 6.0$ MeV, ^{56}Fe which has

Time: 5.806e+12 s
Temp: 0.47 GK
Density: 1.79e+13 g/cm^3
n-Abundan: 9.33e-01
EF_e: 36.20 MeV
EF_n: 4.80 MeV
Max Flow: 1.84e-05
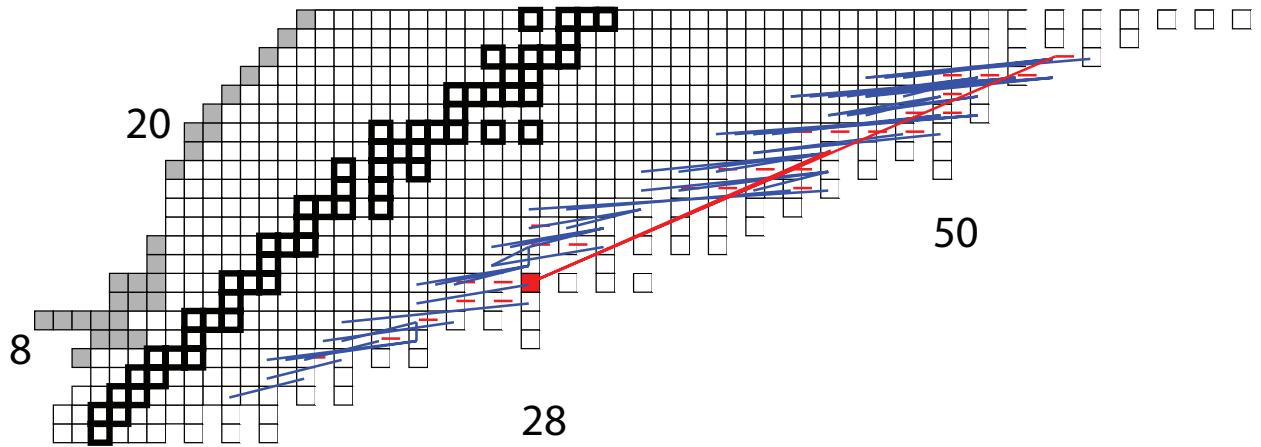
Figure 4.2: Final composition. The lines denote "instantaneous" net reaction flows for the timestep displayed. Red lines show flows in the direction of increasing neutron number, blue lines flows in the direction of decreasing neutron number. See. Fig. 4.1. for additional information.
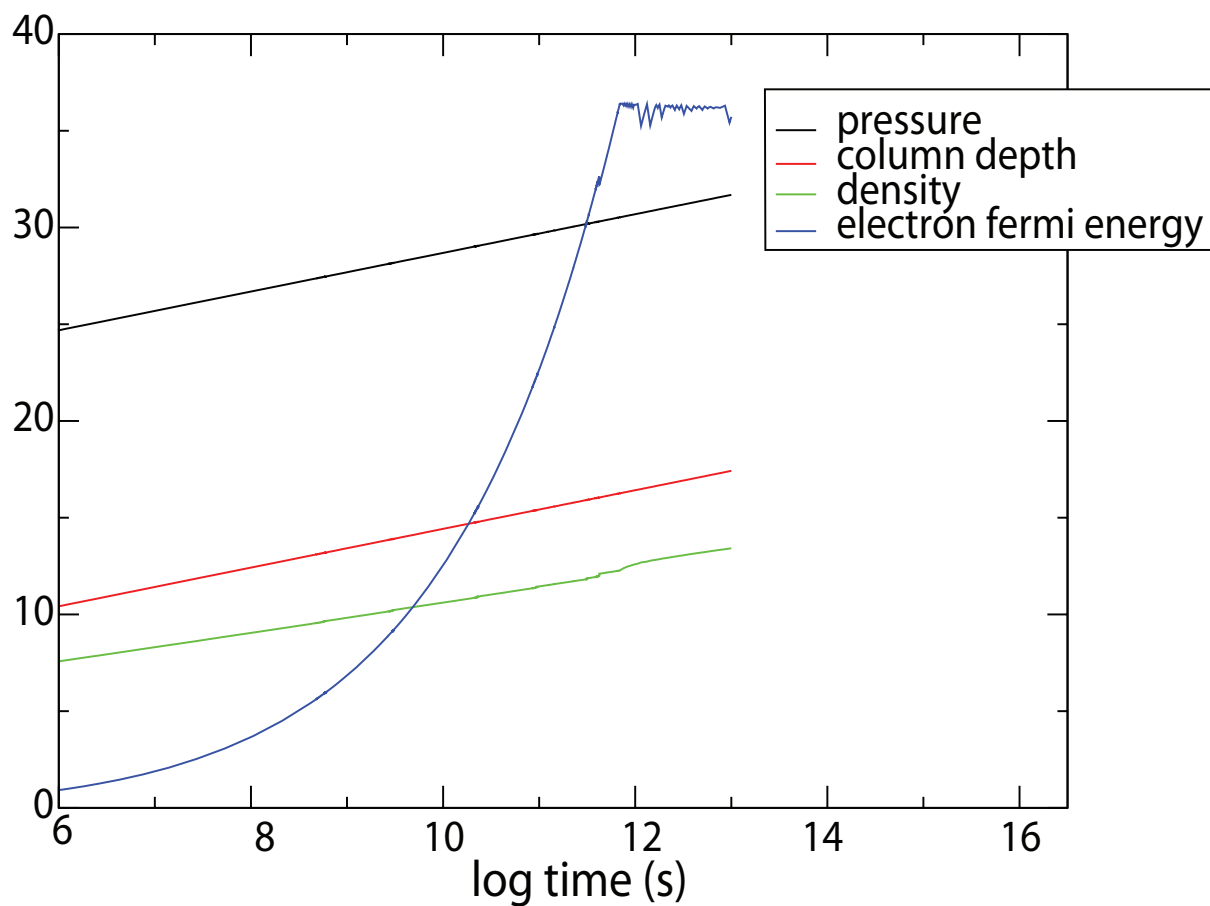
Figure 4.3: The relationship between time (s), log pressure (dyn cm^{-2}), log column depth (g cm^{-2}), log density (g cm^{-3} and electron Fermi energy(MeV)

an electron capture threshold of 6.2156 MeV (Q values plus excitation energy) undergoes electron capture to ^{56}Mn. Experimentally it was found that there is lower lying GT strength in ^{56}Mn but as experimental information is not avaliable for the vast majority of transitions this work uses only theoretical strength functions. ^{56}Mn has an electron capture threshold of 4.8096 MeV, which is lower than the ^{56}Fe electron capture threshold and further undergoes electron capture to ^{56}Cr. Thus a two step electron capture occurs due to the odd-even mass staggering of the nuclei. The electron capture occurs for a Fermi energy below the threshold because the thermal energy $\sim kT$ excites part of the electrons to higher energies. Figure 4.4 shows the reaction flow of the electron capture from ^{56}Fe to ^{56}Cr. The flow F is calculated by time integration of the flux $\frac{dY_i}{dt}$ by the following equation:

$$F_{i \to j} = \int \left(\frac{dY_i}{dt}_{i \to j} - \frac{dY_i}{dt}_{j \to i} \right) dt \tag{4.1}$$

where flux $\frac{dY_i}{dt}$ is calculated by the following equations:

For 1 reactant

$$\frac{dY_i}{dt}_{i \to j} = \rho < \sigma\nu >_{1,i} y_i \tag{4.2}$$

where $< \sigma\nu >$ is the product of cross section and relative velocity averaged over the Maxwell-Boltzmann velocity distribution. Y is the abundance and ρ is the density.

For 2 reactants,

$$\frac{dY_i}{dt}_{i \to j} = \rho < \sigma\nu >_{2,i,j} y_i y_j / \delta_{i,j} \tag{4.3}$$

The flows shown in Figures 4.2. and 4.4. are instantaneous flows. That is, they are integrated over one timestep and the timestep is determined by the code as explained in section 3.4. The figure 4.2 also shows the main flows only while the weak flows are suppressed.

50
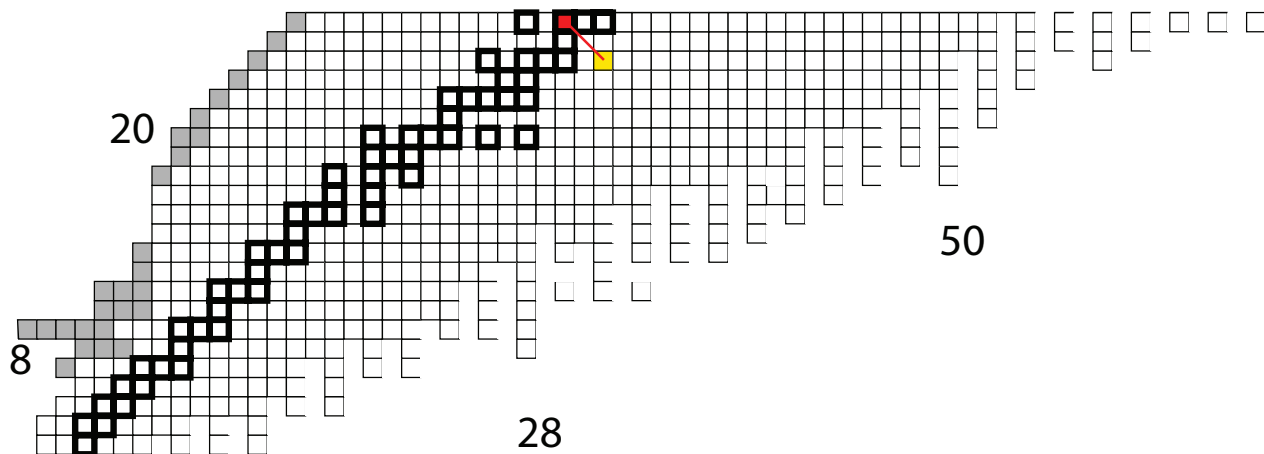
Figure 4.4: The two step electron capture process from ^{56}Fe to ^{56}Cr (see Fig.4.1 and 4.2 for details)

At time 3.4 $\times 10^9$ s, density 1.67×10^{10} g cm^{-3}, and $E_F \sim 9.00$ MeV, ^{56}Cr, which has an electron capture threshold of 9.25 MeV (Q value plus excitation energy), undergoes electron capture to ^{56}V. ^{56}V has an electron capture threshold of 7.143 MeV and undergoes electron capture to ^{56}Ti. ^{56}V has a β^- decay Q-value of 9.20 MeV. The electron Fermi energy is not high enough therefore to block the β^- decay and some ^{56}V β decay back to ^{56}Cr. This leads to some URCA type cycling between ^{56}Cr and ^{56}V and the associated neutron emission leads to some cooling at this location (the possibility of such an effect had been pointed out by Gupta et al.)

At time 2.0 $\times 10^{10}$ s, density 7.02×10^{10} g cm^{-3}, neutron abundance 1.78 $\times 10^{-22}$, and $E_F \sim 15.09$ MeV, ^{56}Ti, which has an electron capture threshold of 15.75 MeV undergoes electron capture to ^{56}Sc. ^{56}Sc, which has an electron capture threshold of 14.56 MeV under-

51

goes electron capture to ^{56}Ca. Figure 4.6 shows the abundance versus time for the electron captures so far. Clearly the transition regions are rather narrow owing to the sharp turnon of the electron captures, though the width is not negligible.

At time 8.6×10^{10} s, density 2.26×10^{11} g cm^{-3}, neutron abundance 9.81×10^{-20}, and $E_{\mathrm{F}} \sim 21.79$ MeV, ^{56}Ca undergoes electron capture to ^{56}K. ^{56}K then electron captures and emits neutrons to ^{54}Ar while at the same time the released neutrons are captured by ^{56}Ca producing ^{57}Ca, which then electron capture to ^{57}K and undergoes further electron capture with neutron emission to ^{56}Ar. The simultaneous occurrence of neutron capture and electron capture on ^{56}Ca happens because the immediately following electron capture on ^{56}K leads to significant neutron emission. This leads to a buildup of a neutron abundance of 9.81×10^{-20}, leading to a significant neutron capture branch before all ^{56}Ca has had a chance to capture electrons. The neutron captures are effective as ^{56}Ca lies on the neutron deficient side of the (n,γ)-(γ,n) equilibrium point. The result is a split of the reaction path with one branch moving to neutron rich Ca isotopes via neutron capture and the other branch moving to lower Z via electron captures (and of course neutron captures as well). This is very different from Haensel & Zdunik [17] where ^{56}Ca is directly converted to ^{56}Ar without a splitting of the reaction path. The difference comes from our consideration of realistic finite electron capture rates, as opposed to infinite fast electron capture in Haensel & Zdunik.

At time 1.4×10^{11} s, density 3.69×10^{11} g cm^{-3}, $E_{\mathrm{F}} \sim 23.61$ MeV, and neutron abundance 3.0×10^{-17}, ^{52}Ar electron captures and neutrons emissions to ^{51}Cl and then electron capture and neutron emissions to ^{48}S. At the same time ^{58}Ca further neutron captures to ^{60}Ca and ^{62}Ca. ^{58}Ca also has an electron capture branch ane neutron emissions to ^{57}K and then to ^{54}Ar, ^{56}Ar.
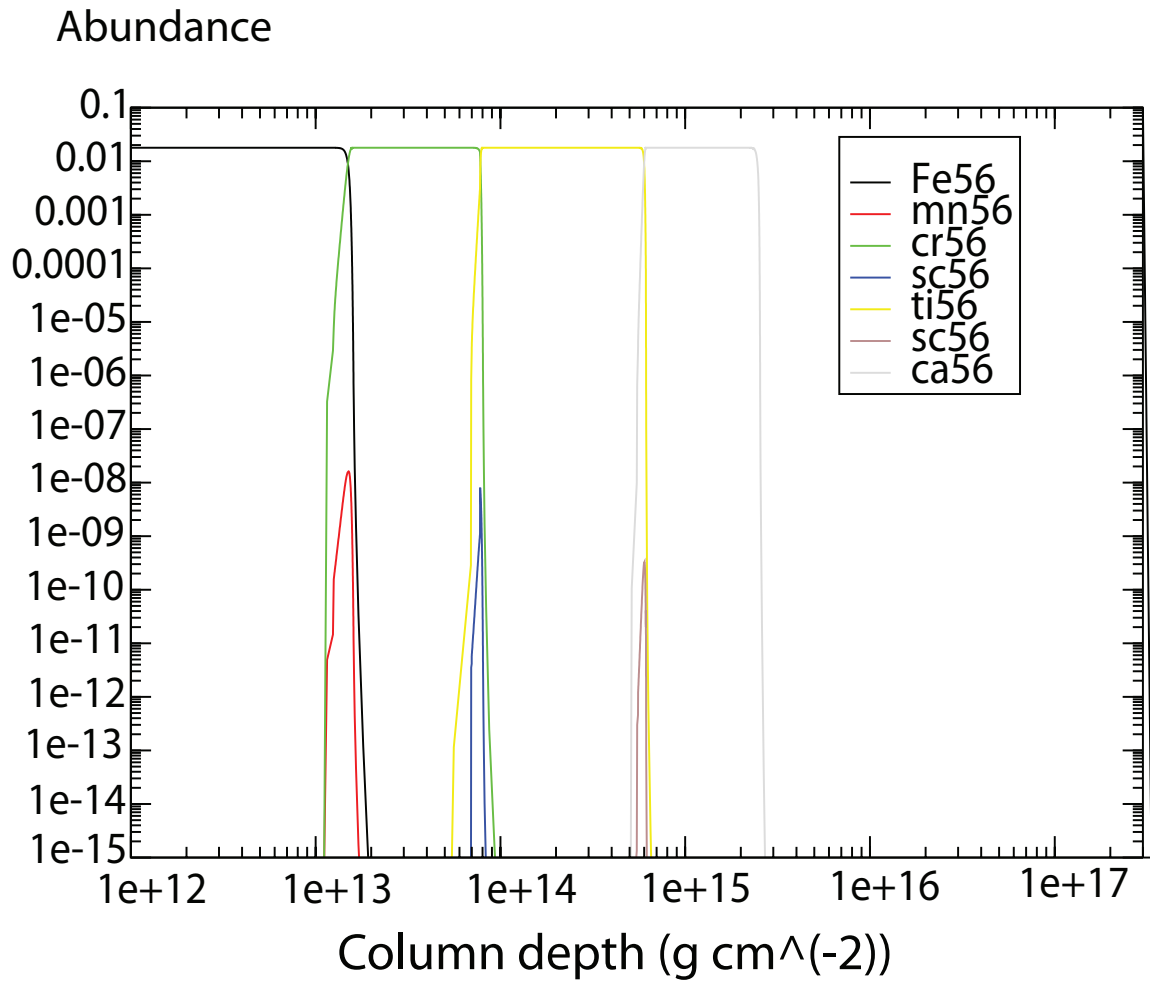
Figure 4.5: Abundance as a function of column depth for ^{56}Fe, ^{56}Mn, ^{56}Cr, ^{56}V, ^{56}Ti, ^{56}Sc, ^{56}Ca
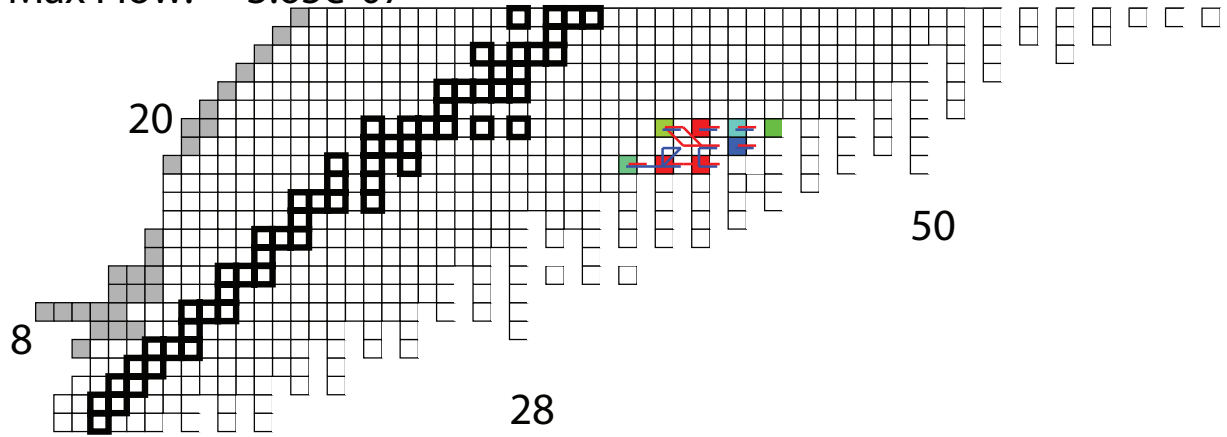
Figure 4.6: The fluxplot shows the splitting of the path at time 9.638×10^{10} s. (See Fig. 4.1. and 4.2. for details)

At time 2.0×10^{11} s, density 4.70×10^{11} g cm^{-3}, neutron abundance 2.75×10^{-17}, and $E_{\rm F} \sim 26.99$ MeV, ^{48}S is partially converted by a sequence of electron captures with neutron emission into ^{42}Si, with the remainder neutron capturing to ^{50}S.

At time 2.2×10^{11} s, density 5.12×10^{11} g cm^{-3}, $E_{\rm F} \sim 27.78$ MeV, and neutron abundance 1.10×10^{-10}, ^{50}S also undergoes electron capture with neutron emissions ending up in ^{42}Si. ^{62}Ca finally also starts electron capturing into ^{56}Ar.

At time 3.0×10^{11}s, density 6.43×10^{11} g cm^{-3}, $E_{\rm F} \sim 30$ MeV, and neutron abundance 2.08×10^{-08}, a small amount of ^{42}Si (EC threshold 30.39 MeV) does electron capture to ^{41}Al (EC threshold 29.72 MeV) and then to ^{36}Mg. Most ^{36}Mg is then converted by neutron capture into ^{40}Mg because of the high neutron capture rate. However, there is again a splitting of the path as electron capture can compete with neutron capture. Therefore some ^{36}Mg (EC threshold 26.85 MeV) does further electron capture to ^{34}Na and ^{35}Na. Within

the time $3.0 \times 10^{11} - 3.1 \times 10^{11}$s, the net flux for the neutron capture of ^{36}Mg is 5.25×10^{-4}. The flux for going to ^{34}Na, ^{35}Na are 1.33×10^{-4} and 1.479×10^{-4} respectively. The flux towards lighter nuclei below Mg is therefore significant (or the order of 50%). ^{34}Na, ^{35}Na (EC threshold 24.11 MeV, 25.72 MeV) do further electron capture to ^{31}Ne and neutron capture to ^{32}Ne. ^{32}Ne (EC threshold 30.35 MeV) undergoes electron capture to ^{31}F. ^{31}F (EC threshold 29.02 MeV) coverts to ^{24}O (EC threshold 27.93 MeV) and then into ^{23}N. ^{23}N (EC threshold 28.63 MeV) then undergoes electron capture to ^{18}C. ^{18}C (EC threshold 28.47MeV) does electron capture to ^{17}B. Some of the ^{18}C neutron captures to ^{20}C. As we can see, some of the heavier isotopes are converted all the way down to very light isotopes (^{17}B) within very short range of electron Fermi energy ($\sim$ 1MeV). This is the super electron capture cascade also found in [20]. When nuclei reach low neutron separation energies electron capture tends to occur into excited states of the daughter nuclei that can lie significantly above the thresholds for multiple neutron emission. Thus, the nuclei undergo electron capture and emit neutrons. We find neutron emission up to 7 neutrons to be significant at this early stage. Because the neutron emission leads to the formation of a daughter nucleus with lower electron capture threshold, an electron capture, again, accompanied by neutron emission, immediately follows. This happens because the electron capture rate for such low threshold nuclei is higher than the neutron capture rates. The process then repeats until neutron capture wins (as is partially the case for ^{36}Mg, where a neutron capture branch leads to ^{40}Mg with a high electron capture threshold ending the cascade) or pycnonuclear fusion sets in. As a result high Z nuclei can be converted to low Z nuclei and a large amount of neutrons within a short range of electron Fermi energy. Thus, the nuclei now have Z values that are low enough for pycnonuclear fusion to occur. ^{17}B, ^{18}C, ^{23}N, ^{24}O, ^{32}Ne fuse to form heavier

elements. This is a major difference to Haensel and Zdunik, where fusion of neon at much greater depth (4.379×10^{12} g cm^{-3} as opposed to 6.40×10^{11} g cm^{-3} here) are the first pycnonuclear reactions to occur. In our calculation, the super electron capture cascade effect [Gupta] converts some fraction of the material into very low Z isotopes at relatively shallow depths. Because of the lower Coulomb repulsion those nuclei can readily undergo fusion. Figure 4.7 shows the reaction flow from ^{56}Ar down to ^{18}C and ^{18}C neutron captures to ^{20}C and it fuses with itself to form ^{40}Mg. Some ^{32}Ne also fuses with ^{20}C to form ^{52}S. These are the first pycnonuclear fusions.

However, the super electron capture cascade does not covert all nuclei into lighter species. Along the way towards lighter elements there are branchings where neutron capture can compete with electron capture, moving some abundance into more neutron rich species with high electron capture thresholds, where the reaction flow has to wait for the electron Fermi energy to rise to include electron capture, or the neutron density to raise to shift the equilibrium towards more neutron rich isotopes. These waiting points are ^{56}Ar, ^{62}Ar, ^{50}S, ^{42}Si, ^{40}Mg, and ^{32}Ne (see Fig 4.7).

One of the nuclei produced in the initial super electron cascade is ^{32}Ne. It is subsequently destroyed by fusion with lighter isotopes. So not only does one have early fusion, one also destroys neon causing the next major fusion step to be Mg fusion instead of Ne fusion as in Haensel and Zdunik [17]. Because of this in our model Ne fusion is essentially skipped and after the first initial fusion events, the major next pycnonuclear fusion is delayed compared to Haensel and Zdunik.

At time 3.4×10^{11} s, density 7.69×10^{11} g cm^{-3}, $E_\mathrm{F} \sim 30.84$ MeV, and neutron abundance 5.43×10^{-06}, ^{50}S neutron captures to ^{56}S while ^{42}Si neutron captures to ^{46}Si.

Time: 3.055e+11s
Temp: 0.50 GK
Density: 6.49e+11 g/cm^3
n-Abundan: 8.70e-10
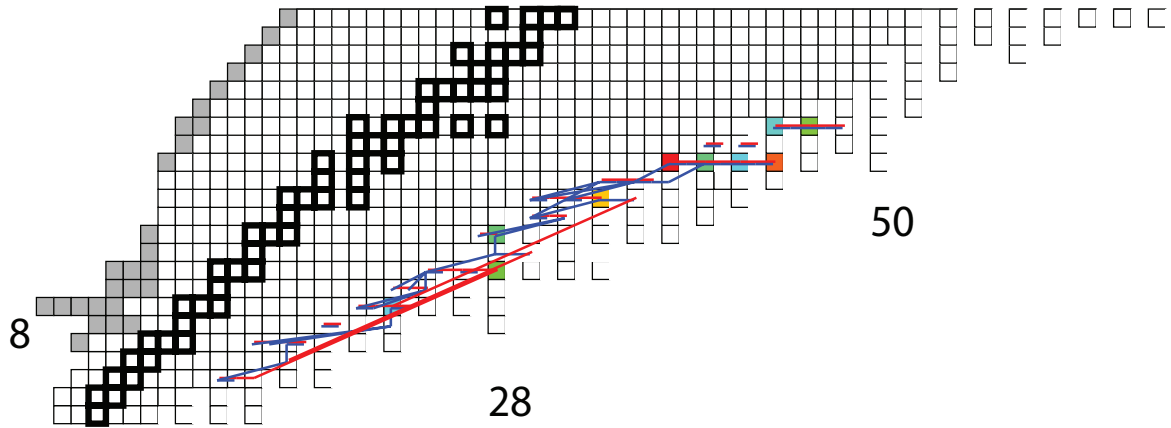EF_e: 30.11 MeV
EF_n: 0.00 MeV

50

8

28

Figure 4.7: The fluxplot shows the small amount of ^{56}Ar does electron capture down to ^{18}C and the first pycnonuclear fusion. The red lines from low Z to high Z show pycnonuclear fusion. (see Fig.4.1 and 4.2 for details)

At time 4.046×10^{11} s, density 9.35×10^{11} g cm^{-3}, neutron abundance 1.68×10^{-02}, and $E_F \sim 32.32$ MeV, some ^{62}Ar neutron captures to ^{64}Ar and some electron captures to ^{57}Cl followed by neutron captures to ^{61}Cl. ^{56}S neutron captures to ^{58}S.

At time 4.071×10^{11} s, density 9.40×10^{11} g cm^{-3}, and $E_F \sim 33.69$ MeV, ^{62}Ar has a large electron capture rate which acts as a pump to pump away the equilibrium Ar isotopes. As a consequence ^{64}Ar (γ, n) to ^{62}Ar which undergoes electron captures with neutron emissions as well as neutron capture to ^{61}Cl. ^{58}S (γ, n) to ^{56}S and undergoes electron capture and 13 neutron emissions followed by neutron capture to ^{45}P. ^{45}P undergoes electron capture and 5 neutron emissions to ^{42}Si and neutron capture to ^{46}Si. At this point in time the composition consists mainly of ^{46}Si, ^{61}Cl, and ^{40}Mg. ^{40}Mg is still unchanged because of its very large threshold for electron capture and the very low neutron capture Q-value of 4.69 MeV, which leads to an extremely small neutron capture rate of 2.06×10^{-45}. In fact, (n, γ)-(γ, n)

equilibrium is located towards more neutron rich isotopes, which however cannot be reached by the system because of the small neutron capture rate.

At time 4.801×10^{11} s, density 1.06×10^{12} g cm^{-3} and $E_{\mathrm{F}} \sim 33.75$ MeV, ^{40}Mg fuses with ^{40}Mg to form ^{80}Cr. This is the first major fusion event where the isotope that constitutes the main composition is fusing with itself. ^{80}Cr is immediately converted to light nuclei via a super electron capture cascade, with some fraction branching back to ^{40}Mg and some fraction further being converted to lighter nuclei.

At time 5.512×10^{11} s, density 1.56×10^{12} g cm^{-3}, neutron abundance 3.35×10^{-1}, and $E_F \sim 34.42$ MeV, electron capture with neutron emissions converts ^{61}Cl into ^{44}S, which neutron captures into ^{50}S. ^{50}S does electron capture to ^{43}P then neutron captures to ^{47}P. ^{47}P then electron captures to ^{40}Si followed by neutron captures to ^{42}Si. At ^{42}Si another branching occurs. Some material undergoes electron capture down to ^{41}Al and then to ^{36}Mg which then neutron captures to ^{40}Mg. Some ^{42}Si however undergoes further neutron capture to ^{46}Si.

At time 6.5×10^{11} s, density 1.75×10^{12} g cm^{-3}, $E_{\mathrm{F}} \sim 35.97$ MeV, neutron abundance 3.43×10^{-1}, ^{46}Si then electron captures to ^{41}Al and then to ^{36}Mg, which neutron captures to ^{40}Mg. At this point all the major waiting points have been converted into ^{40}Mg and free neutrons. ^{40}Mg is a special waiting point because with $N = 28$ it has a closed neutron shell. Its neutron capture Q-value is 4.69 MeV resulting in a essentially non-existent neutron capture rate, and a very high electron capture threshold of 37.03 MeV. β decay is Fermi blocked. Therefore it is essentially stable at this stage, and all other nuclei are eventually converted to ^{40}Mg. This is very different from the Haensel and Zdunik [17] calculation, which did not include shell effects. ^{40}Mg continues to fuse with itself to form ^{80}Cr which is

immediately converted into lighter nuclei by super electron capture cascades. The flow to lighter nuclei branches in part into ^{40}Mg essentially forming a cycle, and in part continues into the nitrogen and carbon region, where these isotopes then fuse mostly with ^{40}Mg forming subcycles. During the process, neutrons are kept being emitted. Essentially one loop in the ^{40}Mg-^{80}Cr cycle converts one ^{40}Mg nucleus into neutrons. Figure 4.2 shows the abundance distribution and reaction flows during this time. As the fusion reaction with ^{40}Mg is the slowest reaction in the cycle, ^{40}Mg is the only isotope that builds up a significant abundance. Figure 4.8 shows the most dominant abundance change of the isotopes in the deeper crust.

The branchings into different subcycles at ^{40}Mg can be analyzed quantitatively. During $1.0 \times 10^{12} - 1.0 \times 10^{13}$ s, there is a flux for 4.528×10^{-3} down to ^{33}N and a flux of 2.447×10^{-3} fluxesfor ^{40}Mg fusion to form ^{80}Cr. The flux for ^{23}N to fuse with ^{40}Mg is $2.905 \times 10^{-3}$and the flux for ^{20}C to fuse with ^{40}Mg is 1.00×10^{-3}. The 3 most dominant fusions overall are:

$$^{23}\text{N} +^{40} \text{Mg} \rightarrow^{63} \text{K} \tag{4.4}$$

$$^{40}\text{Mg} +^{40} \text{Mg} \rightarrow^{80} \text{Cr} \tag{4.5}$$

$$^{20}\text{C} +^{40} \text{Mg} \rightarrow^{60} \text{Ar} \tag{4.6}$$

The pycnonuclear fusion paths are very different from P.Haensel & Zdunik(1990)'s paper [17]. The 3 pycnonculear fusions that P.Haensel & Zdunik propose are ^{34}Ne + ^{34}Ne $\rightarrow^{68}$Ca, ^{36}Ne +^{36}Ne $\rightarrow^{72}$Ca and ^{48}Mg + ^{48}Mg $\rightarrow^{96}$Cr. In addition, they propose that after each fusion there is a successive step-wise electron capture sequence that transforms the nuclei back to lower Z isotopes while we find an essentially instantaneous conversion back to the initially fusing isotope (with some branchings to other isotopes). There are two main reasons
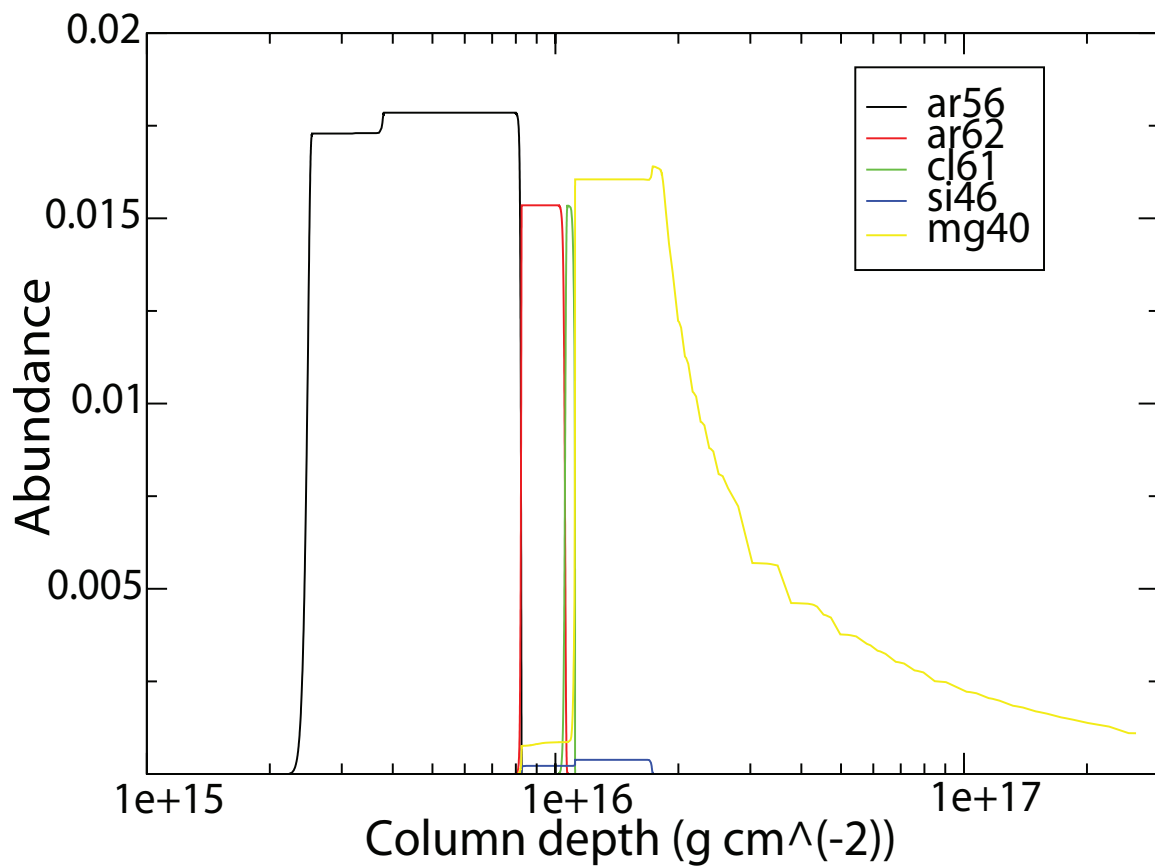
Figure 4.8: The abundance change of isotopes ^{56}Ar, ^{62}Ar, ^{61}Cl, ^{42}Si and ^{40}Mg versus the column depth. The decrease of ^{40}Mg at high column depth is because the continusous depletion by the pycnonuclear fusion cycles converting ^{40}Mg into neutrons.
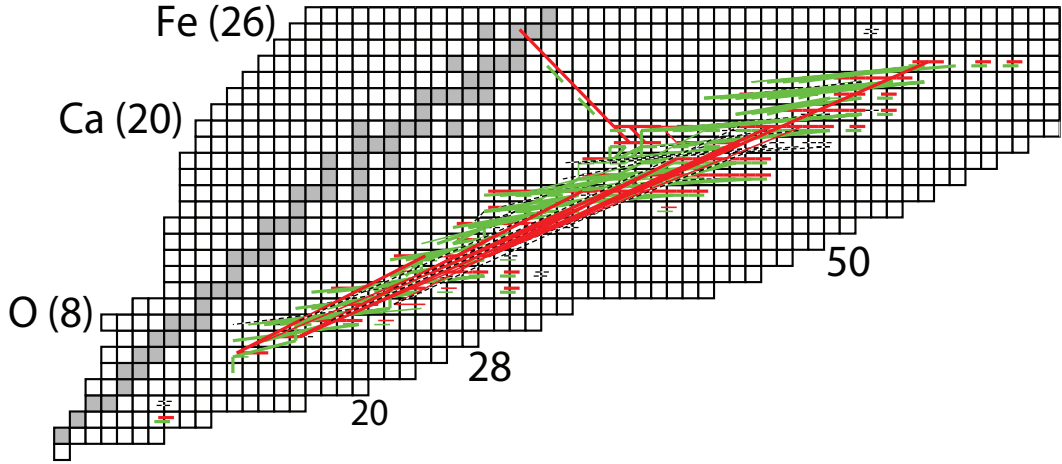
Figure 4.9: Time integrated reaction flows for the complete calculation with initial ^{56}Fe composition. See Fig 4.1. and 4.2. for details. The reaction flows towards lower neutron number are here green instead of blue.

for the difference. One is that the path splitting leads to formation of more than one nuclear species resulting in fusion reactions of unlike species. The other reason are shell effects resulting in the extremely low neutron capture rate and extraordinary high electron capture threshold of ^{40}Mg making it a major waiting point. Finally, the super electron capture cascade, a consequence of taking into account non-equilibrium neutron emission processes during electron capture, and the competition between electron capture and neutron capture, lead to a much more rapid conversion of pycnonuclear fusion products into light nuclei.

The final abundance distribution at the end of our calculation (E_{F}=36.20 MeV) is shown in the Fig 4.2. The composition is dominated by neutrons with an abundance of 0.956. The next dominant nuclide is ^{40}Mg with an abundance of 1.100×10^{-3} while ^{46}Si has an abundance of only 4.689×10^{-9}.

Figure 4.8 shows the total reaction flows integrated over the entire calculation of the crust.

Figure 4.10 shows the average charge number $< Z >$, and the average mass number

$< A >$ (which excludes neutrons) of the composition versus column depth (g cm^{-2}). At the beginning, in our model, $< A >$ remains unchanged while $< Z >$ stepwise decreases because of the electron capture processes. This is similar to Haensel & Zdunik [17] though their transitions occur at different locations because they assume ground state-ground state electron capture and because they use different nuclear masses. At a column depth of 8.0×10^{15} g cm^{-2}, $< A >$ increases because of a significant neutron capture branch in the reaction path. At column depth of 1.0×10^{16} g cm^{-2}, a sharp decrease in $< A >$, $< N >$ and $< Z >$ occurs due to the super electron capture cascade effect which is similar to Gupta et al for a ^{106}Pd case. Beyond a column depth of 1.0×10^{16} g cm^{-2}, $< A >$, $< Z >$ and $< N >$ remain constant at $< A >= 40$, $< Z >= 20$ and $< N >= 28$ since the composition remains mainly ^{40}Mg. This is a major difference to Haensel & Zdunik [17] where $< A >$ and $< Z >$ continue to increase by a factor of 2 due to pycnonculear fusion and then decrease due to electron capture and neutron emission. This pattern repeats for two cycles. However, we find that due to shell effect ^{40}Mg dominates the composition for a long time. In addition, after a pycnonuclear fusion reaction electron capture and neutron emission quickly process material back to ^{40}Mg forming rapid cycles due to the super electron capture cascade effect.

Figure 4.11 shows the integrated heat energy deposited into the crust of ^{56}Fe versus column depth (g cm^{-2}). The heat energy per nucleon deposited into the crust is calculated by equation 3.41. One heat source is electron capture reactions. To illustrate the heating process Figure 4.12 shows the nuclear level scheme and transitions involved. An electron is captured by the parent nucleus in its ground state (we neglect thermal excitations in our approach as temperatures are relatively low) to some excited state in the daughter nucleus. About 3/4 of the transition energy is carried away by the neutrino that is emitted
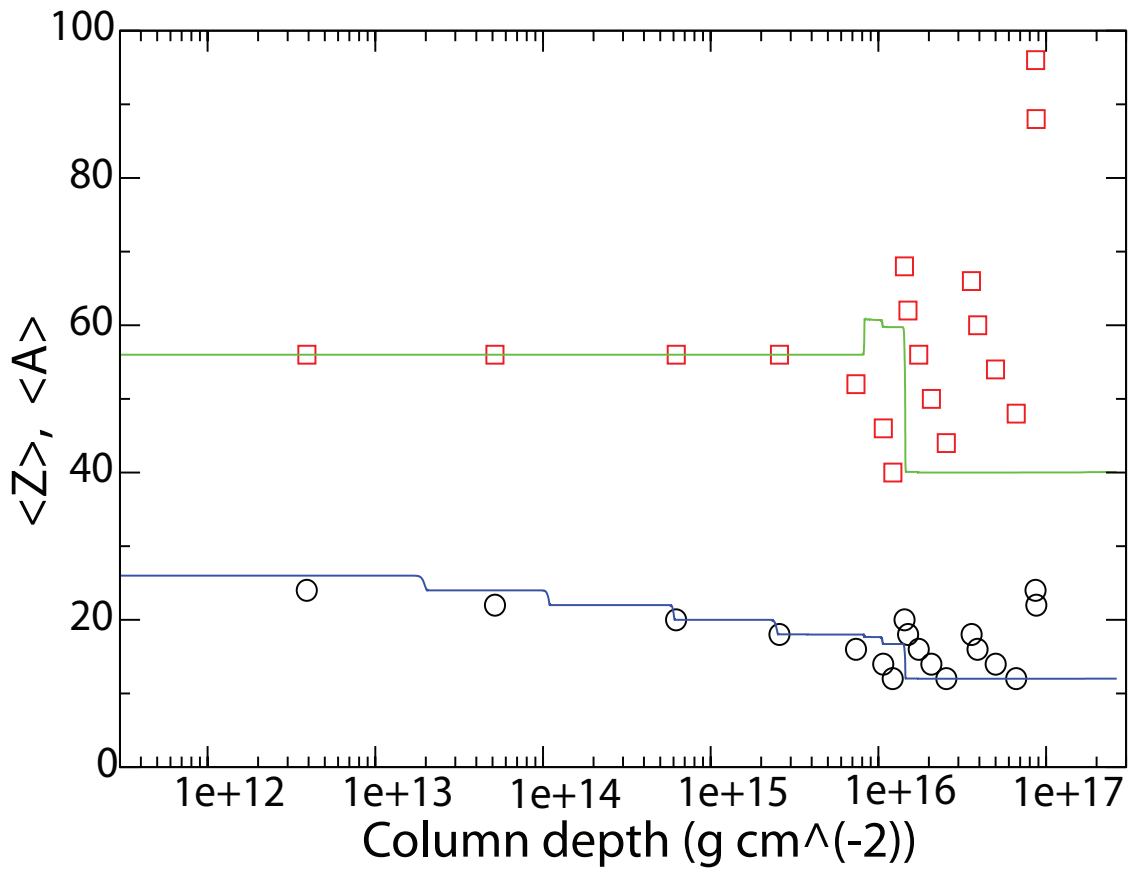
Figure 4.10: $< Z >$ (This work: blue line, Haensel & Zdunik: black circles) and $< A >$ (This work: green line, Haensel and Zdunik: red squares) versus column depth.

in this process. The excited daughter nucleus then deexcites to the ground state depositing its excitation energy as heat into the crust. Taking into account excited daughter states therefore reduces the neutrino energy loss significantly (Gupta et al) [19]. This is different from the Haensel&Zdunik [17] who assume electron capture proceeds from ground state to ground state which release much less energy because of the higher neutrino losses. We therefore obtain more heating. At a depth of 2.0×10^{16} g cm^{-2} the integrated deposited energy continues to increase smoothly and is not governed by individual electron capture transitions anymore. This is caused by energy released in pycnonuclear fusion reactions and the rapid electron capture sequences they induce. Our code shows a much higher energy deposition into the crust because of different pycnonuclear fusion paths.

Fig 4.13 shows another quantity characterizing the composition of the neutron star crust, the so called impurity parameter, which measures the diversity of nuclide charge numbers.It is an important parameter setting the conductivity of the crust [12]

$$Q_{\text{imp}} = n_{\text{ion}}^{-1} \sum n_i (Z_i - \langle Z \rangle)^2 \tag{4.7}$$

where n_{ion} is the total number density of ions, n_i is the number density of nucleus i and Z_i is the charge number of nucleus i. Figure 4.13 shows the impurity parameter versus column depth (g cm^{-2}). In the figure, five peaks appear at around 1.0×10^{13} g cm^{-2}, 8.0×10^{13} g cm^{-2}, 6.0×10^{14} g cm^{-2}, 3.04×10^{15} g cm^{-2} and 1.0×10^{16} g cm^{-2}. The first four peaks are due to the electron capture process which leads to coexistence of two species of nuclei at the same time. The fifth peak is due to the splitting of the reaction path. Beyond the fifth peak, the composition is dominated by ^{40}Mg which leads to a very pure crust with a very small impurity parameter.
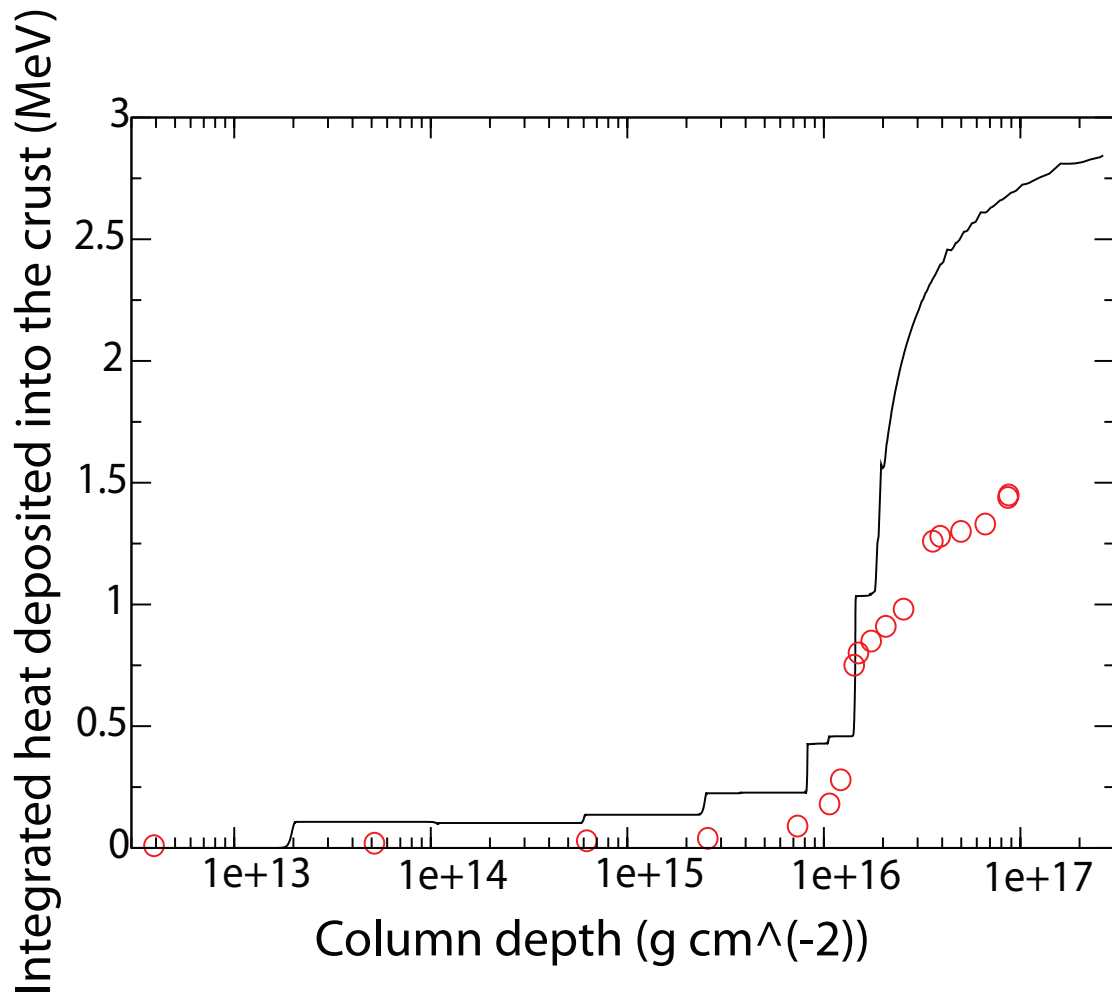
Figure 4.11: The energy generation (MeV per nucleon) versus the column depth (g cm^{-2}). The black line shows the heat deposited into the crust by our model and the red circles shows the table from P.Hasensl & Zdunik 1990 paper.
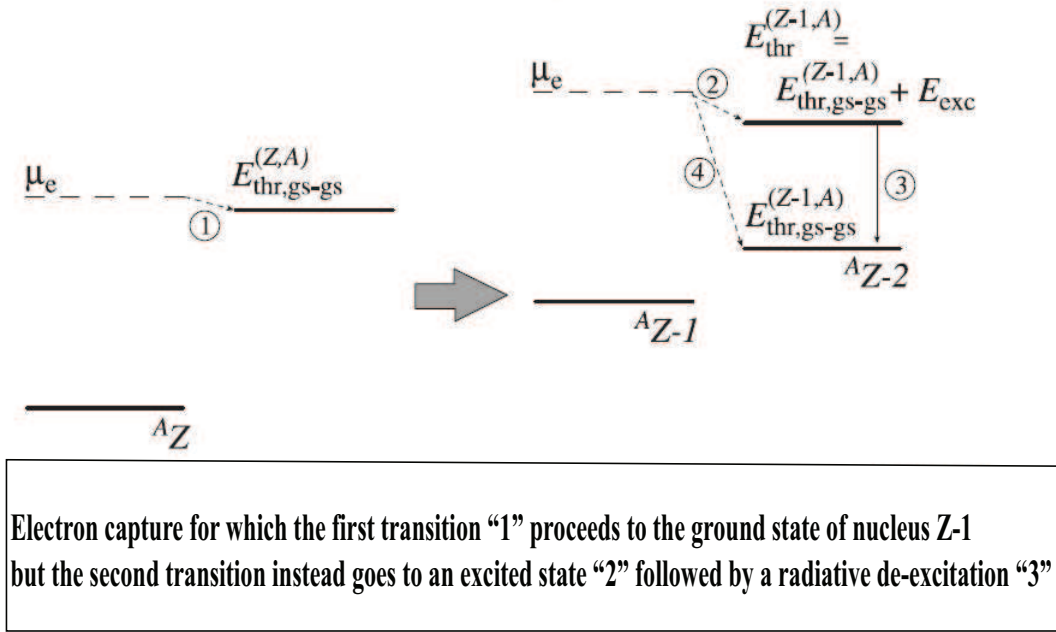
Figure 4.12: The level scheme of electron capture [19].

Another interesting difference between our model and Haensel & Zdunik [83] is the behavior of the electron Fermi energy. Figure 4.14 shows the electron Fermi energy versus column depth. Up to neutron drip around 1×10^{16} g cm $^{-2}$ electrons supply the pressure. Therefore the electron Fermi energy is simply determined by the pressure (with the mass density adjusting itself for compositional changes) and identical in both calculations. Beyond neutron drip Haensel & Zdunik [17] 's electron Fermi energy continues to increase, albeit at a decreasing rate, while in our model the electron Fermi energy remains more or less constant at a value of around 36.5 MeV. This is because the density is defined by the total pressure of the crust. The outer curst (lower density), is mainly supported by electron degeneracy pressure. But the inner crust, is mainly supported by neutron degeneracy pressure. In our model, the neutron pressure (as well as the neutron abundance) constrains the electron pressure in the inner crust. If the electron Fermi energy kept increasing beyond the electron capture threshold of ^{40}Mg (which has an electron capture threshold at around 37
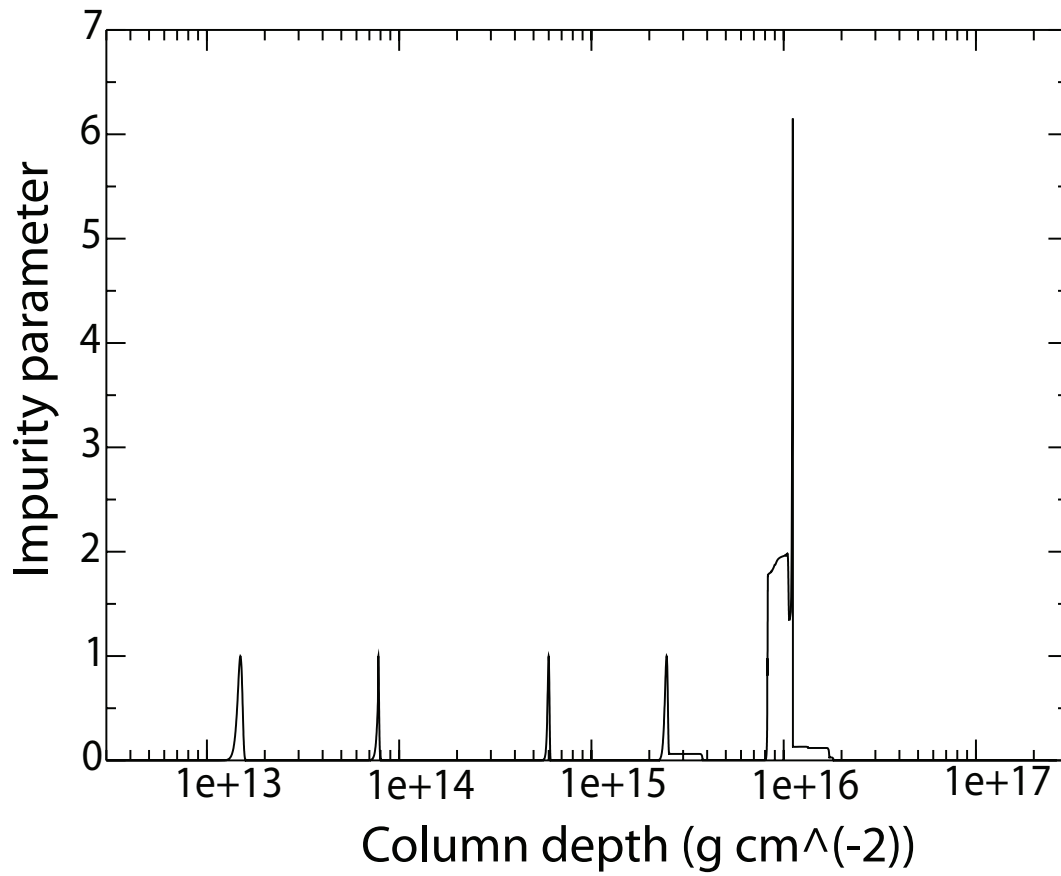
66

Figure 4.13: The impurity parameter versus column depth (g cm^{-2}) for an initial ^{56}Fe composition.
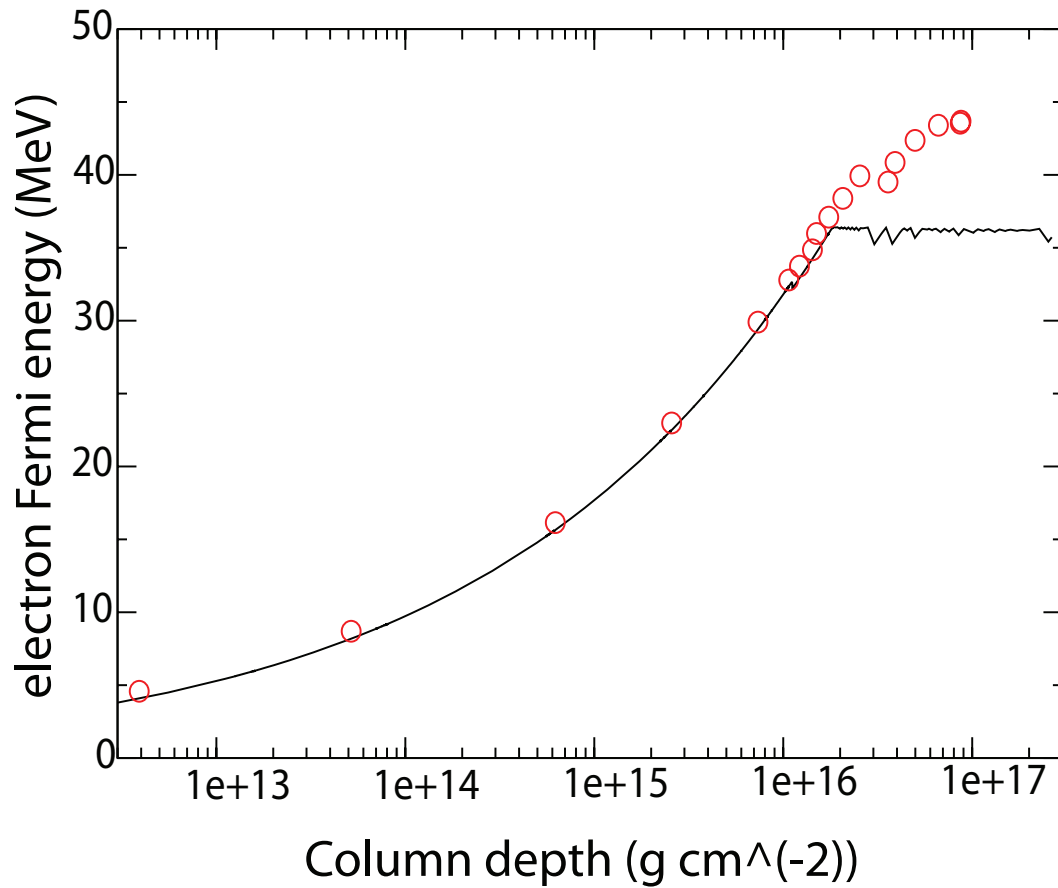
Figure 4.14: The electron Fermi energy versus column depth $(\mathrm{g\ cm^{-2}})$ for an initial composition of ^{56}Fe. The line shows the electron Fermi energy of our model while the red circles show the electron Fermi energy calculated by Haensel & Zdunik [83].

MeV), ^{40}Mg would further electron capture. The subsequent electron capture and neutron emissions would quickly proceed to carbon, which would then trigger a pycnonuclear fusion cycle with remaining ^{40}Mg nuclei ending in ^{40}Mg, effectively converting a ^{40}Mg nucleus into neutrons. This would lead to an increase in neutron abundance and a decrease in density and therefore electron Fermi energy turning electron capture on ^{40}Mg off again. The electron Fermi energy is therefore stablilized near the electron capture threshold of ^{40}Mg.

4.2 ^{56}Fe without pycnonuclear fusion

In order to study the effect of pycnonuclear fusion on the model, we ran a calculation with an initial composition of ^{56}Fe but turned off the pycnonuclear fusion rates. As expected, instead of getting stuck as ^{40}Mg the reaction flow proceeds all the way down to the lightest nuclei in the network.

Figure 4.15 shows the heat energy generation with and without pycnonuclear fusion versus column depth (g cm^{-2}). Clearly without pycnonculear fusion there is much less heating in the inner crust.

By comparing the heat energy generation with and without pycnonuclear fusion, we can see that the pycnonuclear fusion first sets in at around 8.0×10^{15} g cm^{-2} due to the fusion of light isotopes such as carbon, nitrogen oxygen and neon isotopes. After 2.0×10^{16} g cm^{-2} there is a significant amount of heat deposition due to the pycnonuclear fusion of ^{40}Mg with other light isotopes of carbon and nitrogen. We discussed the 3 main fusion cycles in the previous subsection and they are the main heat sources in that region.

Figure 4.16 shows the electron Fermi energy versus column depth (g cm^{-2}) for a calculation with and without pycnonuclear fusion. Without pycnonuclear fusion the stablilization
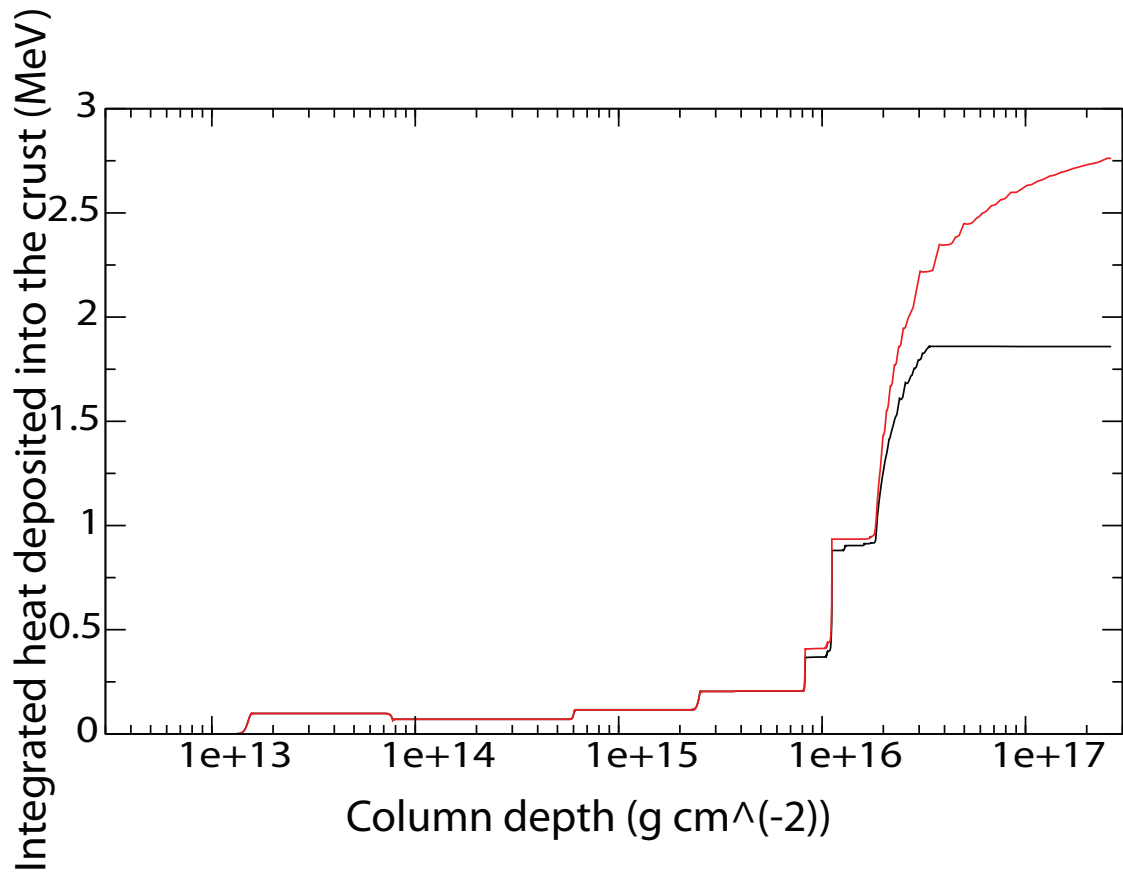
Figure 4.15: The integrated heat energy deposited into the crust with (red) and without (black) pycnonuclear fusion versus column depth (g cm^{-2}).
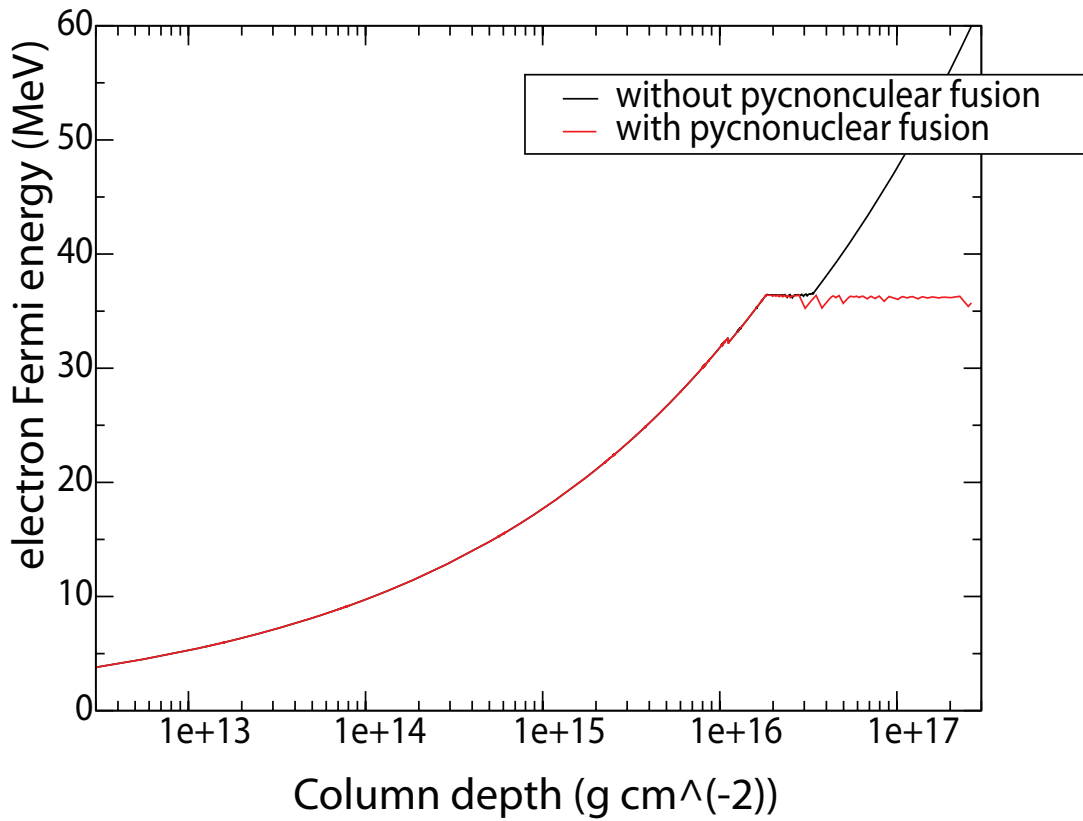
Figure 4.16: The electron Fermi energy with and without pycnonuclear fusion versus column depth $(g \, cm^{-2})$. The red line shows the calculation with pycnonuclear fusion while the black line shows the calculation without pycnonuclear fusion

mechanism described above is disabled. Rather, nuclei at the lower end of the network are essentially stable and can neither fuse or electron capture. Therefore, the electron abundances is fixed and the electron Fermi energy simply continues to increase with increasing density.

4.3   Other abundances

In order to investigate the dependence of the final abundance on initial composition, the model was run for a number of single species initial compositions. In each case, the initial mass fraction of the initial species chosen is 1. The simulation conditions are the same as for the ^{56}Fe case. Figures 4.17, 4.18 and 4.19 shows $< Z >, < N >$ and $< A >$ versus column depth for calculations with ^{38}Ar,^{42}Si, ^{41}K, ^{47}Sc, ^{46}Ti, ^{50}Cr, ^{61}Ni ,^{70}Ge as initial abundance.

As for an initial composition of ^{56}Fe, initially during the electron capture phase $< A >$ remains constant while $< Z >$ decreases and $< N >$ increases stepwise. Overall the behavior for different initial isotopes is qualitatively similar with transitions simply occurring at different locations owing to different electron capture thresholds. Neutron drip occurs at around column depth 1.0×10^{16} g cm^{-2} with only a very small dependence on the initial composition. And independent of the initial nucleus the composition is quickly converted into ^{40}Mg. Therefore regardless of initial composition, beyond a column depth 2.0×10^{16} the crust is composed of ^{40}Mg.

^{38}Ar behaves differently as it reaches neutron drip at a lower Z (oxygen and neon isotopes) than ^{40}Mg. Oxygen and Neon isotopes fuse to form heavier isotopes and they electron capture and neutron emission down to ^{40}Mg. Figure 4.20 shows the time integrated reaction flows for an initial composition of ^{38}Ar. As we can see from the graph, oxygen and neon isotopes fuse to form heavier isotopes.

Figure 4.17: $< Z >$ versus column depth (g cm^{-2}) for an initial abundance ^{38}Ar, ^{42}Si, ^{41}K, ^{47}Sc, ^{46}Ti, ^{50}Cr, ^{61}Ni and ^{70}Ge
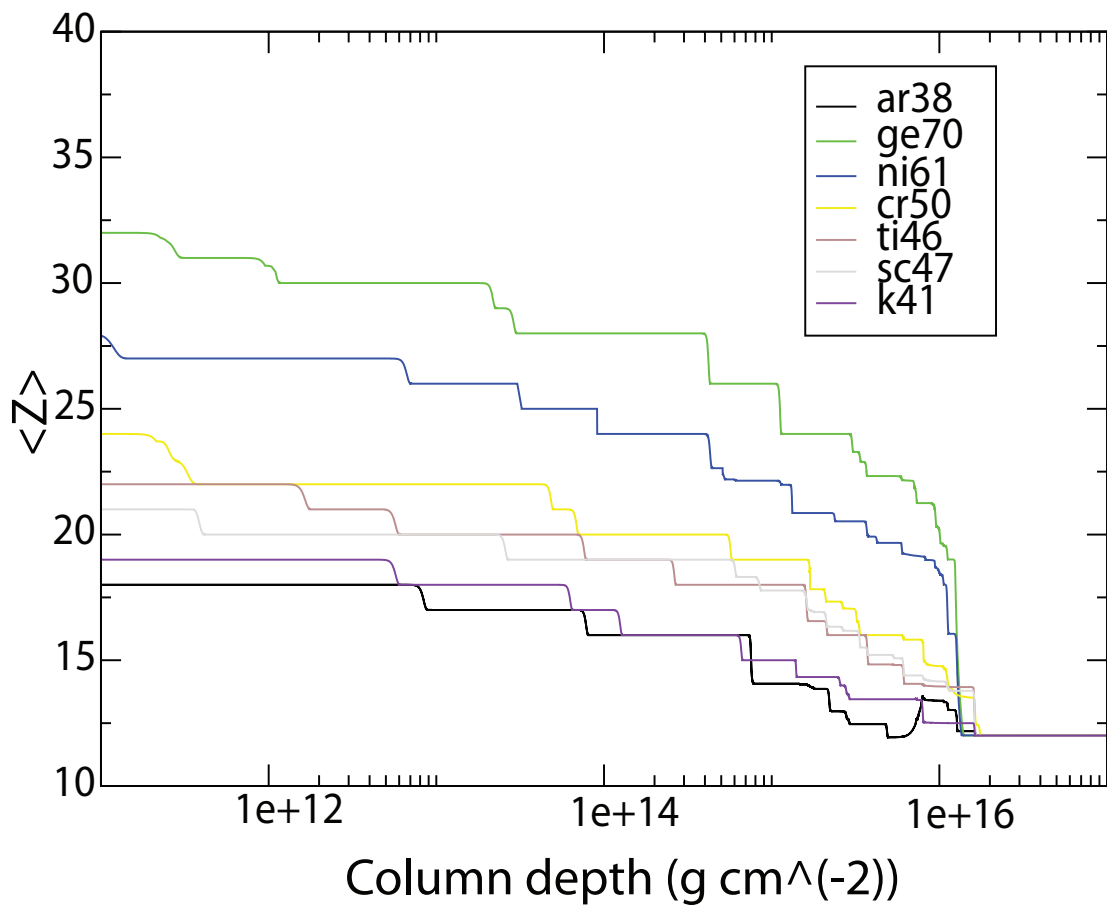
Figure 4.18: $< N >$ versus column depth (g cm^{-2}) for and initial abundance ^{38}Ar, ^{42}Si, ^{41}K, ^{47}Sc, ^{46}Ti, ^{50}Cr, ^{61}Ni and ^{70}Ge

Figure 4.19: $< A >$ versus column depth (g cm^{-2}) for and initial abundance ^{38}Ar, ^{42}Si, ^{41}K, ^{47}Sc, ^{46}Ti, ^{50}Cr, ^{61}Ni and ^{70}Ge
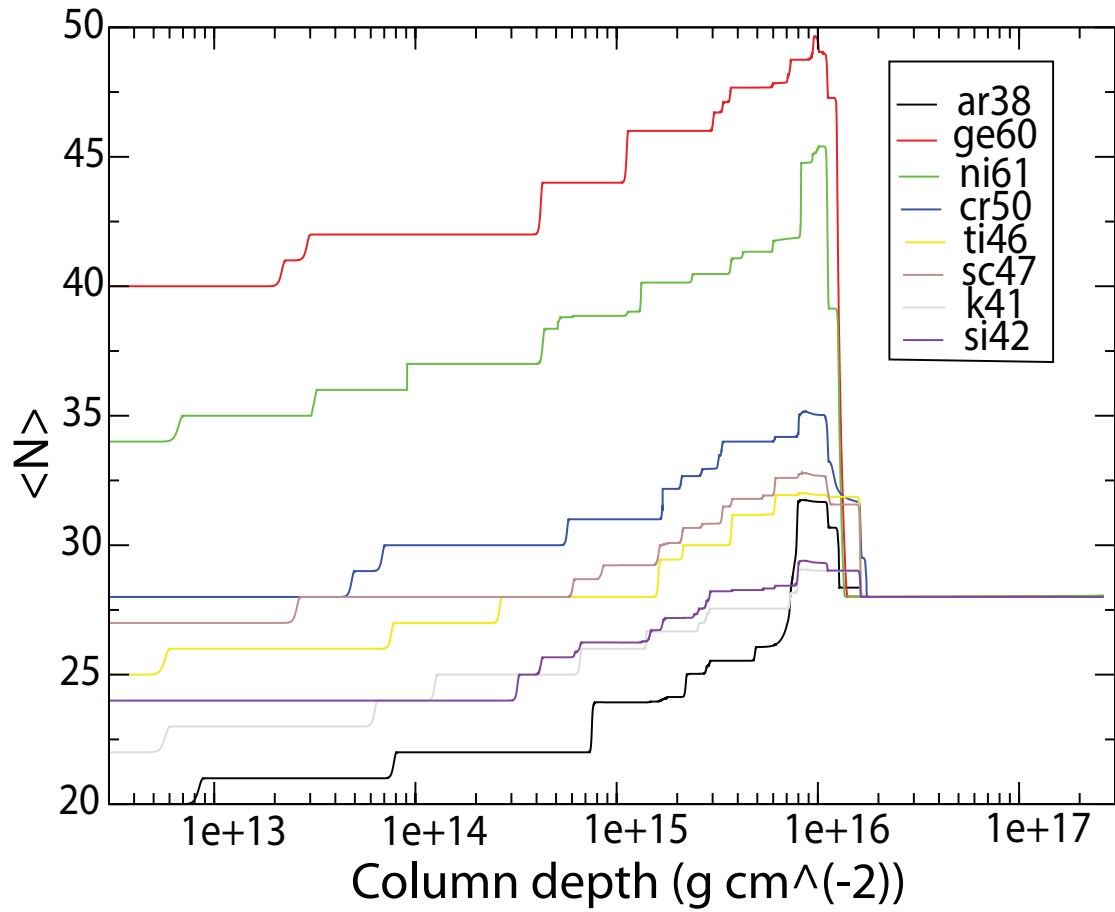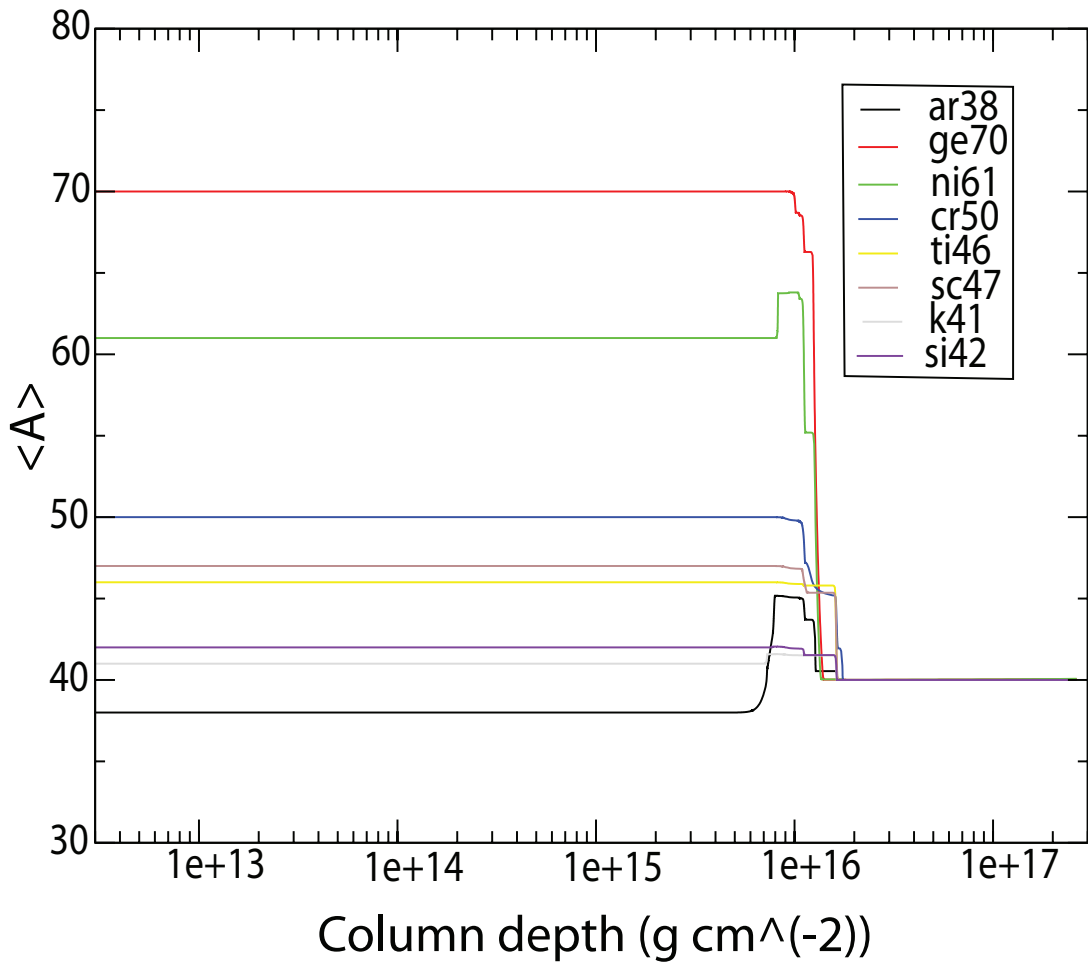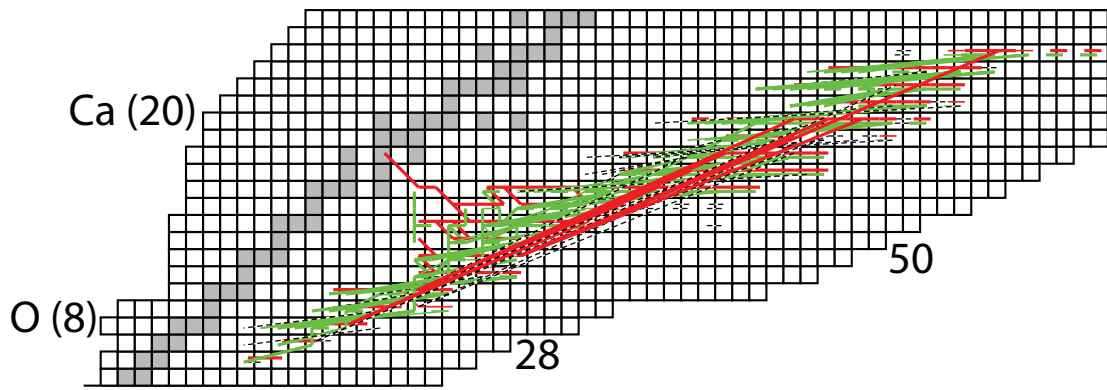
Figure 4.20: Reaction flows for an initial composition of ^{38}Ar (see Fig. 4.1 and 4.2 for details). Here unbound nuclei are not distingusihed from bound nuclei .

4.4 Superburst ashes

After studying the reaction path of individual initial nuclides, we now go to a more realistic composition, the superburst ashes. This would reflect a system where all the accreted matter is processed by superbursts. The superburst ashes from [84] are used. It is dominated by ^{66}Ni with a mass fraction of 0.348, ^{64}Ni with a mass fraction of 0.151, ^{60}Fe with a mass fraction of 0.140, and ^{54}Cr with a mass fraction of 0.058. The evolution starts at time 1.0×10^8 s, temperature 0.48 GK, density 1.20×10^9 g cm^{-3}, and electron Fermi energy 3.66 MeV. The evolution ends at time 1.0×10^{13} s, with temperature 0.46 GK, and electron Fermi energy 35.45 MeV. Figure 4.21 shows the initial composition and Fig 4.22 shows the final composition at the end of the calculation. As expected from the results discussed in 4.3, the initially diverse ashes are again converted to ^{40}Mg at the end of the evolution.

At the beginning of the evolution, some nuclei do β decay back to more proton-rich nuclei because of a mismatch of initial electron Fermi energy in our calculation, and the electron Fermi energy corresponding to the initial composition. However, the composition quickly settles into the correct equilibrium composition for the initial depth. The nuclei then undergo electron capture and in some cases the inverse β^- decay can also occur (green lines for some

Time: 1.000e+08 s
Temp: 0.48 GK
Density: 1.20e+09 g/cm^3
n-Abundan: 2.82e-11
EF_e: 3.66 MeV
EF_n: 0.00 MeV
Max Flow: 0.00e+00
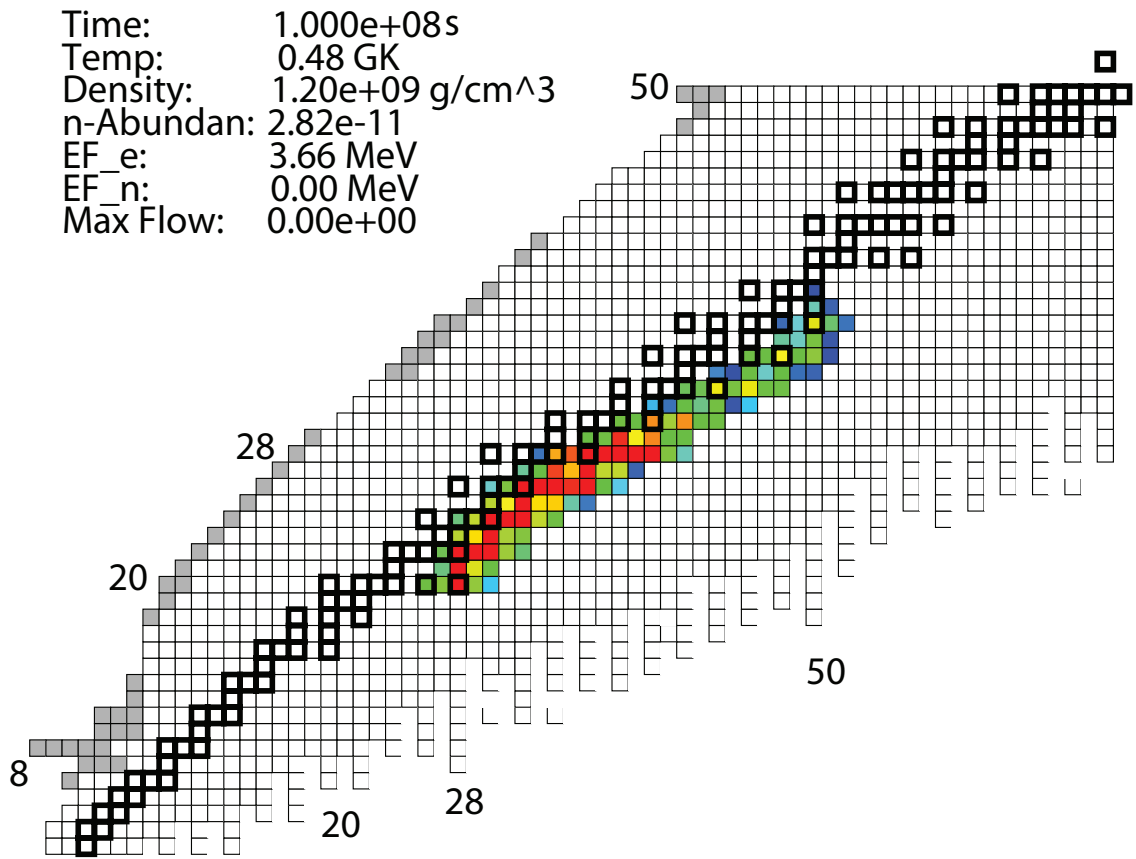
Figure 4.21: The initial composition of the calculation with superburst ashes

Time: 2.992e+12s
Temp: 0.48 GK
Density: 1.10e+13 g/cm^3
n-Abundan: 8.90e-01
EF_e: 36.24 MeV
EF_n: 3.71 MeV
Max Flow: 1.20e-04

Figure 4.22: Composition at the end of the calculation with initial superburst ashes(see Fig. 4.1 and 4.2 for details)

nuclei in Fig 4.23). This leads to a cycling behavior. The associated neutrino emission leads to cooling. Beyond an electron Fermi energy of 12 MeV, neutron emission leads to an increase in neutron abundance. The neutrons emitted are absorbed by nuclei (especially even Z nuclei). The nuclei continue to be transformed into more neutron rich species by electron capture and neutron capture while the neutron abundance keeps increasing.

At time 2.964×10^{11} s, density 6.56×10^{11} g cm^{-3}, neutron abundance 4.94×10^{-10}, and electron Fermi energy around 29.92 MeV, a super electron capture cascade as described in Gupta et al [19] occurs. As a consequence high Z nuclei are converted into low Z nuclei and a large number of neutrons a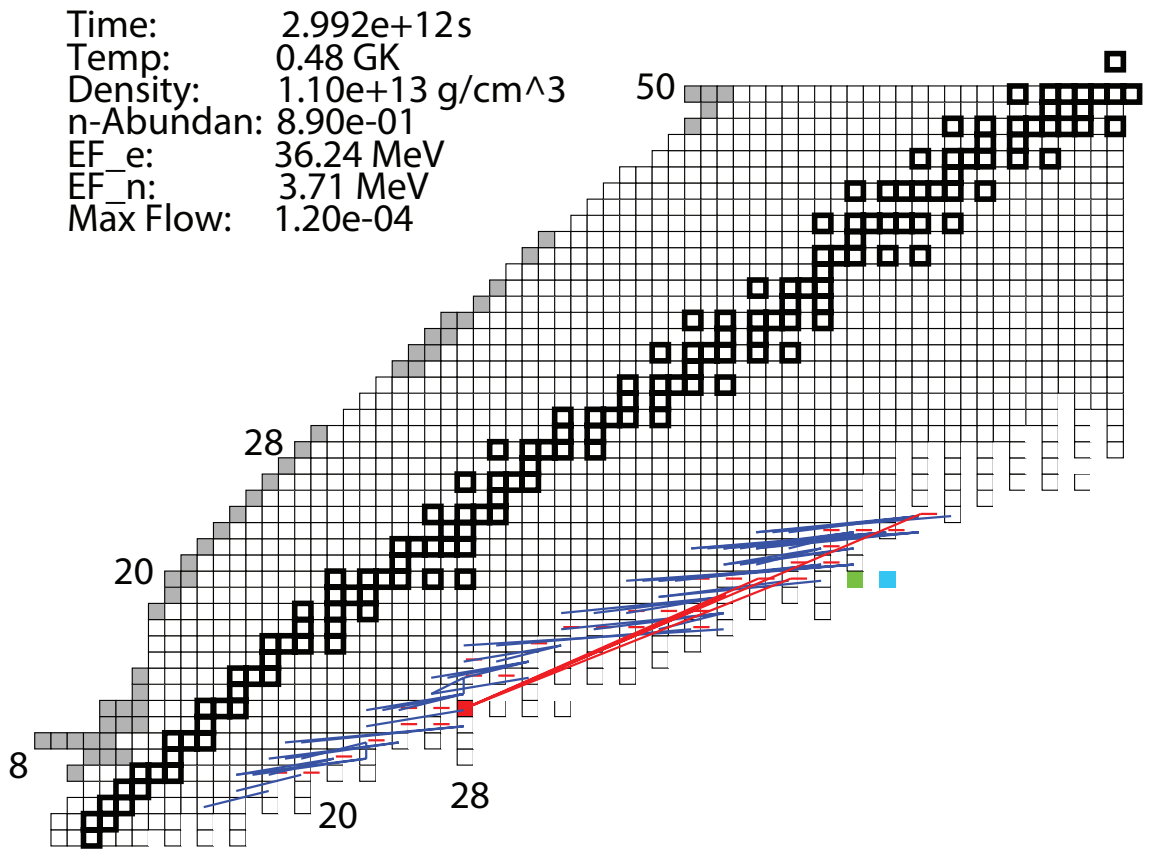re emitted within a small range of electron Fermi energy. The situation is similar to the case of initial ^{56}Fe composition. One difference are the higher abundances of ^{32}Ne, ^{42}Si and ^{70}Ca due to the different initial abundances in the calculation with superburst ashes. Because of the higher abundance of ^{32}Ne, the dominant initial fusion is ^{32}Ne fuses with ^{32}Ne to form ^{64}Ca and ^{23}N fuses with ^{23}N forming ^{46}Si as well as the fusion of ^{23}N with ^{32}Ne to form ^{55}Cl. These first fusion reactions are different from the case with an initial ^{56}Fe composition. Figure 4.23 shows the first fusion of the superburst ashes.

At time 3.957×10^{11} s, density 8.85×10^{11} g cm^{-3}, neutron abundance 4.84×10^{-3}, and electron Fermi energy around 32.16 MeV, the dominant nuclei are ^{70}Ca, ^{62}Ar, ^{61}Cl, ^{46}Si and ^{40}Mg. The difference from the ^{56}Fe case is the appearance of significant amounts of ^{70}Ca which is produced partly by electron capture and neutron emission from heavier isotopes and partly by the fusion of neon isotopes as discussed above.

At time 5.153×10^{11} s, density 1.56×10^{12} g cm^{-3}, neutron abundance 3.78×10^{-1}, and electron Fermi energy around 34.00 MeV, ^{62}Ar and ^{61}Cl electron capture and neutron emission partly to ^{46}Si and partly to ^{40}Mg similar to the ^{56}Fe calculation.

Time: 2.964e+11 s
Temp: 0.50 GK
Density: 6.56e+11 g/cm^3
n-Abundan: 4.94e-10
EF_e: 29.89 MeV
EF_n: 0.00 MeV
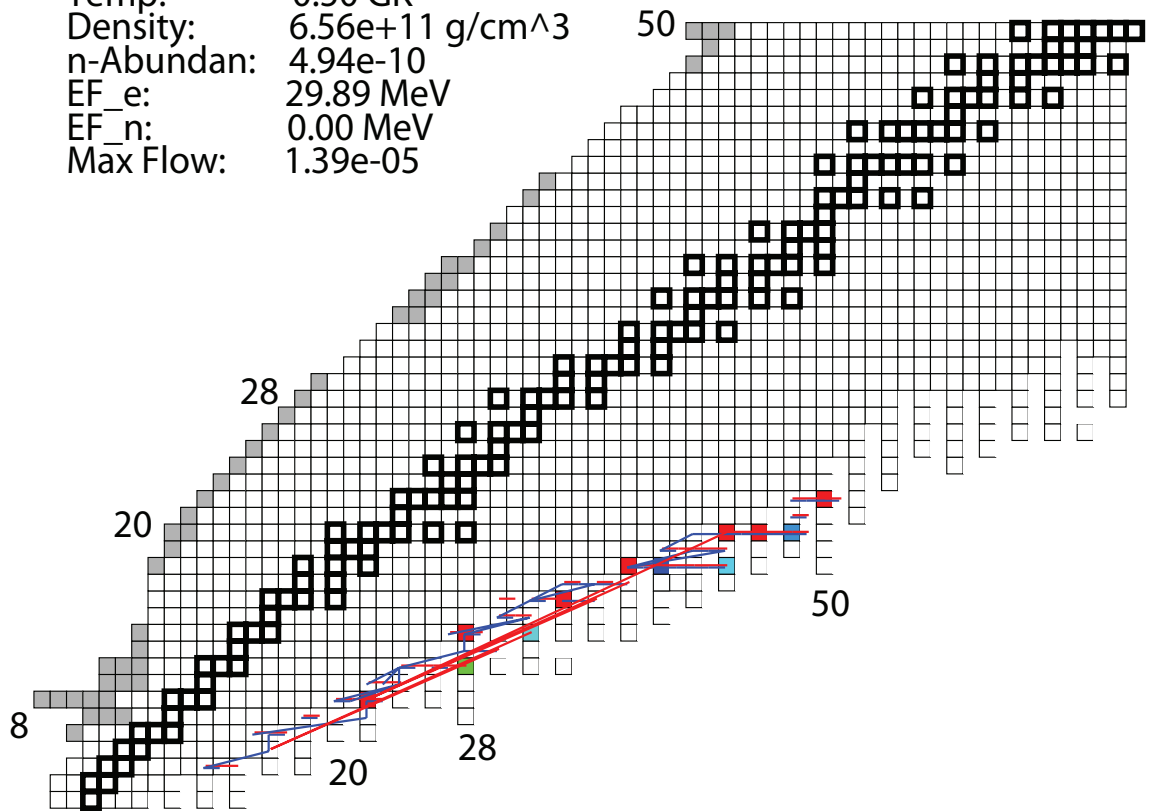Max Flow: 1.39e-05

50

28

20

8
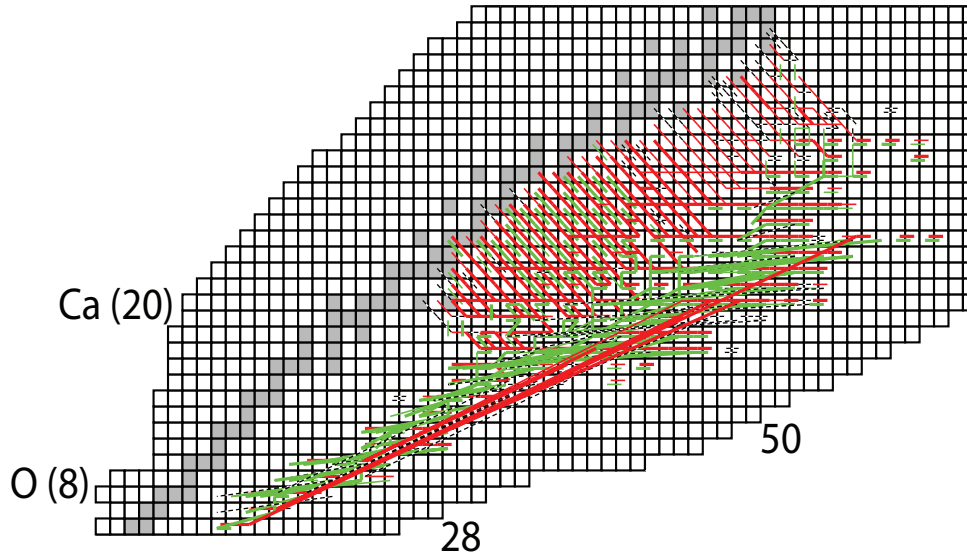
20

28

50

Figure 4.23: The first fusion of the superburst ashes

Figure 4.24: Time integrated reaction flows for an initial composition of superburst ashes

At time 6.689×10^{11} s, density 1.90×10^{12} g cm^{-3}, neutron abundance 3.83×10^{-1}, and electron Fermi energy around 35.95 MeV, all isotopes convert to ^{40}Mg. Beyond this point, the three most dominant fusion cycles are the same as in the ^{56}Fe calculation. Figure 4.24 shows the reaction flows.

Figure 4.25 shows the abundances of ^{72}Ti, ^{62}Ar, ^{70}Ca, ^{46}Si, and ^{40}Mg versus time. ^{40}Mg starts building up at 3.0×10^{11} g cm^{-2} and starts decaying due to the fusion of ^{40}Mg at 1.0×10^{12} g cm^{-2}. The decay of ^{40}Mg occurs somewhat later than in the ^{56}Fe case.

Figure 4.26 shows $< Z >, < N >, < A >$ versus column depth (g cm^{-2}). At the beginning, $< N >$ increases and $< Z >$ decreases while $< A >$ remains the same. Then at a column density of around 8.0×10^{15} g cm^{-2}, $< Z >$ decreases while $< N >$ and $< A >$ increase because of neutron capture. At around 1.0×10^{16} g cm^{-2}, $< Z >$ and $< N >$ and thus $< A >$ decrease because the super electron capture cascade. Beyond a column depth of 1.0×10^{16} g cm^{-2} the composition besides of neutrons is dominated by ^{40}Mg. An interesting point is that the final abundance is the same as the ^{56}Fe case, this implies that the final
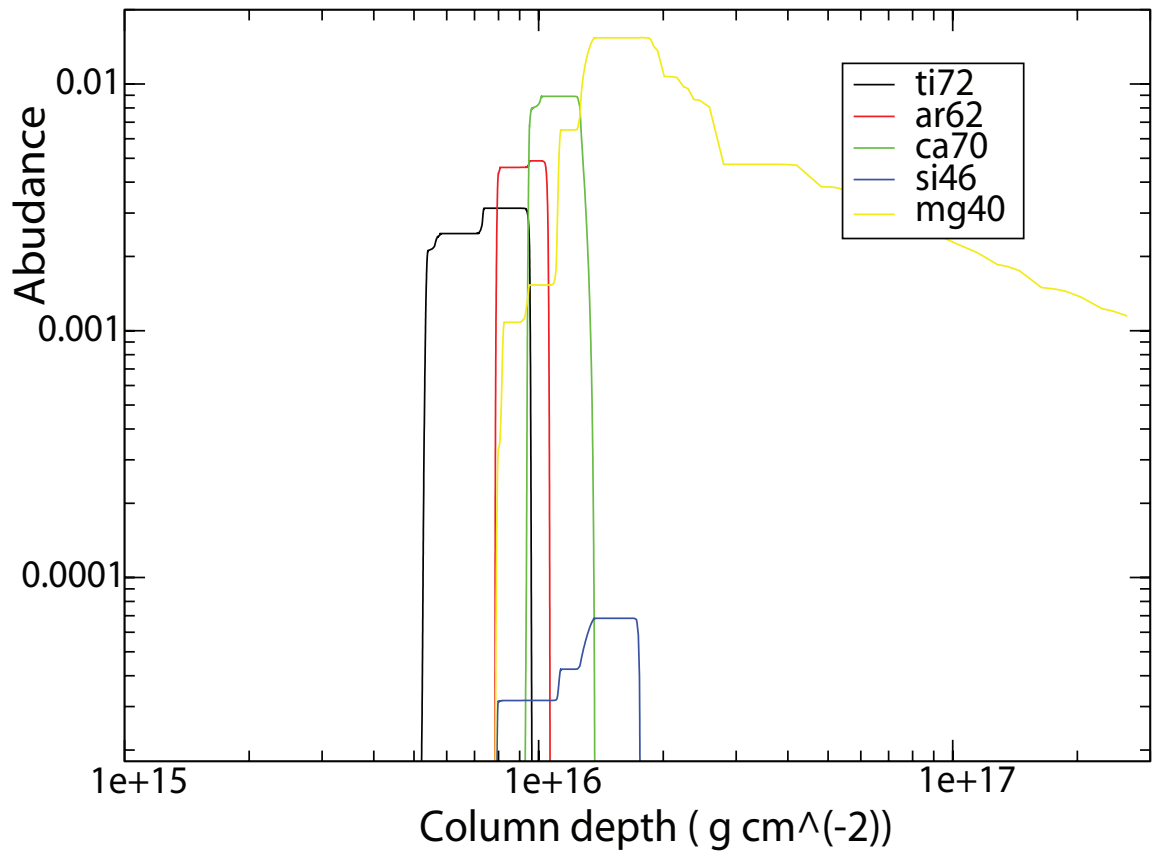
Figure 4.25: The abundance of ^{72}Ti, ^{62}Ar, ^{70}Ca, ^{46}Si, ^{40}Mg versus column depth.
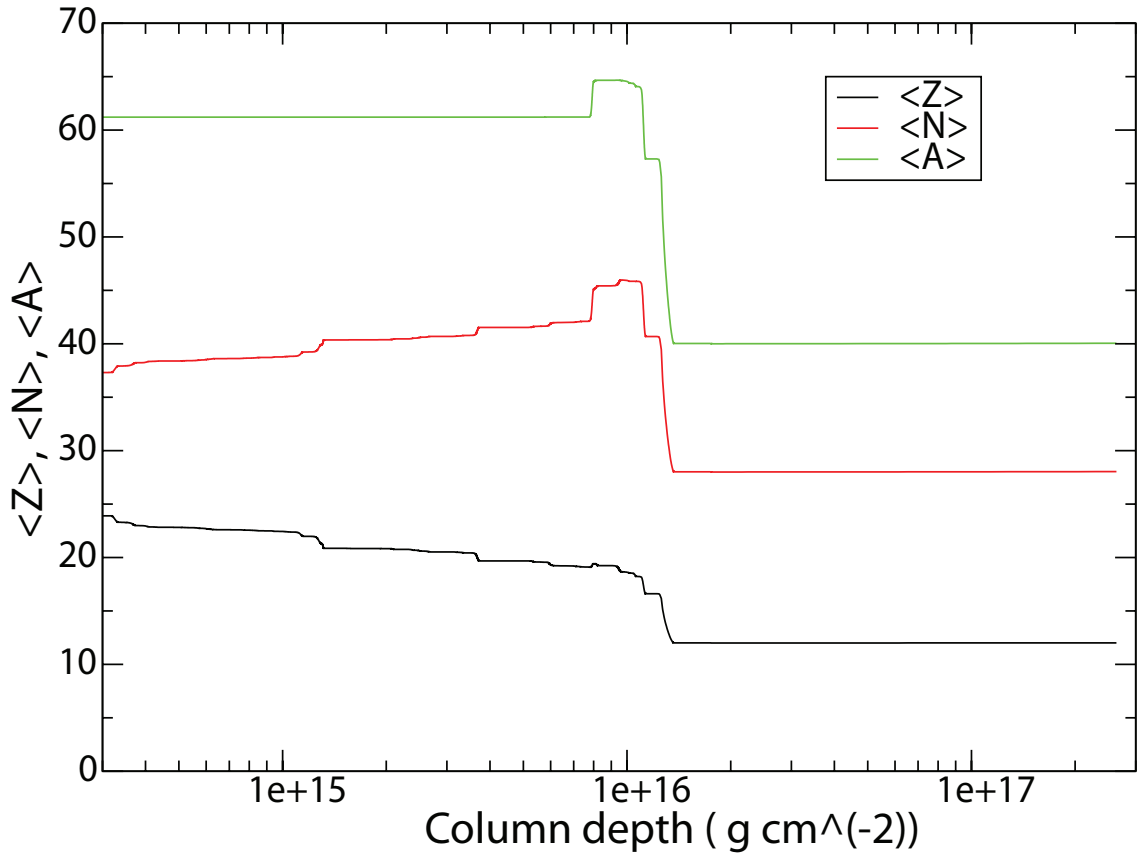
Figure 4.26: $< Z >, < N >, < A >$ versus column depth.

composition does not depend on the initial abundance.

Figure 4.27 shows the integrated energy deposited into the crust as a function of column depth. At the beginning, the energy is negative is due to the cooling via the β decay/electron capture cycles. At column depth 5.0×10^{14} g cm $^{-2}$, heat generated by the electron captures leads to an increase of the integrated energy deposition. After 1.0×10^{16} g cm^{-2}, there is a jump in the energy deposition due to the onset of the super electron capture cascade. The pycnonuclear fusion reactions further increase the heat energy deposition beyond that depth.

Figure 4.28 shows the impurity parameter as a function of column depth. After some initial fluctuations the main effect is a drastic decrease in impurity around a column depth
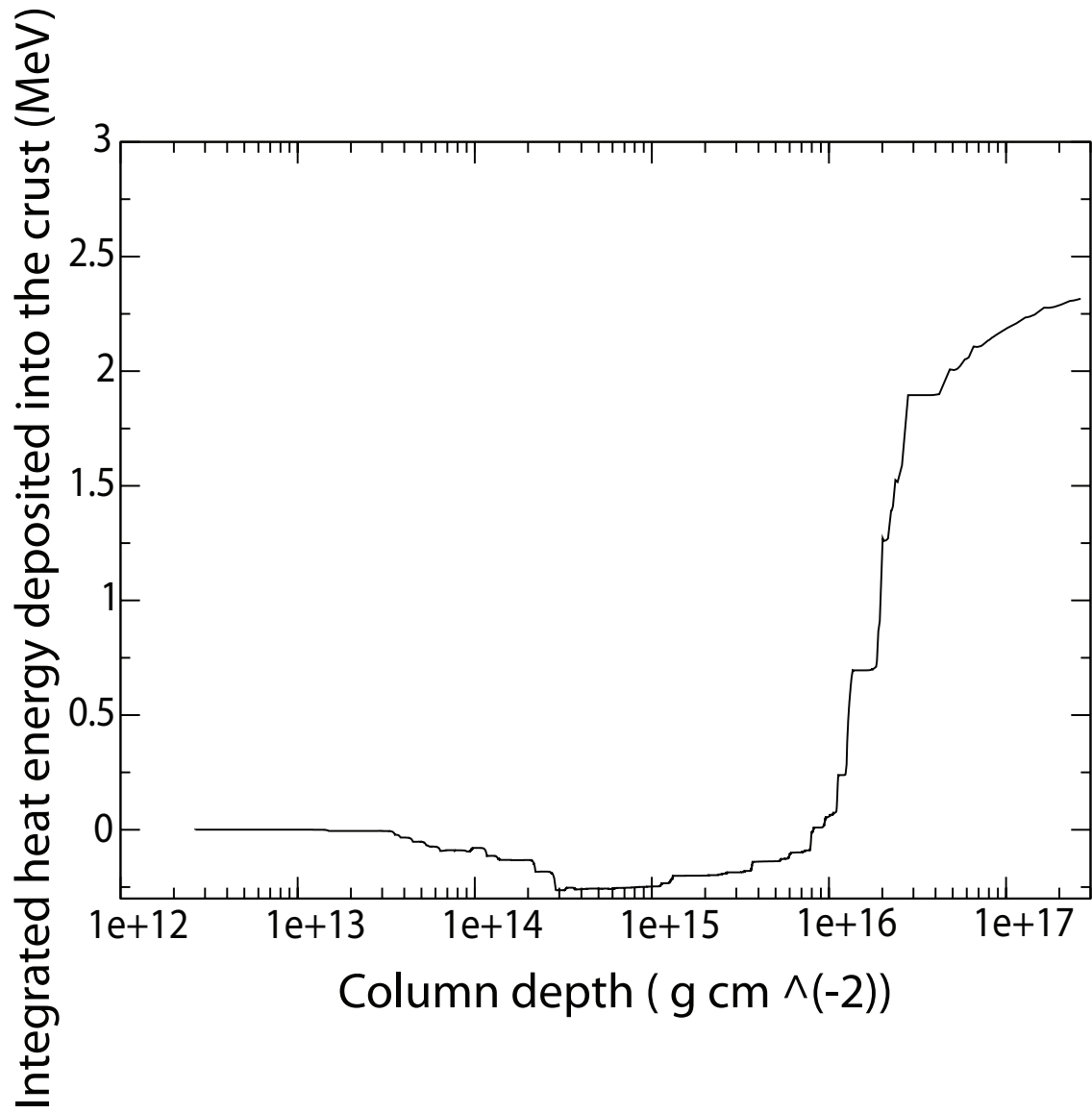
Figure 4.27: The integrated energy deposition versus column depth for initial superburst ashes

of 1.0×10^{16} g cm^{-2}. This implies that the ashes transition from a diverse distribution to a more uniform distribution. At the end of the evolution, the impurity parameter drops much below 1 implying that the crust is very pure. The small increase in the impurity parameter is because the ^{40}Mg keeps decreasing and converts to neutrons while the other abundances (which are small) remain more or less constant.
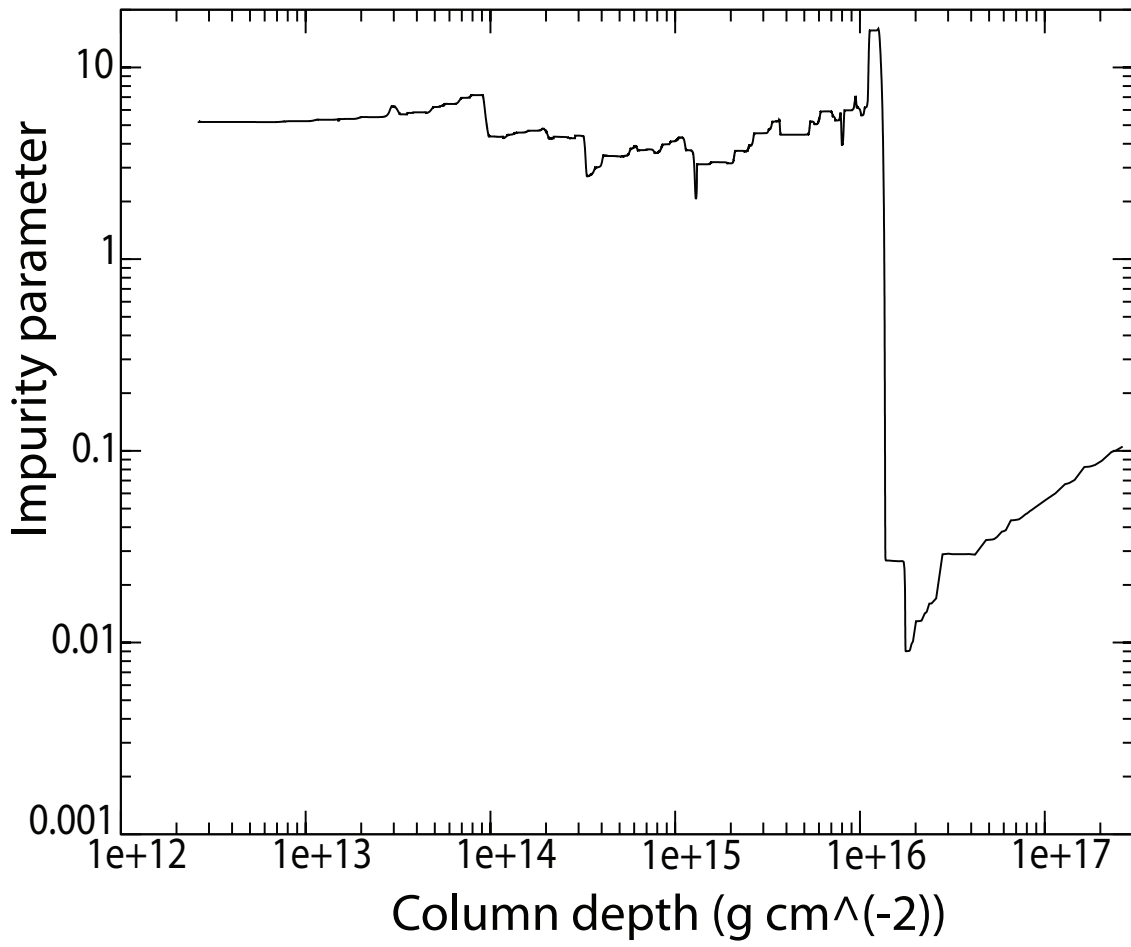
Figure 4.28: Impurity parameter versus column depth.

Chapter 5

Astrophysical applications

The composition and heat generation of the crust of accreting neutron stars affect various crust properties which are linked to observables. In this section, we use the results to briefly discuss on the electrical and thermal conductivities, ionic coupling parameter, ionic and electronic plasma frequency, plasma temperature, shear modulus and viscosity.

5.1 Ionic and electronic plasma frequency and temperature

Plasma properties affect the charge screening properties of nuclear reactions and the transmission of electromagnetic fields. In this context plasma frequency and plasma temperature are two important parameters. The plasma frequency is defined as a resonant frequency where the whole plasma behaves collectively as an oscillating system. For a solid state the plasma frequency is an isotropic measure of the refractive index for transmission and reflection of radiation inside the plasma. The plasma in the magnetosphere of the neutron

stars can produce coherent radio emissions which are pulsars. In our calculation of the pycnonuclear reaction rates, we use the plasma frequency to take into account its effects on the pycnonuclear reaction rates. The ion plasma frequency for a one component plasma is defined as [10]

$$\omega_{\text{pi}} = (\frac{4\pi e^2 n_N Z^2}{A m_u})^{1/2} \tag{5.1}$$

where e is the electron charge, n_N is the number density of ions, Z is the proton number of the nuclei, A is the mass number of nuclei, and m_u is the atomic mass unit. The plasma temperature T_{pi} is defined as

$$T_{\text{pi}} = \hbar\omega_{pi}/k_{\text{B}} \tag{5.2}$$

For multiple species of nuclei, the ion plasma frequency is defined as [74]

$$\omega_{\text{pi}}^2 = \sum_j \frac{4\pi Z_j^2 e^2 n_j}{A_j m_u} \tag{5.3}$$

If the electrons are cold, (the electron thermal speed is negligible), the electron plasma frequency is defined as [10]

$$\omega_{\text{pe}} = (\frac{4\pi e^2 n_{\text{e}}}{m_{\text{e}}^*})^{1/2} \tag{5.4}$$

where n_e is the electron density, $m_{\text{e}}^* = m_{\text{e}}(1 + x_r^2)^{1/2}$ and $x_r = p_{\text{Fe}}/(m_{\text{e}}c)$ and $p_{\text{Fe}} = \hbar(3\pi^2 n_{\text{e}})^{1/3}$

Figure 5.1 shows the ion plasma temperature (K) versus column depth (g cm^{-2}) for an initial composition of ^{56}Fe compared to previous work. The ion plasma temperature for our model with initial superburst ashes is also shown. We can see that the plasma temperature in general increases with the density. This is expected as the ions density increases with mass

density. The three cases are very close to each other in the outer crust. Beyond a column depth $\sim 10^{16}$ g cm^{-2}, the plasma temperature increases much less for all three cases. This is because neutrons drip out from the nuclei decreasing the density of ions. There are some smaller discrepancies in the inner crust between our model and previous work because the final abundance and therefore Z^2/A are different. In addition, the electron density in our model tends to remain constant in the inner crust while Haensel and Zdunik [17] predict a continued increase (see Fig. 4.14) leading to different slopes in the plasma frequency.

Figure 5.2 shows the electron plasma temperature in log10 (K) versus column depth in log10 (g cm^{-2}) for ^{56}Fe compared to previous work. The ion plasma temperature for our model with initial superburst ashes is also shown. The electron plasma temperature shows similar behavior as the ion plasma temperature.

5.2 Coulomb coupling parameter and crust melting

Using the composition predicted by Haensel and Zdunik, it has been shown that for neutron star crusts with low thermal conductivity where electron-ion scattering dominates, alternating layers of liquid and solid material can form [59]. Following Farouki & Hamaguchi [61], the crust is liquid when the ionic coupling parameter $\Gamma \sim< 170$, otherwise, the crust forms a crystallized solid. Electron capture reactions lower the Z values which leads to a decrease in Γ below 173. Pycnonuclear fusions of identical species in the model of Haensel and Zdunik double the Z values and increase the Γ value above 173. That is why the crust forms alternating layers. The strain in the crust disappears in the melted layers because the liquid does not have shear stress. This limits the mass quadrupole of the neutron star induced by thermal perturbations to the electron capture rate (Bildsten 1998) [11].

Figure 5.1: The plasma temperature in log10 (K) versus column depth in log10 (g cm^{-2}) from this work for an initial composition of ^{56}Fe (black) and superburst ashes (red) as well as from Haensel and Zdunik (green)
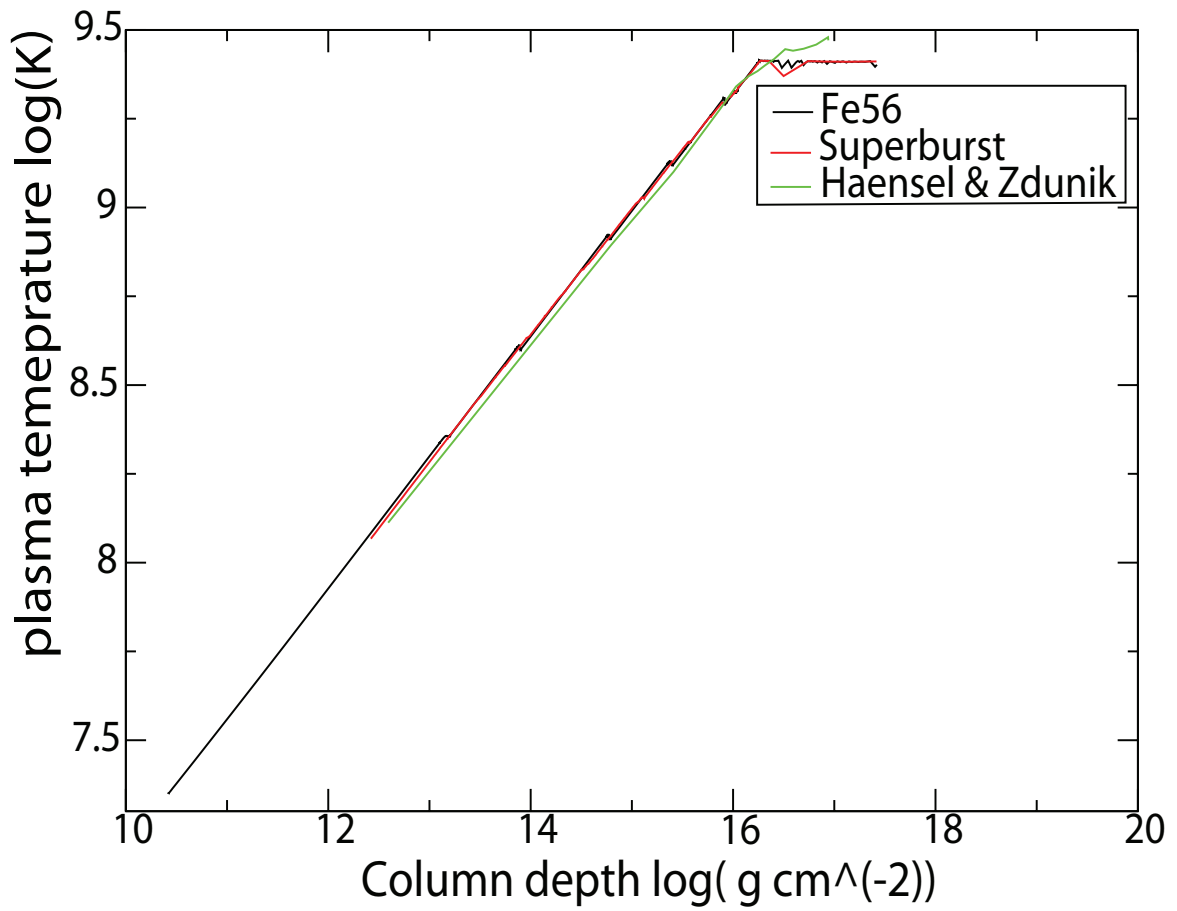
Figure 5.2: The electron temperature log10(K) versus column depth in log10 (g cm^{-2}) from this work for an initial composition of ^{56}Fe (black) and superburst ashes (read) as well as from Haensel and Zdunik (green)
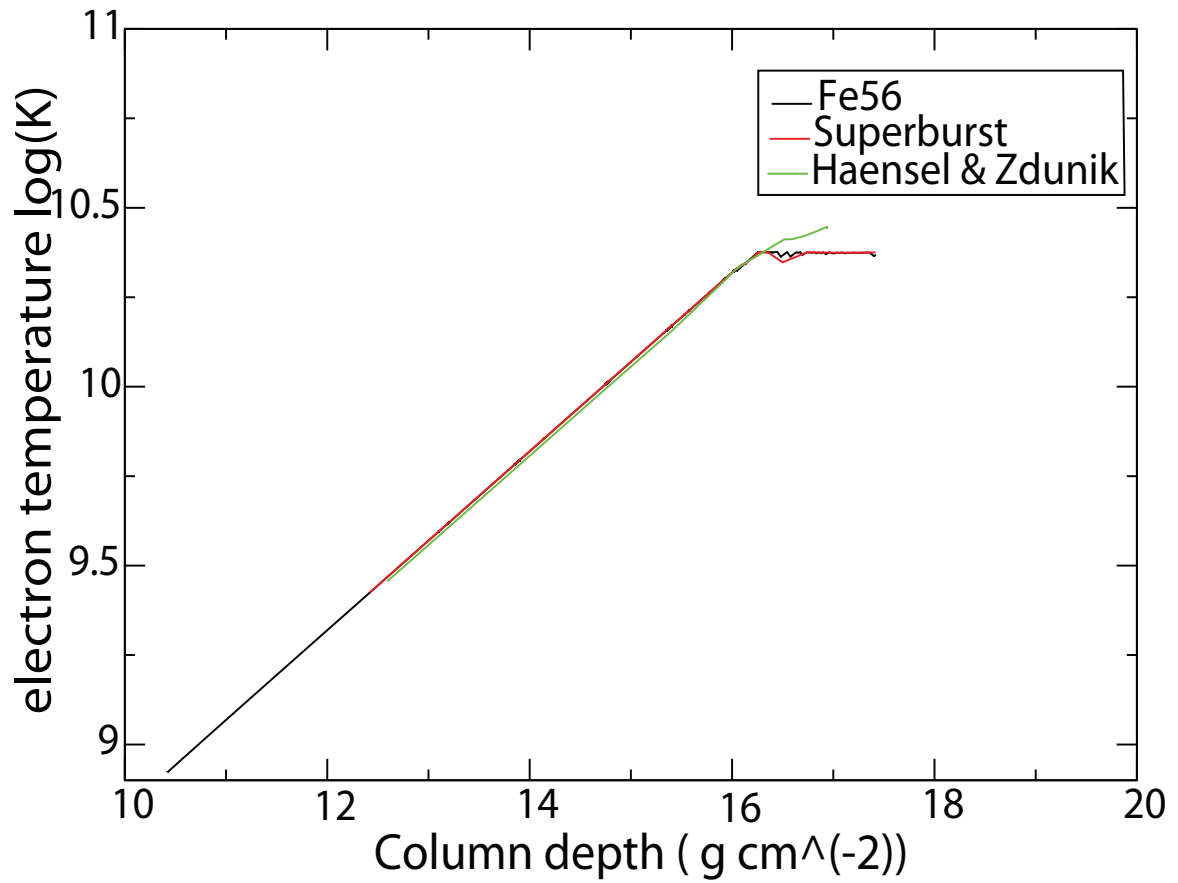
The ionic coupling parameter for a crust composed of a single species of nuclei is defined as:

$$\Gamma = \frac{Z^2 e^2}{k_{\mathrm{B}} T} \left(\frac{4\pi}{3} n_N\right)^{1/3};$$ (5.5)

where Z is the charge number, e is the electron charge, k_B is the Boltzmann constant, T is the temperature, and n_N is the number density of nuclei. The exact value of Γ for the transition from solid to liquid is not known, but it is predicted to be approximately ~ 173.

For a multicomponent plasma, the ionic coupling parameter can be defined as [74]:

$$\Gamma = \sum_j \Gamma_j = \sum_j \frac{Z_j^2 e^2}{k_{\mathrm{B}} T} \left(\frac{4\pi}{3} n_N\right)^{1/3} = \sum_j \frac{Z_j^{5/3} e^2}{k_{\mathrm{B}} T} \left(\frac{4\pi}{3} n_{\mathrm{e}}\right)^{1/3}$$ (5.6)

Figure 5.3 shows Γ versus pressure for an initial composition of ^{56}Fe. Γ increases with the mass density as the electron density increases until a pressure of around 10^{30} dyn cm^{-2} at which point the super electron capture cascade leads to a significant decrease in electron density and Z value. After this sharp drop, differences from the composition of Haensel & Zdunik appear. The main difference is that Γ remains fairly constant in the pycnonculear regime because the abundance is locked in ^{40}Mg due to shell effects, and because the super electron cascade effect leads to rapid cycling of material back to ^{40}Mg once a fusion reaction has occurred. Therefore there is no temporary high Z phase following a fusion as in Haensel & Zdunik and consequently Γ stays low.

However, Γ does not go as low as in Brown [59] because shell effects favour ^{40}Mg as opposed to lighter nuclei. Therefore, when taking $\Gamma = 173$ as transition the crust in my model is solid beyond a pressure of $\sim 10^{28.5}$ dyn cm^{-2}.

The predicted values of Γ vary only slightly between 183 and 216 in the inner crust,

rather close to 173. Given the uncertainty in where exactly the liquid to solid transition takes place, there could still be liquid to solid transitions.

5.3   Shear modulus

The shear modulus of the neutron star crust can affect crust oscillations [86]. Specific frequencies are observed for these oscillations. The shear modulus is also an important parameter for the calculation of star quakes [87]. Magnetic mountains are irregularities on the neutron star surface [87]. They have been proposed to be created by matter that is accreted onto the star and is channeled to the poles by a strong magnetic field. It has been suggested that if the field is strong enough it can maintain a moutain at the poles that is not flattened by the strong gravitational force. The typical height of magnetic moutians is a few meters. Magnetic mountains on rapidly rotatiY neutron stars emit gravitational waves because of their large masses and high accelerations and the height of the mountains depends on breaking strain of the neutron star crust [87]. An effective shear modulus μ assuming a body-centered cubic polycrystal is calculated by Ogata & luchimaru [88]. They performed directional averages over rotations of the Cartesian axes. At T=0, they obtain:

$$\mu = \frac{1}{5}(2b_{11} + 3c_{44}) \tag{5.7}$$

where

$$b_{11} = 0.0245 n_N (Ze^2)(\frac{4\pi}{3}n_N)^{1/3} \tag{5.8}$$

$$c_{44} = 0.1827 n_N (Ze^2)(\frac{4\pi}{3}n_N)^{1/3} \tag{5.9}$$
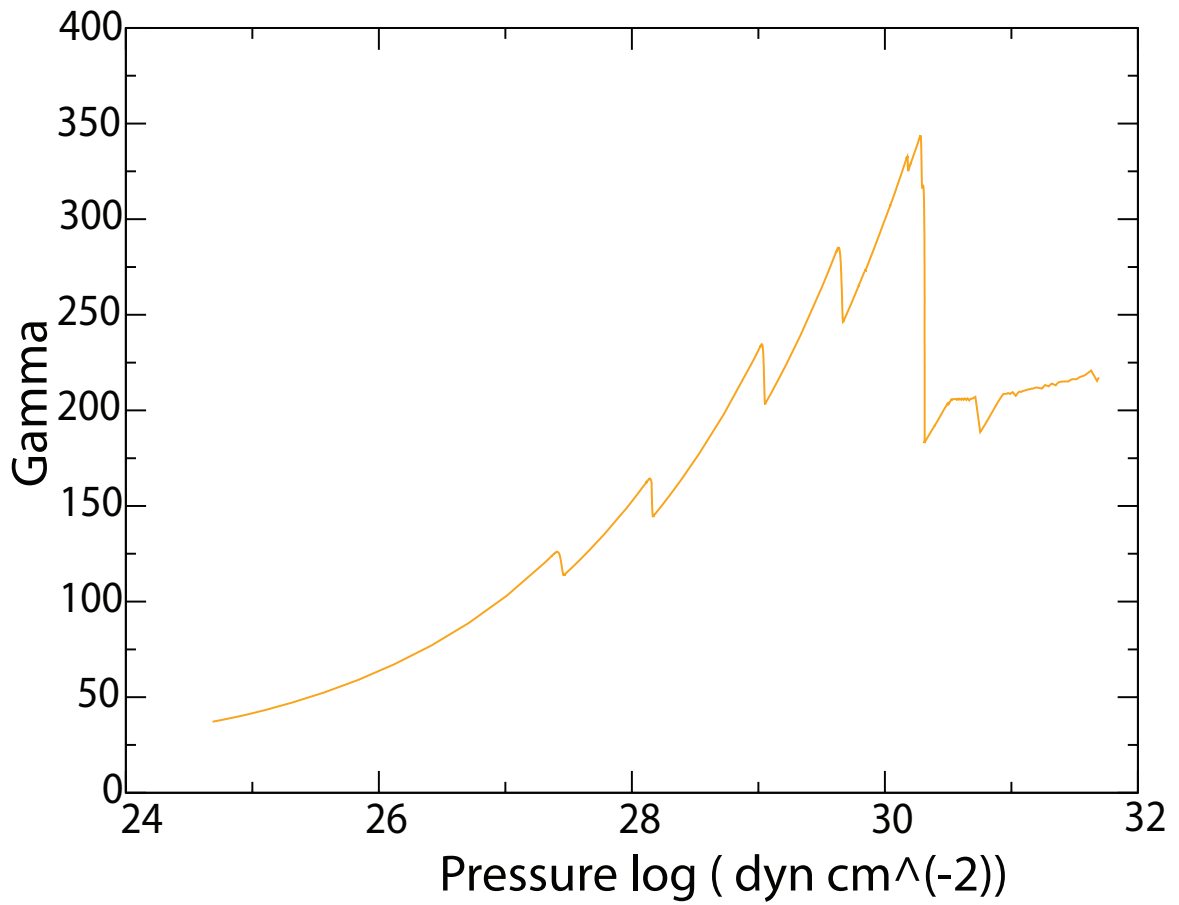
Figure 5.3: The Γ versus pressure log10 (dyn cm^{-2}).

Figure 5.4 shows the effective shear modulus for an initial composition of ^{56}Fe from Haensel & Zdunik's and our model. The effective shear modulus for an initial composition of superburst ashes is also shown. For a mix of nuclei, we assume Z is the average Z in equations 5.8 and 5.9. The shear modulus in general increases with mass density as the density of ions increases. Beyond neutron drip at a density around $\sim 10^{12}$ g cm^{-3} free neutrons reduce the ion number density leading to a weaker increase of the shear modulus with depth. In all 3 cases the calculated shear moduli are similar in the outer crust but they differ in the inner crust. In the model of Haesnel & Zdunik the shear modulus is a factor of 2 to 3 higher than in our model beyond a column depth of 1.0×10^{16} g cm^{-2}. This is because the higher Z and higher ion density predicted by Haensel and Zdunik.

5.4   Superfluidity

Neutrons in the neutron star can form a superfluid. Neutrons of opposite spins form pairs with zero total angular momentum and behave like bosons. These Cooper pairs condense into a lowest energy single particle state below a critical temperature.

Pulsar glitches and neutron star oscillations are believed to be the observational evidence of superfluidity in neutron stars. Besides, quiescent luminosity also provides clues for neutron superfluidity [58]. Brown et al (2009) models the cooling curves of KS 1731-260 and MXB 1659-29. They found that the light curve of a cooling crust can be described as a broken power law transitioning a constant at later times. From the model, the fit suggests that the heat capacity is low, implying that the inner crust is a superfluid. Thus, the location of neutron drip is critical.

Figure 5.5 shows the neutron abundance in log10 versus column depth for an initial com-

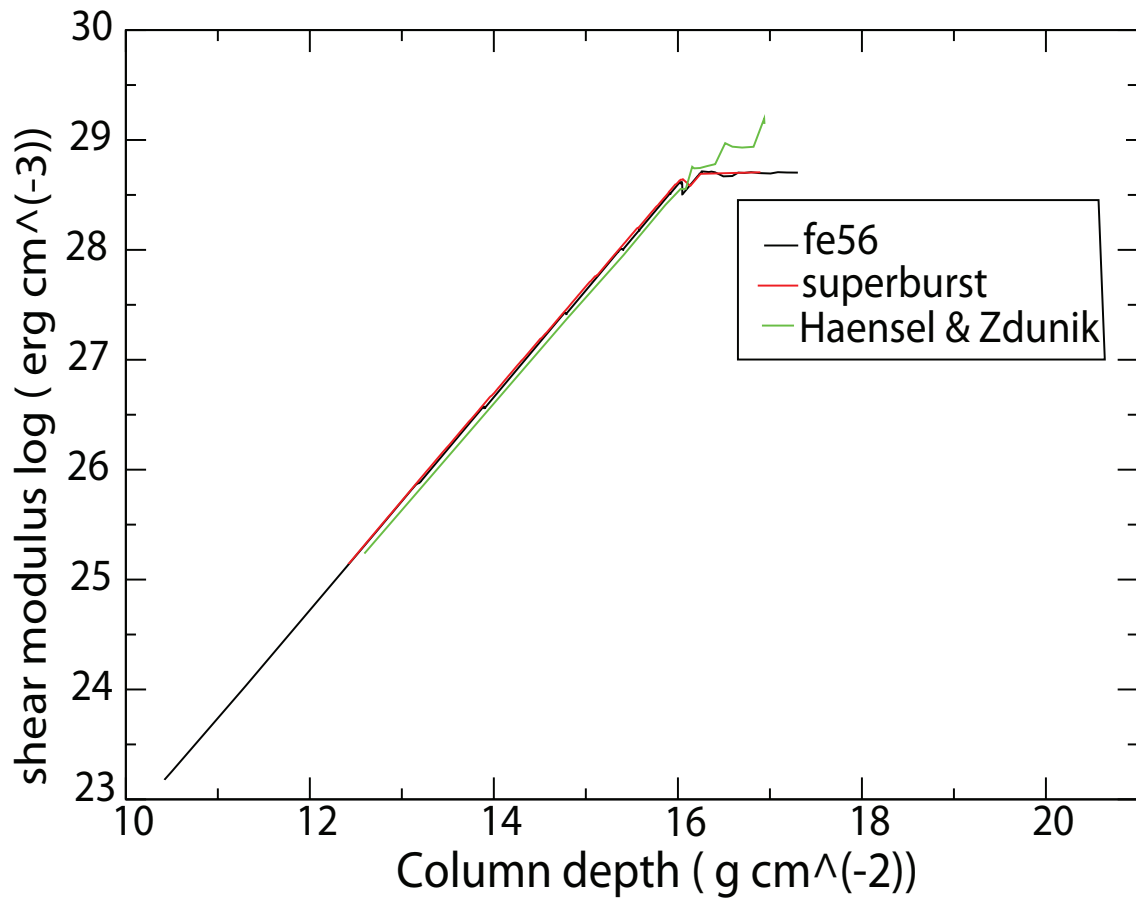Figure 5.4: The shear modulus in log10 (erg cm−3) versus column depth in log10 (g cm^{-2}) from this work for an initial composition ^{56}Fe (black) and superburst ashes (red) as well as from Haensel and Zdunik (green)

position of ^{56}Fe from Haensel & Zdunik and from our crust model. The neutron abundance of the initial composition of superburst ashes is also shown. In our model, neutron drip occurs later than in previous work. This is because some of the nuclei emit neutrons and immediately some nuclei capture the neutrons emitted which postpone neutron drip. The differences in the mass models also lead to different neutron drip. After 2.0×10^{16} g cm^{-2}, our models emit neutrons more efficiently than Haensel & Zdunik because of the more rapid pycnonuclear fusion cycles. In Haensel & Zdunik nuclei fuse together to form heavier nuclei and electron capture then down to heavier nuclei (heavier than ^{40}Mg) which leads to less neutrons emission.

5.5   Electrical and thermal conductivities

The main carriers in the thermal and electrical transport processes in the crust are electrons. Electron-electron scattering is negligible because the electrons are degenerate [10]. Thus, electric and thermal conductivities in the crust are mainly set by electron-phonon and electron-impurity scattering. The electronic conductivity affects ohmic diffusion timescales and therefore magnetic evolution [12]. The thermal conductivity affects the cooling in transients during the off state as well as the thermal profile. In the relaxation -time approximation, the electrical (σ) and thermal (κ) conductivities are (Yakovlev & Urpin 1980) [89]

$$\sigma = \frac{e^2 n_{\mathrm{e}}}{m_{\mathrm{e}}^* \nu_\sigma} \tag{5.10}$$

$$\kappa = \frac{\pi^2 k_{\mathrm{B}}^2 T n_{\mathrm{e}}}{2 m_{\mathrm{e}}^* \nu_\kappa} \tag{5.11}$$
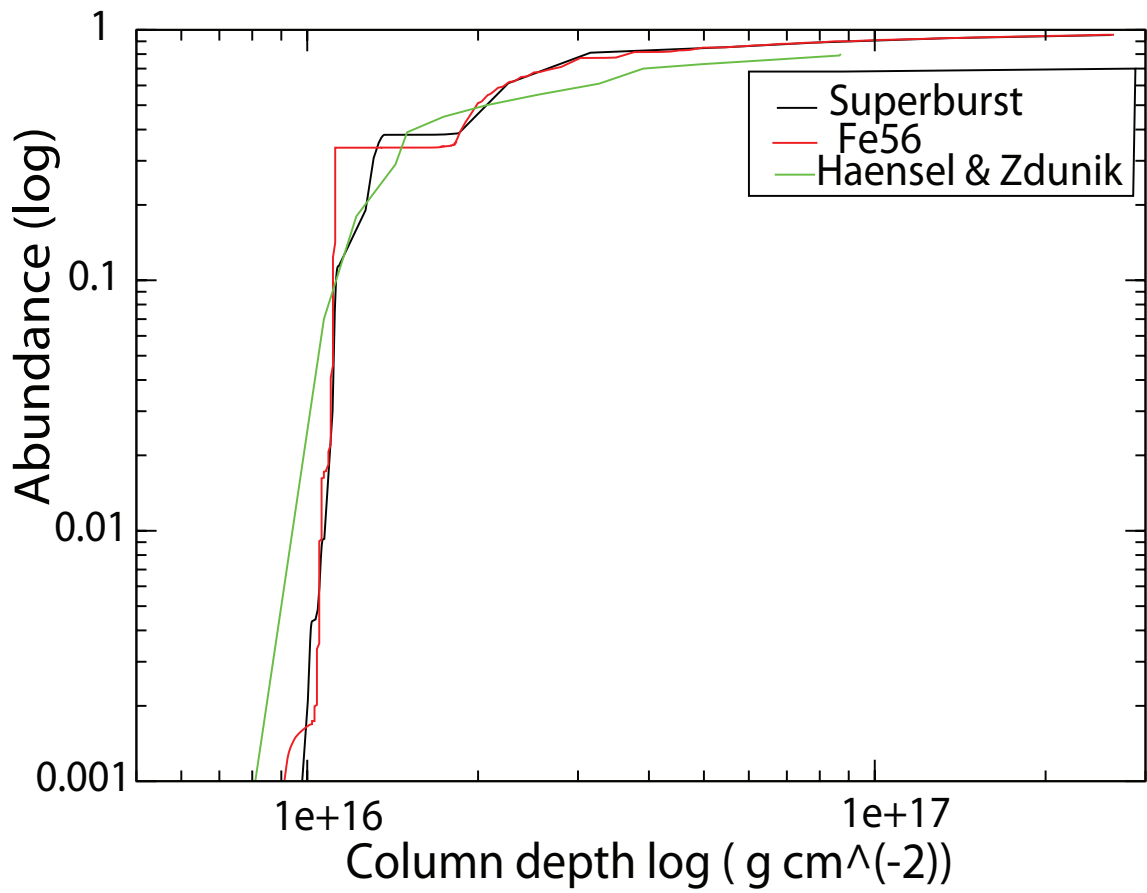
Figure 5.5: The neutron abundance in log10 versus column depth in log10 (g cm^{-2}) from this work for an initial composition of ^{56}Fe (red) and superburst ashes (black) as well as from Haensel & Zdunik (green)

Assuming electron-electron scattering is negligible:

$$\nu = \nu_\kappa = \nu_\sigma \tag{5.12}$$

where ν is the sum of the electron-phonon ($\nu_{\rm ph}$) and electron-impurity collision frequencies ($\nu_{\rm imp}$).

$$\nu = \nu_{\rm ph} + \nu_{\rm imp} \tag{5.13}$$

The electron-phonon and electron-impurity collision frequencies can be calculated as Urpin & Yakovlev (1980) [68]:

$$\frac{1}{\nu_{\rm ph}} = \frac{\hbar^2 c}{13e^2 k_B T}[1 + (\frac{\Delta}{3.5kT})^2]^{1/2}; \tag{5.14}$$

with the Δ is the Debye temperature:

$$\Delta = 1.76 \times 10^8 K(\frac{2Z}{A})(\frac{\rho}{10^{10}gcm^{-3}})^{1/2} \tag{5.15}$$

For mixed nuclei, the Debye temperature is calculated approximately by averaging the Z and A values.

$$\frac{1}{\nu_{\rm imp}} = \frac{13\pi\hbar^3}{8m_{\rm e}e^4}\frac{Z}{Q}\frac{m_{\rm e}c}{p_{\rm Fe}} \tag{5.16}$$

where Q is the impurity parameter and p_{Fe} is the Fermi momentum of the electrons. Figure 5.6 shows the electron-impurity scattering frequency for the most impure crust composition studied here, the superburst ashes, and compares it to the electron-phonon frequency for the same composition for a temperature of 0.5 GK. As we can see, the electron-phonon frequency is around an order of magnitude higher than the electron-impurity scattering frequency. This implies that electron-impurity scattering is negligibile in the crust of accreting neutron stars

that process all their accreted material through superbursts. But if we compare it to the electron-phonon scattering at 0.01 GK, we can see that the electron-impurity scattering is comparable with the electron-phonon scattering.

Figure 5.7 shows the electrical conductivity calculated from the composition and electron density of Haensel & Zdunik and from this work for both, initial ^{56}Fe and initial superburst composition. They are calculated for a temperature of 0.5 GK. As we can see, the electrical conductivity increases with the mass density as the electron density increases. Beyond a density of $\sim 10^{12}$ g cm^{-3} the conductivities diverge. This is because the Z/A values are different in our model from Haensel & Zdunik. The electron densities are also different. In our model, the electron density remains constant while in Hasenel and Zdunik the electron density increases.

The thermal conductivities show a similar behavior as the electrical conductivities.

5.6   Shear viscosity

The shear viscosity of the crust might have a damping effect on the amplitude of r-modes oscillations in rotating neutron stars [90]. Such damping has implications for the emission of gravitational waves. Here we assume the crust is a solid plasma where the transport is dominated by electrons. The electron shear viscosity can be expressed as [10]:

$$\eta = \frac{n_e p_{\text{Fe}} v_{\text{Fe}}}{5 \nu_{\text{ph}}} \tag{5.17}$$

Figure 5.9 shows the electron shear viscosity for an initial composition of ^{56}Fe calculated from the results of Haensel & Zdunik and from this work. The electron-shear viscosity calculated

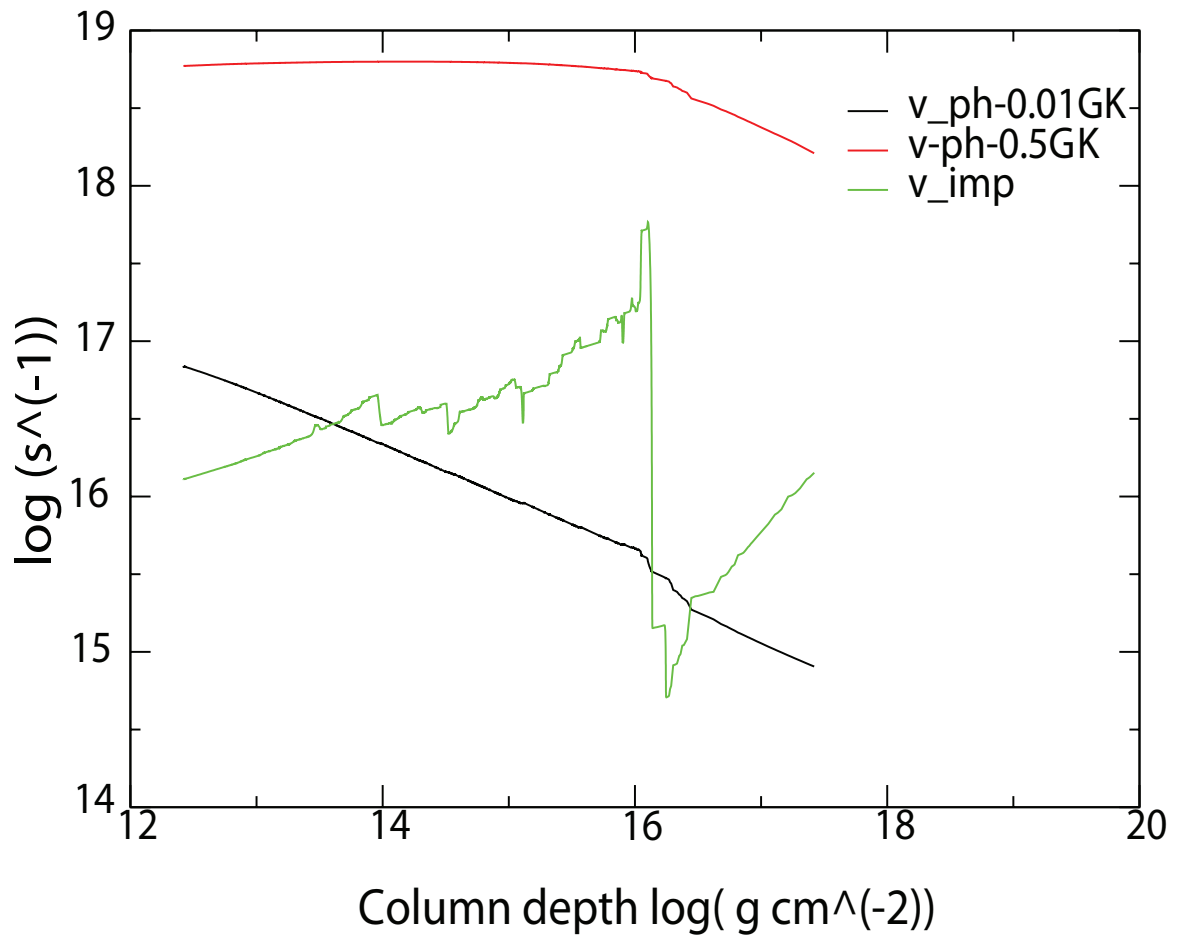Figure 5.6: The electron-impurity scattering frequency and electron-phonton scattering frequency $\log 10$ (s^{-1}) of superburst
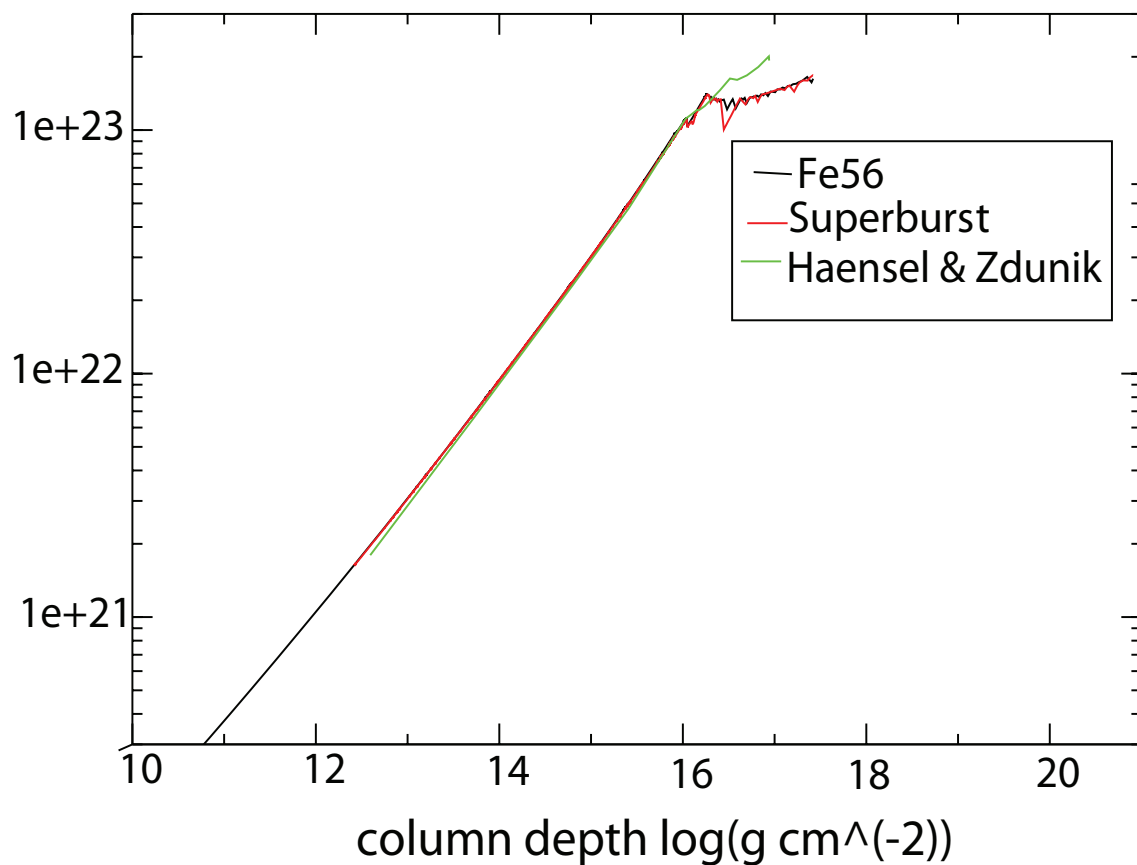
Figure 5.7: The electrical conductivity in $\log 10(\mathrm{s}^{-1})$ versus column depth $\log 10 \ (\mathrm{g \ cm}^{-2})$ for an initial composition of $^{56}\mathrm{Fe}$ (black), Superburst ashes (red) and Haensel & Zdunik (green)

for an initial composition of superburst ashes is also shown. The shear viscosity increases with mass density. This is because the electron density increases with mass density. There are discrepancies between our models and Haensel & Zdunik's results beyond column depth of 1.0×10^{16} g cm^{-2} because Hasenel & Zdunik find higher electron densities.

Figure 5.8: The shear viscosity in log10(g cm^{-1} c^{-1}) versus column depth in log10 (g cm^{-2}) for initial abundance of ^{56}Fe,(black), superburst (red) and Hasenel &Zdunik (green)

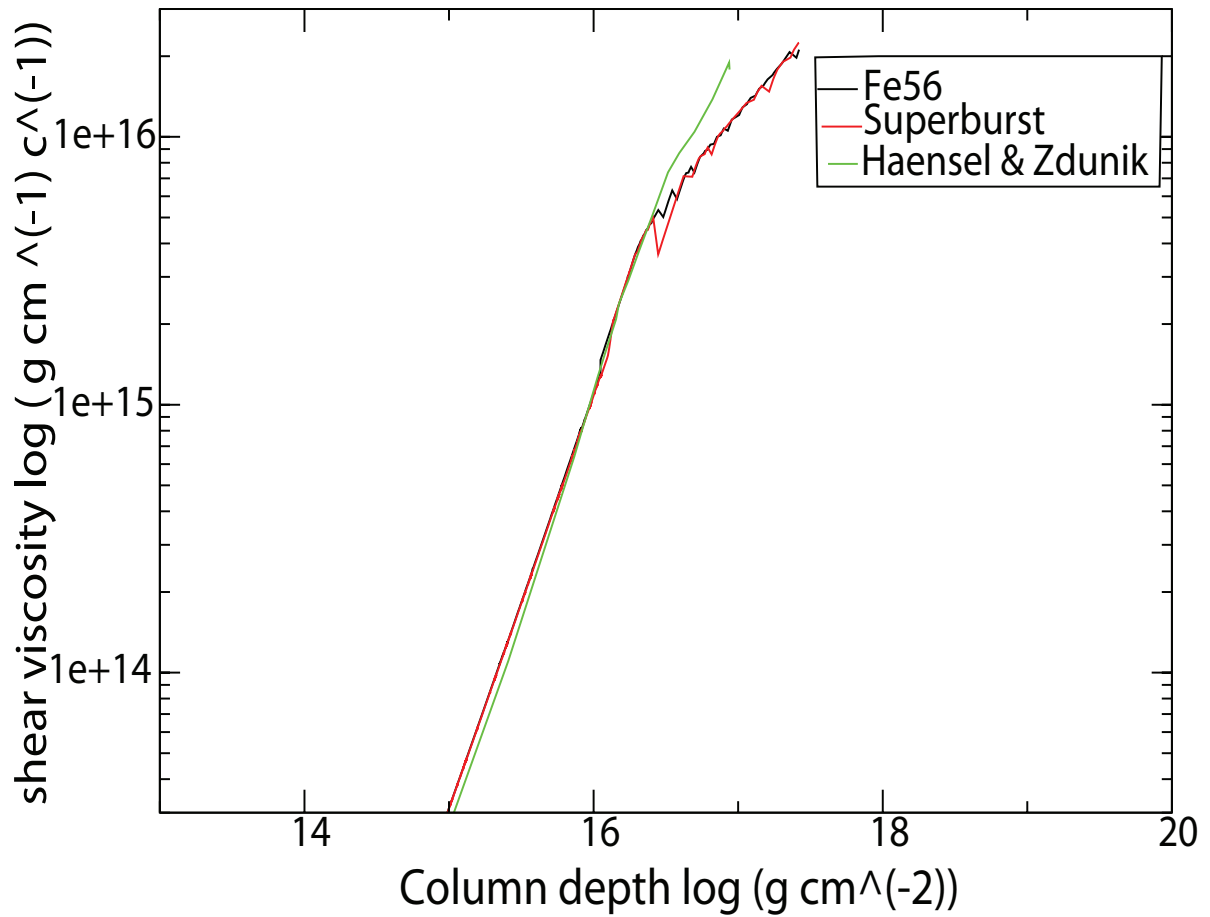# Chapter 6

Conclusion & Discussion

The goal of the thesis is to understand the nuclear reactions and associated heat generation in the crust of accreting neutron stars. This is the first network reaction calculation of neutron star crust processes that uses a complete set of nuclear reactions, including electron capture with neutron emissions, β decay, neutron capture, photodisintegration, and pycnonuclear fusion. The main differences to the results from previous work are:

(1) Even for single species initial composition, the reaction path splits and multiple nuclear species are present beyond neutron drip.

This is because we use finite and realistic electron capture rates. When nuclei undergo electron capture and neutron emissions, the high neutron capture rates capture the neutrons emitted and lead to path splitting.

(2) Pycnonucler fusion sets in earlier than predicted previously and during this earlier phase involves lighter species.

This is because the super electron cascade effect which was found by Gupta et al [20] leads to electron capture to production of lighter nuclei at a low density which allows pycnonuclear

fusions to set in at a lower depth.

(3) ^{40}Mg plays a special role. Regardless of initial composition all nuclei are converted into ^{40}Mg beyond a column density of 1.0×10^{16} g cm^{-2}. Therefore ^{40}Mg is the main fuel for the beginning of the main phase of pycnonuclear fusion

This is because we use a mass model considering shell effects. Because ^{40}Mg has a neutron magic number N=28 and therefore a high electron capture threshold and a high neutron separation energy. Neutron capture rates and electron capture rates are low.

(4) Pycnonculear fusion proceeds in cycles where the fusion reaction is the slowest reaction. Therefore, fusion is not followed by a layer of high Z nuclei but the composition in the inner crust remains predominantly ^{40}Mg throughout.

This is because of the super electron capture cascade effect that leads to nuclei emit all the way down to light nuclei expect ^{40}Mg which has a high electron capture threshold as explained in (3).

(5) Neutron drip happens at a higher density than in previous work.

This is because some nuclei emit neutrons and other nuclei which have high neutron capture rates immediately capture the neutrons emitted. This postpones the neutron drip to a higher density. The difference is also caused by a different mass model we use.

As a result one finds significant differences to the predictions from previous work.

In this thesis we use an initial set of nuclear physics input. Although the nuclear physics input is uncertain because the nuclei are very neutron rich and experimental data are unavailable, significant improvements are still possible in the nuclear physics. First, the neutron capture rates we use here are calculated using a rather crude approximate analytical formula. More sophisticated predictions of the dominant direct capture processes should be possible.

106

The neutron degeneracy and neutron superfluidity in the calculation of the neutron capture rates are neglected. This is justified for an initial study as neutron capture rate calculations have large uncertainties, but it will be interesting to explore the effects of the neutron degeneracy and superfluidity in the future. Although a correction factor for the photodisintegration rates is included to account for fully degenerate neutrons, a descriptions allowing for arbitrary degrees of degeneracy could be implemented. Furthermore, the pycnonuclear reaction rates for odd-even nuclei are calculated by extrapolations from the even-even nuclei. In principle, the S-factor of the odd-even nuclei should be calculated to give more accurate pycnonuclear fusion rates. However, the pycnonuclear fusion rates themselves are also very uncertain. The structure of the neutron star crust (whether it is body-centered cubic or face centered cubic, lattice imperfections, distribution of nuclei etc) are expected to affect the pycnonuclear fusion rates greatly [74]. The uncertainties from a lack understanding of the masses and structure of neutron rich exotic nuclei also affect the calculation. In our model, we use the FRDM model, complemented with the Hilf mass for nuclei lighter than oxygen. In the future, it would be preferable to use a consistent set of mass which covers the neutron rich and light nuclei, though the accurate prediction of the masses of light nuclei remains a major challenge in nuclear theory. There are also large uncertainties in the electron capture rates, in particular because the first forbidden transitions are neglected. This could also be improved in the future, should global predictive models of first forbidden strength become avaliable.

BIBLIOGRAPHY

BIBLIOGRAPHY

[1] J.M. Lattimer. & M. Prakash., *Science.*, **304**:536, 2004.

[2] S.L. Shapiro & S A. Teukolsky., *Black Holes, White Dwarfs and Neutron Stars: The Physics of Compact Objects.*, 1983.

[3] P. Haensel et al., *Neutron Stars.*, Springer, 2007.

[4] Kaspi et al., *Compact stellar X-ray sources.*, Cambridge University Press, 2006.

[5] S.E. Thorsett & D. Chakrabarty., *ApJ.*, **512**:288, 2010.

[6] Kiziltan et al., *arXiv:1011.4291.*, 2010

[7] Demorest et al., *Nature.* **467**:1081-1083, 2010

[8] Cornelisse et al., *A & A.*,**382**:174, 2000

[9] Steiner et al., *ApJ*, **722**:33, 2010

[10] N. Chamel & P. Haensel, *Living Reviews in relativity*, volume 11, 2008

[11] L. Bildsten., *ApJ*, **506**:842, 1998

[12] E.F. Brown & L. Bildsten., *ApJ*, **496**:915, 1998

[13] Ushomirsky et al., *MNRAS*, **319**:902, 2000

[14] K. Sato., *Prog. Theor. Phys.*, **62**:957, 1979

[15] G. Bisnovatyi-Kogan & V. Chechetkin., *Sov. Phys. Usp.*, **22**:89, 1979

[16] Y. Vartanyan & N.Ovakimova., *Soob. Byur. Obs.*, **49**:87, 1976

[17] P. Haensel & J. Zdunik., *A & A.*, **227**:431, 1990

[18] P. Haensel et al., *A & A.*, **314**:328, 1996

[19] S.S. Gupta et al., *ApJ*, **662**:1188, 2007

[20] S.S. Gupta et al., *Phys. Rev. Lett.* **101**:23101, 2008

[21] M. Beard et al., *Atomic and Nuclear Data Tables*, **96**:541, 2010.

[22] W. Baade, & F. Zwicky., *Proc. Nat. Ac. Sci.*, *20*:254, 1934

[23] J.R. Oppenheimer, & G.M. Volkoff., *Phys. Rev.*, **55**:374, 1939

[24] A.G.W. Cameron., *ApJ.*, **130**:884, 1959

[25] A.Hewish et al., *Nat.*, **217**:709, 1968

[26] E. Schreier et al., *ApJ.*, **172**:L79, 1972

[27] H. J. Grimm et al., *MNRAS.*, **339**:793, 2003

[28] H. Schatz et al., *ApJ.*, **524**:1014, 1999

[29] Grindlay et al., *ApJ.*, **205**:L127, 1976

[30] L. Maraschi & A. Cavaliere., *X-ray binaries and compact objects.*, 1977

[31] H. Schatz & Rehm., *Nuclear physics A* **777**:601, 2006

[32] H. Schatz et al., *Phys. Rev. Lett.*, **86**:3471, 2001

[33] J.J.M. in't Zand et al., *A & A.*, **426**:257, 2004

[34] E.F. Brown., *ApJ.*, **614**:L57-L60, 2004

[35] E. Kuulkers., *Nuclear Physics B-Proceedings Supplements.*, **132**:466, 2004

[36] S. Campana et al., *The Astronomy and Astrophysics review.*, **8**:279, 1998

[37] L. Cominsky et al., *ApJ.*, **224**:46, 1978

[38] L. Maraschi et al., *Nat.*, **259**:292, 1976

[39] N. E. White & F. E. Marshall., *ApJ.* **281**:354, 1984

[40] J. K. Cannizzo et al., *in Accretion Disks in Compact Stellar Systems.*, World Scientific Publishing, 1993

[41] J. van Paradijs, *ApJ.*, **464**:L139, 1996

[42] M. Tavani & J. Arons.,*ApJ.*, **477**:439, 1997

[43] E. Brown et al., *ApJ.*, **504**:L95, 1998

[44] R. E. Rutledge et al., *ApJ.*, **559**:1054-1059, 2001

[45] S. Campana et al., *A & A.* **324**:941, 1997

[46] E. M. Cackett et al., *MNRAS.*, **372**:479 2006

[47] E. M. Cackett et al, *ApJ.* **687**:L87, 2008

[48] Sunyaev R., *IAU Circ.*, **4839**, 1, 1989

[49] Sunyaev R., *IAU Circ.*, **5104**, 1, 1990

[50] R. Wijnands et al., *ApJ.*, **560**:L159, 2001

[51] R. Wijnands et al., *ApJ.*, **573**:L45, 2002

[52] W. H. G. Lewin et al., *IAU Circ.*, **2994**, 1976

[53] L.Cominsky et al., *ApJ.*, **270**:226, 1983

[54] in't Zand J. et al., *IAU Circ.*, **7138**, 1999

[55] R. Wijnands.et al., *ApJ.*, **566**:1060, 2002

[56] R. Wijnands et al., *ApJ.*, **594**:952, 2003

[57] R. Wijnands et al., Rev. Mex. Astron, Astrofis. Conf. Ser., Vol. 20, Compact Binaries in the Galaxy and Beyound. UNAM, Mexico, 2004

[58] E. F. Brown & A. Cumming., *ApJ.*, **698**:1020, 2009

[59] E. F. Brown., *ApJ.*, **531**:988, 2000

[60] F. X. Timmes & F. D. Swesty., *ApJ*, **126**:501, 2000

[61] R. Farouki,& S. Hamaguchi., *Phys. Rev. E.*, **47**:4330, 1993

[62] F. D. Mackie & G. Baym., *Nucl. Phys. A.*, **285:332**, 1977

[63] W.H. Press et al., *Numerical Recipes in FORTRAN*, Cambridge Univ. Press, 1992

[64] D. G. Yakovlev et al., *A & A*, **343**:650, 1999

[65] N. Ioth & Y. Kohyama, *ApJ*, **404**:268, 1993

[66] A.Y. Potekhin et al., *A & A*. **346**:345, 1999

[67] A. D. Becerril Reyes et al., *Symposium on Nuclear Astrophysics -Nuclei in the Cosmos -IX*, 2006

[68] P. *Möller* & J. Randrup., *Nuclear Physics A.*, **514:1**, 1990

[69] G.J. Mathews et al., *ApJ.*, **270**:740, 1983

[70] Christian iliadis, *Nuclear Physics of Stars*, 2007

[71] T. Rauscher & F. -K. Thielemann., *Atomic Data and Nuclear Data Tables.*, **75**:1, 2000

[72] P. S. Shternin & D. G. Yakovlev., *Phys. Rev. D.*, **79**:123004, 2009

[73] C. J. Hansen et al., *Stellar Interiors - Physical Principles, Strcuture, and Evolution*, 1995

[74] D. G. Yakovlev et al, *Phys. Rev. C.*, **74**:035803, 2006

[75] E. E Salpeter & H. M. Van Horn, *ApJ.*, **155,**:183, 1969

[76] A.Estrade, *Phys. Rev Lett.*, **107**:172503, 2011

[77] Private Communication April 2011 by Georges Audi and Wang Meng

[78] P. Möller et al., *Atomic Data and Nuclear Data Tables.*, **59**:185, 1995

[79] E. R. Hilf et al., *Proceedings of the 3rd International Conference on Nuclei Far from stability.*, pages 142-148, 1976

[80] S. Goriely et al., *Phys. Rev.* **82**:035804, 2010

[81] W. D. Myers & W. J. Swiatecki, *Nuclear Physics.* **81**:1, 1966

[82] W. R. Hix and F.-K. Thielemann., *Journal of Computational and Applied Mathematics*, **109**:321,1999

[83] P. Haensel. & J. L. Zdunik, *A & A*, **229**:1,1990

[84] H.Schatz et al., *Nuclear Physics A*, **718**:247, 2003

[85] B. M. Mirza, *International Journal of theoretical physics*, **48**:723

[86] A.I. Chugunov & D.G. Yakovlev, *Astronomy Reports*,**49**:724

[87] C. J. Horowitz & Kai Kadau, *Phys. Rev. Lett.*, **102**:191102, 2009

[88] S. Ogata, & S. lchimaru, *Phys. Rev. A*,**42**:4867, 1990

[89] D. G. Yakovlev & V. A. Urpin, *AZh*, **57**:526, 1980

[90] O.L.Caballero et al., *Phys. Rev. C*, **78**:045805, 2008